Strain Localisation during Dome-Building Eruptions

Jackie Evan Kendrick

München 2013

Strain Localisation during Dome-Building Eruptions

Jackie Evan Kendrick

Dissertation
an der Fakultät für Geowissenschaften
der Ludwig-Maximilians-Universität
München

vorgelegt von
Jackie Evan Kendrick
aus Cardiff, United Kingdom

München, den 18 Februar 2013

Erstgutachter: Prof. Dr. Donald B. Dingwell
Zweitgutachter: Prof. Dr. Claudia A. Trepmann
Tag der mündlichen Prüfung: 01. Juli, 2013

A view from within…

"All right then! I can conquer this mountain!"

-Didymus, Labyrinth

Contents

List of Figures

List of Tables

Acknowledgements

improbable without the aid of Sandra Grosskopf, Margot Lieske, Rosa Susnjar, Carina Brackenhofer, Renate Döring and Isabel Heggmair.

Without O. Spieler and S. Mueller there would be no Colima samples. Nick Varley, thanks for dragging us up there, (what a view!) and to Adrian Hornby for putting the rest of us to shame. To all my other field companions: too many to mention, but all memorable... And to everyone I've shared a bevvy, a brew or a bite with- Orya, Sascha, Jeremie, Linda, Basti, Alex, Asher (for trying to teach me MATLAB), Paul, Klaus, Nikita- I wish you all the best.

-Team Moose Honorary Member and Token Girl

Preamble

Part of the data presented in this doctoral dissertation have been published in scientific journals, are in the review process or are in preparation; namely,

1. Kendrick, J.E., Lavallée, Y., Ferk, A., Perugini, D., Leonhardt, R. and Dingwell, D.B., 2012, Extreme frictional processes in the volcanic conduit of Mount St. Helens (USA) during the 2004-2008 eruption, *Journal of Structural Geology*, 38: 61-76.

2. Kendrick, J.E., Lavallée, Y., Hess, K-U., Heap, M.J., Gaunt, H.E., Meredith, P., and Dingwell, D.B., 2013, Tracking the permeable porous network during strain-dependent magmatic flow, *Journal of Volcanology and Geothermal Research*, 260: 117-126.

3. Kendrick, J.E., Lavallée, Y., Mariani, E. and Dingwell, D.B., Crystal plasticity as a strain marker of the viscous-brittle transition in magmas. In Review at *Geology*.

4. Kendrick, J.E., Lavallée, Y., Hess, K-U., Ferk, A., Dingwell, D.B. and Leonhardt, R, Seismogenic frictional melting in the magmatic column. Submitted to *Solid Earth*.

5. Kendrick, J.E., Lavallée, Hirose, T., di Toro, G. and Dingwell, D.B., Frictional melt brake and stick-slip in volcanic conduits. In preparation for *Nature*.

Summary
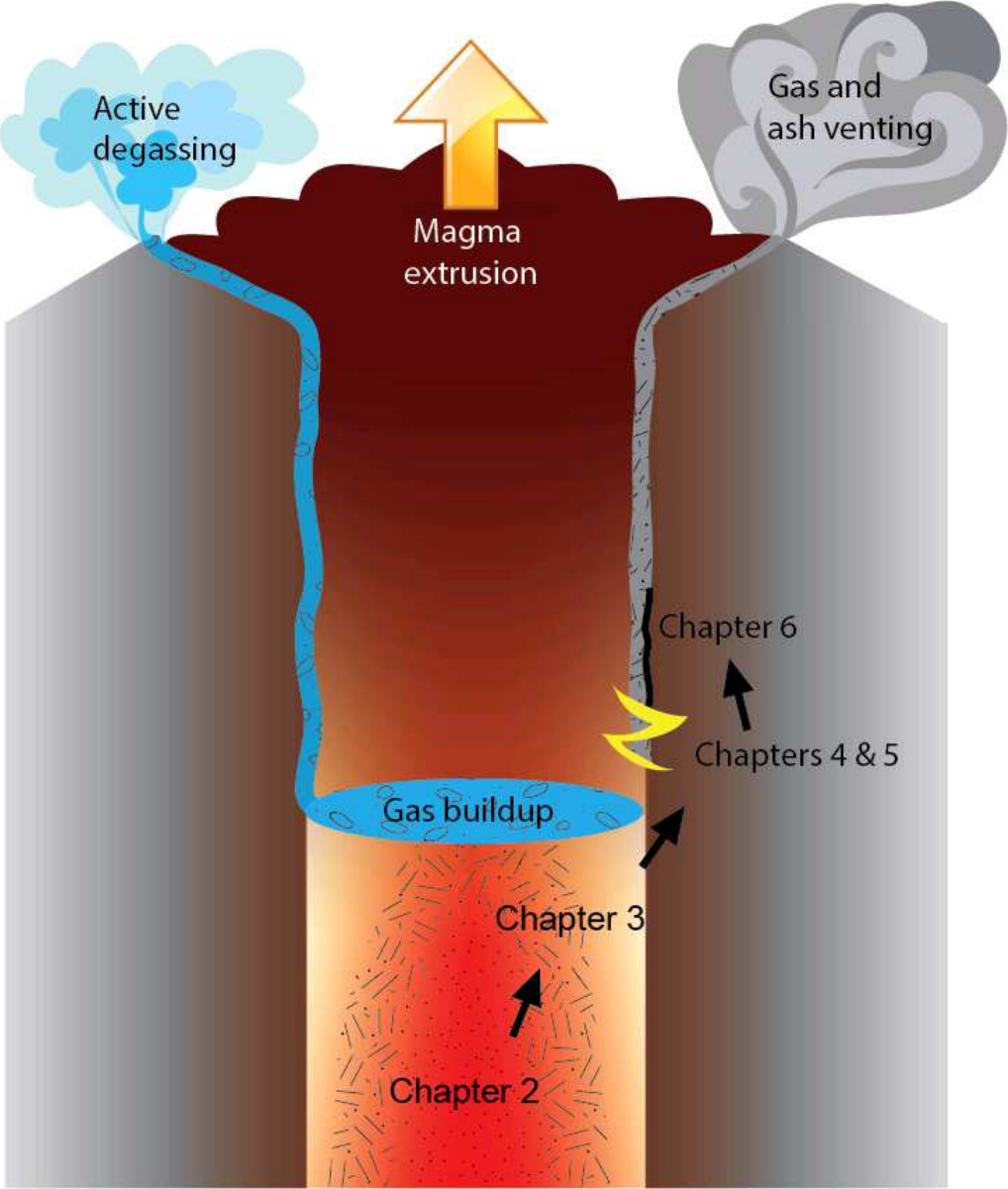
Figure S-1. Schematic chapter index. The ascent of magma through the conduit is depicted in terms of the chapter which describes the processes involved.

Volcanic landscapes often present advantages for people who inhabit the surrounding areas, but the increasing numbers of people threatened by potential activity increases as these settlements grow. It is thus of vital importance to glean as much information as possible by monitoring active volcanoes (including seismicity, ground deformation, gas flux and temperature changes). Although volcanic behaviour can be difficult to predict, precursory information can often be identified retrospectively (once an eruption begins) to help link antecedent behaviour to eruption attributes. Likewise, eruption relics can be used to identify processes in pre-eruptive

magma. Additionally, a huge amount of information may be gathered through experimentation on rock and magma samples. This study combines field and analytical studies of natural samples from Volcán de Colima (Mexico), Mount St. Helens (USA) and Soufrière Hills (Montserrat) with high-temperature magma deformation experiments to investigate the processes involved with magma ascent during dome-building eruptions (Figure S-1).

The study of conduit-dwelling magma is of the utmost importance for understanding transitions from effusive to explosive eruptions. Of primary interest is the rheology of highly crystalline magmas that make up the magma column. Rheology is integrally linked to the composition and textural state (porosity, crystallinity) of magma as well as the stress, temperature and strain rate operative during flow. Many studies have investigated the rheology of multi-phase magmas, but in **Chapter 2** this is notably linked to the evolution of the physical properties of the magmas; tracing the changes in porosity, permeability, Poisson's ratio, Young's modulus during strain dependent magmatic flow. Especially at high strain rates mechanical degradation of the magma samples may supersede magmatic flow and crystal rearrangement as the dominant form of deformation, resulting in lower apparent viscosities than those anticipated from magmatic state. This leads to an evolution of the fracture network to form inhomogeneous distribution of the permeable porous network; with damage zones cutting through areas of densification. In a conduit setting this is analogous to the formation of a dense, impermeable magma plug which would prohibit degassing through the bulk of the magma. Degassing may or may not proceed along conduit margins, and the plug formation could lead to critical overpressures forming in the conduit and result in highly explosive eruption.

During the multi-scale process of strain localisation it is also probable that another previously unforeseen character acts upon magma rheology. **Chapter 3** details the first documentation of crystal plasticity in experimentally deformed multi-phase magmas. The extent of the crystal plasticity (evidenced by electron backscatter diffraction (EBSD)) increases with increasing stress or strain, and thus remnant crystals may be used as strain markers. Thus it seems that crystal-plastic deformation plays a significant role in strain accommodation under magmatic conditions. Indeed plastic deformation of phenocrysts in conduit magmas may be an important transitional regime between ductile flow and brittle fracture, and a time-space window for such deformation is envisaged during the ascent of all highly-crystalline magmas. This phenomenon would favour strain localisation and shear zone formation at conduit margins (as the crystal-

plastic deformation leads the magma toward brittle failure) and ultimately preferentially result in plug flow.

During volcanic eruptions, the extrusion of high-temperature, high-viscosity magmatic plugs imposes frictional contact against conduit margins in a manner that may be considered analogous to seismogenic faults. During ascent, the driving forces of the buoyant magma may be superseded by controls along conduit margins; where brittle fracture and sliding can lead to formation of lubricating cataclasite, gouge or pseudotachylyte as described in **Chapter 4** at Mount St. Helens. Within volcanic systems, background temperatures are significantly higher than the geotherm permits in other upper-crustal locations, whereas confining pressures are much lower than in high-temperature, lower-crustal settings: thus via their exceptional ambient P-T conditions, volcanic systems represent unique environments for faulting. This can result in the near-equilibrium melting and slow recrystallisation of frictional melt, which hinders the development of signature pseudotachylyte characteristics. Thus frictional melting may be more common than previously thought. Indeed **Chapter 5** documents a second occurrence at Soufrière Hills volcano. Here, the formation is linked to repetitive seismic "drumbeats" which occurred during both the eruption at Mount St. Helens and at Soufrière Hills. Strain localisation, brittle rupture, sliding and the formation of shear bands along the conduit margin can have important implications for the dynamics of eruptions. Specifically, the capability of degassing via the permeable porous network may be strongly influenced by the formation of pseudotachylyte, which has almost no porosity.

Based on the findings in chapters 4 and 5, a series of high-velocity rotary shear (HVR) experiments were performed. In **Chapter 6** the results of these experiments demonstrate the propensity for melting of the andesitic and dacitic material (from Soufrière Hills and Mount St. Helens respectively) at upper conduit stress conditions (<10 MPa). Additionally, frictional melting induces a higher resistance to sliding than rock on rock (which follows Byerlee's friction coefficient) and thus can act as a viscous brake. Variable-rate HVR experiments which mimic rapid velocity fluctuations during stick-slip motion demonstrate velocity-weakening behaviour of melt, with a tendency for unstable slip. The occurrence of frictional melting can explain the self-regulating, cyclic progression of stick-slip motion during viscous magma ascent and additionally accounts for the fixed-location, repetitive "drumbeats" via the arrival of fresh magma at the source.

Zusammenfassung

Vulkanische Landschaften stellen besonders vorteilhafte Lebensräume für ihre Bewohner dar, doch mit stetig wachsender Bevölkerung wachsen auch die mit vulkanischer Aktivität verbundenen Gefahren. Es ist daher besonders wichtig, so viele Informationen wie möglich durch stetige Überwachung (von Seismizität, Deformation, Gasaustritt und Temperaturänderungen) von aktiven Vulkanen zu gewinnen. Obwohl das Ausbruchsverhalten von Vulkanen schwer vorhersehbar sein kann, können vorangegangene Warnsignale häufig rückwirkend mit der Eruption korreliert werden. Diese Erkenntnisse ermöglichen dann eine bessere Risikoabschätzung bei künftigen Ausbruchsszenarien. In ähnlicher Weise können Eruptionsprodukte verwendet werden um Prozesse zu identifizieren, die in den tiefer gelegenen Magmakammern kurz vor einer Eruption stattfanden. Zusätzlich kann eine Fülle von Informationen durch Experimente an Gesteins- und Magmaproben gewonnen werden. Diese Arbeit kombiniert Feld- und Laboranalysen an natürlichen Proben des Volcán de Colima (Mexico), Mount St. Helens (USA) und Soufrière Hills (Montserrat) mit Hochtemperatur-Magmadeformationsexperimenten mit dem Ziel, die Prozesse zu studieren, die am Aufstieg von Magma während dombildenender Eruptionen beteiligt sind (Abb. S-1).

Die Erforschung von Prozessen, die sich während des Magmaaufstieges im vulkanischen Schlot ereignen, ist von äußerster Bedeutung für das Verständnis des Überganges von effusivem zu explosivem Eruptionsverhalten. Die Rheologie von hochkristallinem Magma ist dabei von vorrangigem Interesse. Das rheologische Verhalten des Magmas ist sowohl abhängig von der Zusammensetzung und dem strukturellen Zustand (Porosität, Kristallinität), als auch von der erfahrenen Auflast, Temperatur und der Deformationsgeschwindigkeit des Magmas während des Aufstieges. Viele Studien haben sich bereits mit der Rheologie von mehrphasigen Magmen beschäftigt, jedoch nur in statischen Zuständen. Kapitel 2 dieser Arbeit stellt daher die Rheologie in Beziehung zu den sich kontinuierlich verändernden physikalischen Eigenschaften eines Magmas. Veränderungen der Porosität, des Poisson-Verhältnisses und des Elastizitätsmoduls wurden während verformungsabhängigem, magmatischen Fließens ermittelt. Besonders bei hohen Deformationsraten kann mechanisches Versagen einem magmatischen Fließen und der Neuausrichtung von Kristallen zuvorkommen, was zu niedrigeren Gesamtviskositäten führen kann als im magmatischen Zustand zu erwarten wäre. Dies führt zur Entwicklung eines Netzwerkes von Brüchen, welches wiederum zu einer heterogenen Verteilung des porösen Permeabilitätsnetzwerkes führt, bei dem lokale

Störungszonen ansonsten verdichtete Zonen durchziehen. In einem Vulkanschlot entspricht dies der Bildung eines dichten, undurchlässigen Magmapfropfens der das Entgasen eines Großteils des Magmas verhindert. Eine Entgasung kann dann nur über die Schlotränder möglich sein, wodurch die Bildung eines solchen Pfropfens zu einem kritischen Überdruck und somit zu hochexplosiven Eruptionen führen kann.

Die Lokalisierung der Deformation entlang des Schlotes ist wahrscheinlich eine bis heute ungekannte Eigenschaft der Rheologie eines Magmas. Kapitel 3 enthält die erste bekannte Beschreibung von Kristallplastizität in experimentell deformierten, multiphasen Magmen. Die Kristallplastizität, nachweisbar durch Elektronenbeugung (electron backscatter diffraction, EBSD) wird intensiver mit erhöhter Auflast und/oder Deformation und daher können Kristalle als Deformationsmarker verwendet werden. Es scheint daher, dass die kristallplastische Deformation eine wichtige Rolle bei der Deformation eines Magmas unter natürlichen Bedingungen darstellt. Diese kristallplastische Deformation könnte sogar ein wichtiges Zwischenstadium bei Übergang von plastischer zu spröder Verformung eines Magmas darstellen und ein solches Deformationsregime wäre damit beim Aufstieg aller kristallreichen Magmen vorhanden. Dieses Phänomen würde die Lokalisierung von Deformation und das Entstehen einer Scherzone an den Schloträndern begünstigen (da die kristallplastische Verformung zu einer spröden Verformung des Magmas führt) und kann einen sogenannten "plug flow" erzeugen, der das Risiko einer explosiven Eruption erhöht.

Während vulkanischer Eruptionen entsteht durch die Extrusion eines hochviskosen Pfropfens ein Kontakt am Schlotrand, der ähnlich einer Störungszone aufgebaut ist. Übersteigt der Impuls des aufsteigenden Magmas die Festigkeit des Gesteins am Schlotrand, bewirkt sprödes Bruchverhalten und Scherung die Bildung eines Kataklasits oder Pseutotachylits, der schmierend wirkend kann. Dieser Effekt der Kataklasitbildung wird in Kapitel 4 am Beispiel von Mount St. Helens beschrieben. In vulkanischen Systemen sind die Temperaturgradienten signifikant höher als unter normalen geothermischen Bedingungen, während gleichzeitig der Umgebungsdruck deutlich niedriger ist als in den Hochtemperaturbereichen der unteren Kruste. Vulkanische Systeme stellen durch diese besonderen Druck- und Temperaturbedingungen eine einmalige Umgebung für die Entwicklung von Scherzonen dar. Dies kann zur Bildung und langsamer Rekristallisierung von Reibungsschmelzen führen, was die Entwicklung klassischer Pseudotachylit-Texturen verhindern kann. Die Bildung von Reibungsschmelzen kann daher häufiger vorkommen als ursprünglich angenommen. Kapitel 5 beschreibt ein weiteres

Vorkommen von Reibungsschmelzen am Soufrière Hills Vulkan. Die Entstehung solcher Schmelzen ist dabei an das Vorkommen von rhythmischer Seismizität, sogenannter "drumbeats", gebunden, die bei beiden Eruptionen vorkamen, auf die hier näher eingegangen wird. Die Lokalisierung von Deformation, spröde Verformung, Rutschen und die Entstehung von Scherbändern entlang des Schlotrandes können wichtige Einflüsse auf die Eruptionsdynamik haben. Insbesondere die Effizienz der Entgasung durch das durchlässige Porennetzwerk kann stark von der Bildung von nahezu porenfreiem Pseudotachylit beeinflusst werden.

Auf Grund der Ergebnisse von Kapitel 4 und 5 wurden eine Reihe von Scherversuchen bei Hochgeschwindigkeit (HVR) unternommen. Die Ergebnisse dieser Studie sind in Kapitel 6 zusammengefasst und demonstrieren die Eigenschaften andesitischer und dazitischer Schmelzen von Mount St. Helens und Soufrière Hills bei flachen Schlotbedingungen von weniger als 10 MPa. Zusätzlich bewirkt die Präsenz von Schmelze in Scherzonen höhere Gleitwiederstände als in schmelzfreien Szenarien. Dies entspricht dem Byerlee's Reibungskoeffizienten und zeigt, dass das teilweise Aufschmelzen an Scherhorizonten als viskose Bremse agieren kann. Geschwindigkeitsregulierte HVR Experimente, welche Geschwindigkeitsveränderungen während stick-slip Ereignissen nachahmen, zeigen die geschwindigkeitsschwächende Wirkung von Schmelze mit der Tendenz zu unstabilem Gleiten. Das Vorkommen von Reibungsschmelzen kann die selbst regulierende, zyklische Entwicklung von stick-slip Bewegungen während des Aufstiegs von Magma erklären und erklärt zusätzlich die gleichbleibende Tiefe der wiederholten 'drumbeats' durch die Ankunft von neuem Magma an der Quelle.

"…never seen such a sight, never heard such a bellow; it was like a mountain laughing"

- The Golden Compass

Chapter 1

Introduction

Volcanoes are amongst the most dynamic and enigmatic settings on Earth, and present economic advantages for those who live in surrounding areas (e.g. fertile soil, geothermal energy, tourism). However, they also represent potentially lethal neighbours for upwards of 500 million people worldwide who live within 100 km of historically active volcanoes (Marti and Ernst, 2005). Of these 550 or so volcanoes, only around 150 are monitored, and little more than a dozen adequately so (Tilling, 1996). Precursory activity including gas emissions, temperature changes, ground deformation and seismic output can indicate *when* but not *how* an eruption will proceed.

Since Pliny the Younger's accounts of Vesuvius's AD79 "plinian" eruption (Allen, 1961) people have begun to understand the dangers that volcanoes pose. The birth of "volcanology" followed the 1902 eruption of Mount Pelee (Martinique) as scientists began trying to unravel the remarkable, unpredictable and alarming occurrence of eruptions. With the ultimate goals of civil protection and crisis management in mind, a plethora of field, experimental and theoretical studies characterise, quantify and simulate the products and processes of volcanic eruptions (Alidibirov and Dingwell, 1996; Cimarelli et al., 2011; Costa et al., 2009; Gonnermann and Manga, 2005; Kueppers et al., 2006; Lavallée et al., 2008; Llewellin et al., 2002; Mueller et al., 2011; Mueller et al., 2004; Namiki and Manga, 2008; Okumura et al., 2009; Palladino et al., 2008; Scheu et al., 2008; Trigila et al., 2008; Yamamoto et al., 2008).

Dome-building eruptions have catastrophic potential, with dome collapse leading to devastating pyroclastic flows with almost no precursory warning. In recent history dome collapses have wiped out the town of St. Pierre (Martinique) and forced evacuation of 60% of the island of Montserrat. Highly viscous domes can also plug the volcanic conduit, allowing the calamitous build-up of magmatic overpressures and leading to highly explosive volcanic eruptions. Additionally, the steep morphology and frequently unconsolidated, ubiquitous layers of ash or pumice mean that composite cones are particularly susceptible to sector collapse (Siebert, 2004; Vidal and Merle, 2000). This may be triggered by volcanic unrest, heavy rainfall or earthquakes (Hürlimann, 2000) and can in itself lead to eruption (Lipman, 1981). Composite volcanoes continue to threaten not only the wellbeing of populations in close proximity to the flanks, but

also the social and economic welfare of lands much farther afield and hence their study is of great importance.

1.1. Glass transition

The transition from effusive to explosive volcanism is a common phenomenon worldwide (Barmin et al., 2002), but our understanding of the processes which control this evolution is poor. Silicate liquid behaves according to Maxwell, as a visco-elastic fluid (Webb and Dingwell, 1990). While behaviour is Newtonian at low strain rates, as deformation approaches the timescale of structural relaxation the response exceeds the elastic limit, inducing failure. This is represented by a deviation from a linear stress-strain relationship and is known as the glass transition. In short, the glass transition (Figure 1-1) marks the boundary of viscous to brittle magma deformation, and may be crossed by decreasing temperature or increasing strain rate (Dingwell, 1996). Both water and silica content have a drastic influence, with decreasing water content favouring the brittle field and silica vice-versa.
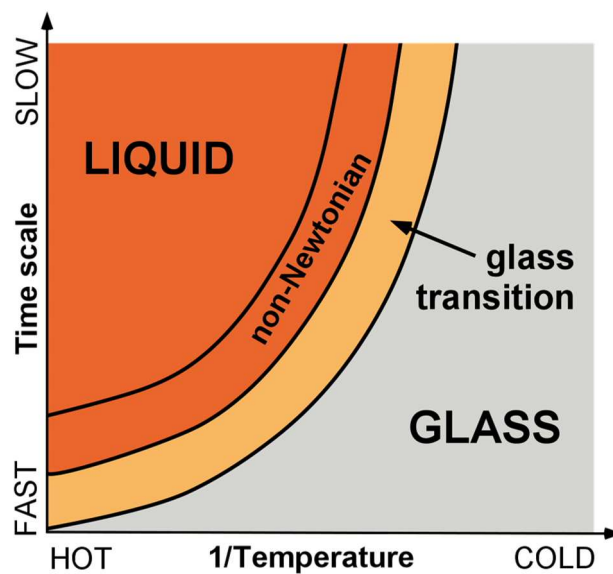
Figure 1-1. The glass transition in time-reciprocal temperature space. Deformations slower than the structural relaxation time entail a relaxed, viscous liquid response of the melt. When the timescale of deformation approaches that of the glass transition, the result is elastic storage of strain energy for low strains and shear thinning and brittle failure for high strains (modified from Dingwell et al., 1996).

1.2. Magma rheology and parallel plate viscometry

In nature however, magma is scarcely single phase, and commonly contains both pores and crystals. The addition of crystals to a melt increases viscosity, as first described by Einstein (1906). At low crystallinity (<40 %), this non-linear increase is described by the Einstein-Roscoe equation (Roscoe, 1952), parameterised by Marsh (1981).

While many volcanoes serve as a natural laboratory, there is also the necessity for experiments and modelling to further develop understanding, with the aim of improving our ability to forecast volcanic hazards. As local stresses (especially in the conduit) cannot be accurately measured in volcanoes (Ikeda et al., 2003), they must be estimated through either analytical or numerical modelling, which rely heavily on laboratory measurements and experimentally derived input parameters (Gudmundsson, 2006; Gudmundsson and Brenner, 2009; Gudmundsson and Philipp, 2006). With this in mind, uniaxial compression experiments inspired by the theoretical parallel plate viscometer of Gent (1960) were developed (Cordonnier et al., 2009; Hess et al., 2007; Lejeune and Richet, 1995).

The parallel plate viscometer has facilitated investigation of high-viscosity, natural melts (Hess et al., 2007; Lejeune and Richet, 1995). Beyond a given threshold of crystallinity, related to the maximum packing fraction, which in itself is dependent upon the size, shape (Picard et al., 2011) and distribution of the suspended crystals, stress-partitioning results in non-Newtonian rheological behaviour (Caricchi et al., 2007; Carreau et al., 1999; Cordonnier et al., 2009; Deubelbeiss et al., 2011; Lavallée et al., 2007; Lejeune and Richet, 1995; Webb and Dingwell, 1990). A set of equations determined to compute the apparent viscosity of melts with any crystal fraction were developed by Costa (2005). However, these did not explain the strain-rate dependence (Lejeune and Richet, 1995), which is incorporated into the work of Lavallée (2007), who developed a non-Newtonian rheological law for highly crystalline dome lavas (Eq. 1) where strain rate (γ) and eruptive temperatures (T) can be used to predict viscosity (η).

$$\log \eta = -0.993 + 8974/T - 0.543 * \log \gamma \qquad \text{(Eq. 1)}$$

The strain-rate dependence is manifest as a decrease in apparent viscosity with increasing strain rate above a threshold of 10^{-5} s^{-1} (Figure 1-2), a characteristic known as shear thinning (Caricchi et al., 2007; Lavallée et al., 2007; Stevenson et al., 1996). Shear thinning occurs in highly

crystalline mixtures, where the microstructure evolves and crystals align preferentially into the flow direction (Foss and Brady, 2000). The suspended particles will form a more ordered formation at higher shear rates (Petford, 2009). The crystalline magmas suffer an instantaneous variation in viscosity as a result of applied stress (Figure 1-3). Additionally, at constant stress there is a continued decrease in the viscosity of the sample with time, termed "time-dependent" deformation by Cordonnier et al. (2009).
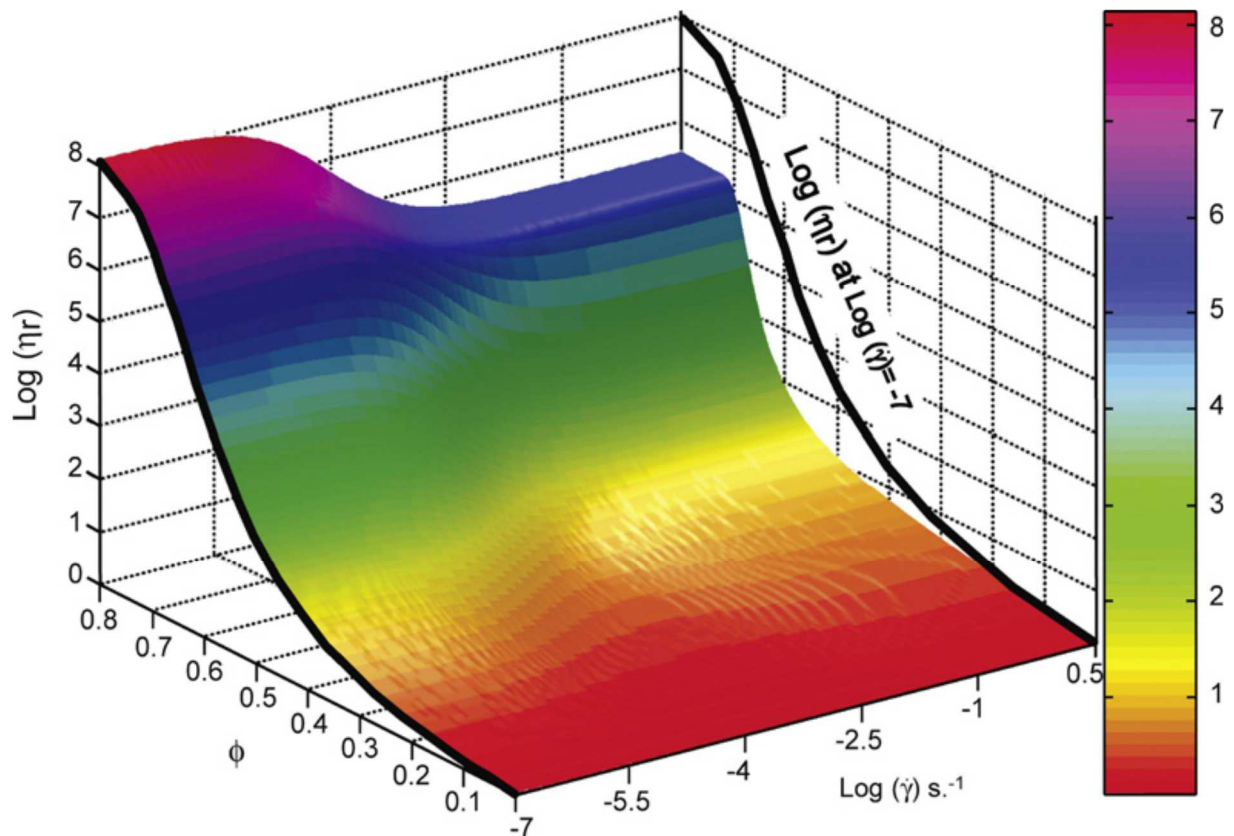
Figure 1-2. Variation diagram showing the logarithm of the relative viscosity (log ηr) as a function of crystal fraction (φ) and the logarithm of the strain rate (log γ) (s⁻¹). The black line on the right depicts the projection of the log ηr at a strain-rate 10⁻⁷ s⁻¹ and highlights the influence of γ˙ on the maximum packing fraction and demonstrates the shear thinning behaviour of crystal-bearing magmas (from Caricchi et al. 2007).
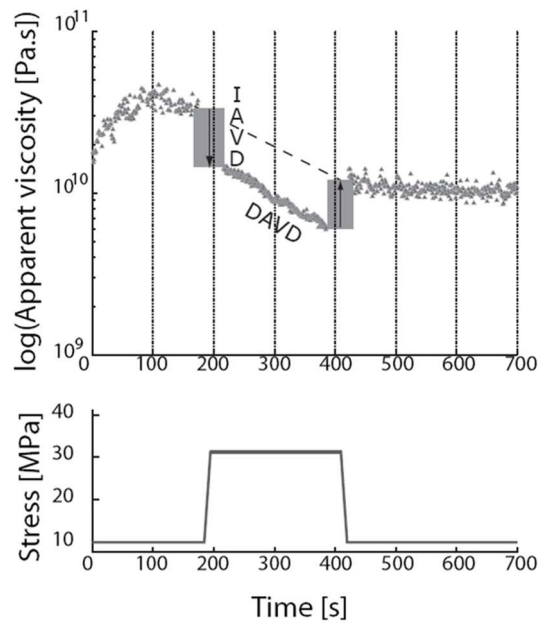
Figure 1-3. Multi-stress experiments. Example of instantaneous apparent viscosity profile obtained during an experiment in which 10, 30 and 10 MPa were successively applied to show shear thinning (IAVD) and time dependent (DAVD) deformation (after Cordonnier et al., 2009)

1.3 Breaking magma

The demonstrable brittle failure of magma at high temperature (Lavallée et al., 2008; Smith et al., 2011; Spieler et al., 2004; Tuffen et al., 2008; Webb and Dingwell, 1990) is integral to magma expulsion. Magma fragmentation occurs when the strain-rate surpasses the timescale of relaxation is considered the primary cause of explosive volcanism (Papale, 1999). It is highly probable that in ascending and extruding magma (especially during crystal-poor obsidian eruptions) the glass transition may be surpassed repeatedly (Tuffen and Dingwell, 2005), forming textures that record rupture and healing cycles (Figure 1-4). It is common for tensile rupture zones to form along with shear fractures (Paterson and Wong, 2005), and these may be filled with a mixture of crystal and glass fragments to form tuffisite veins.

Shearing and cracking also influence the development of the permeable porous network (Figure 1-5), manipulating the magmas ability to degas (Dingwell, 1996). Localised brittle failures or fragmentation evens along the conduit margins may increase degassing capabilities (Watts et al., 2002) and lower the explosive potential of the eruption (Gonnermann and Manga, 2003).
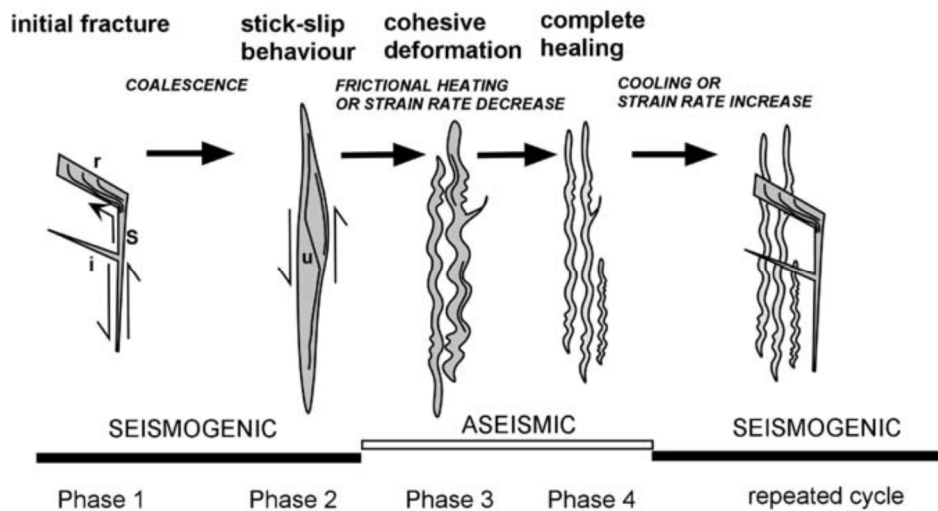
Figure 1-4. Cartoon illustrating the different phases of seismic cycles within rising magma. S corresponds to fault vein, I to injection vein, r to reservoir zone, and u to ultracataclasite zone (from Tuffen and Dingwell, 2005).
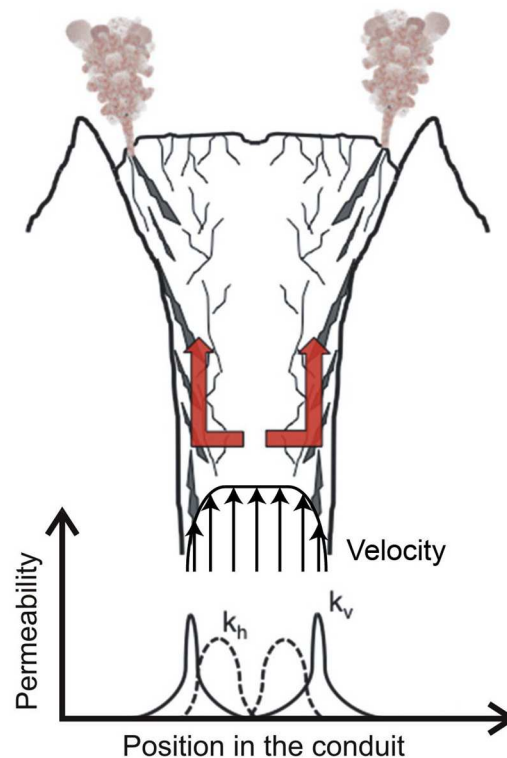
Figure 1-5. Architecture of permeable fracture network induced by strain localisation in magma. Localisation of strain induces an increase in permeability, promoting outward degassing (red arrows) toward the conduit margins; regions where the magma is subjected to the highest strain rate. Fractures subparallel to the flow direction favour the ascent of gas along the largest peripheral fractures (from Lavallée et al., 2013).

24

Figure 1-6 documents time-dependent cracking in crystalline magmas at constant stress in the approach to failure (Cordonnier et al. 2009). It demonstrates the wide transitional area between ductile magma deformation and brittle failure, which is the area inhabited by the bulk of ascending magma. Here, cracks nucleate, propagate and coalesce as catastrophic failure is approached, typically 2-3 orders of magnitude earlier than in pure silicate melt (Cordonnier et al., 2012; Gottsmann et al., 2009).
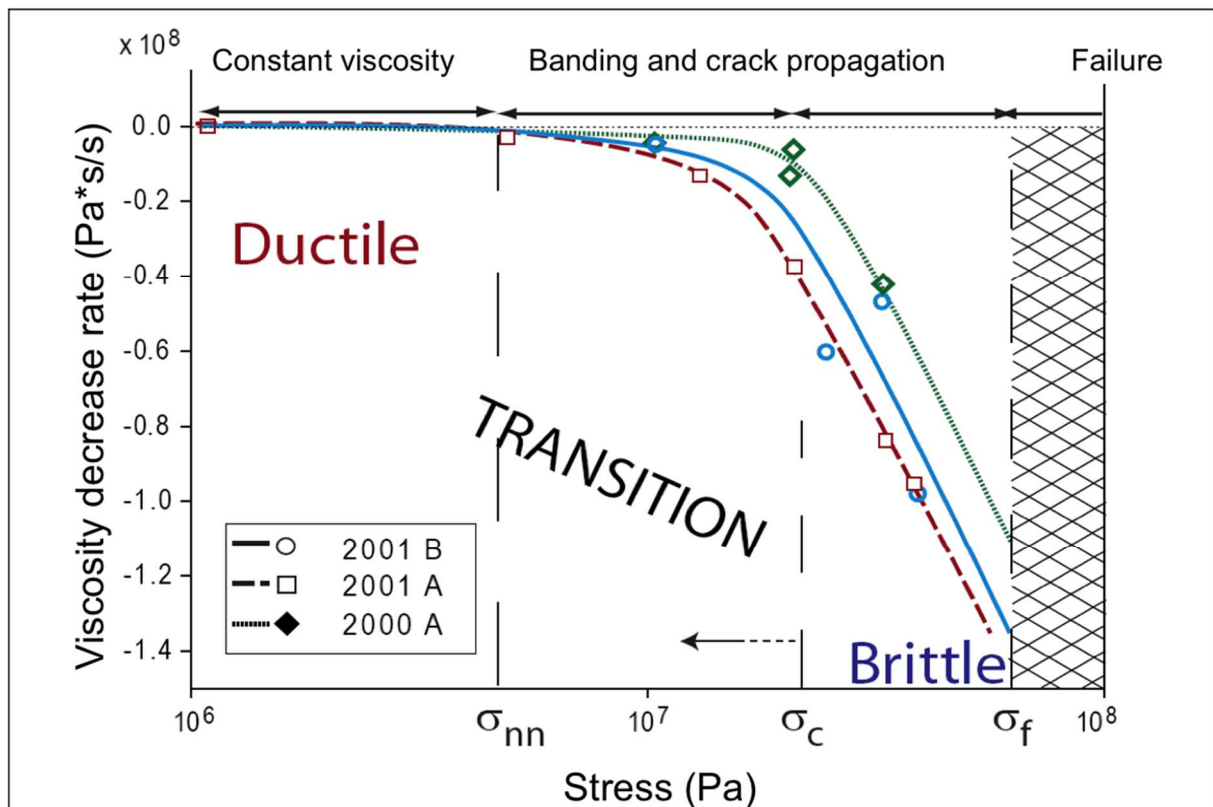
Figure 1-6. Viscosity variation rate at constant applied stress. Here, σ_{nn} is the onset of the time-weakening domain, σ_c is the onset of the brittle domain (where cracking alters the apparent viscosity) and σ_f provides the upper limit for the complete failure of the sample.

Strain localisation in hot, flowing magma during ascent alters the intrinsic strength of the magma by exploiting pre-existing weaknesses in the multi-phase (crystals, pores and silicate melt) magma. So the higher the crystallinity, the more pre-existing weaknesses exist and the lower the stress at failure. However, as previously mentioned, crystalline magma is strain-rate dependent, and hence the deformation rate dictates the failure stress and strain (Lavallée et al., 2013). This is depicted in Figure 1-7, where different strain rates were applied to the same sample type from Volcán de Colima (Mexico).
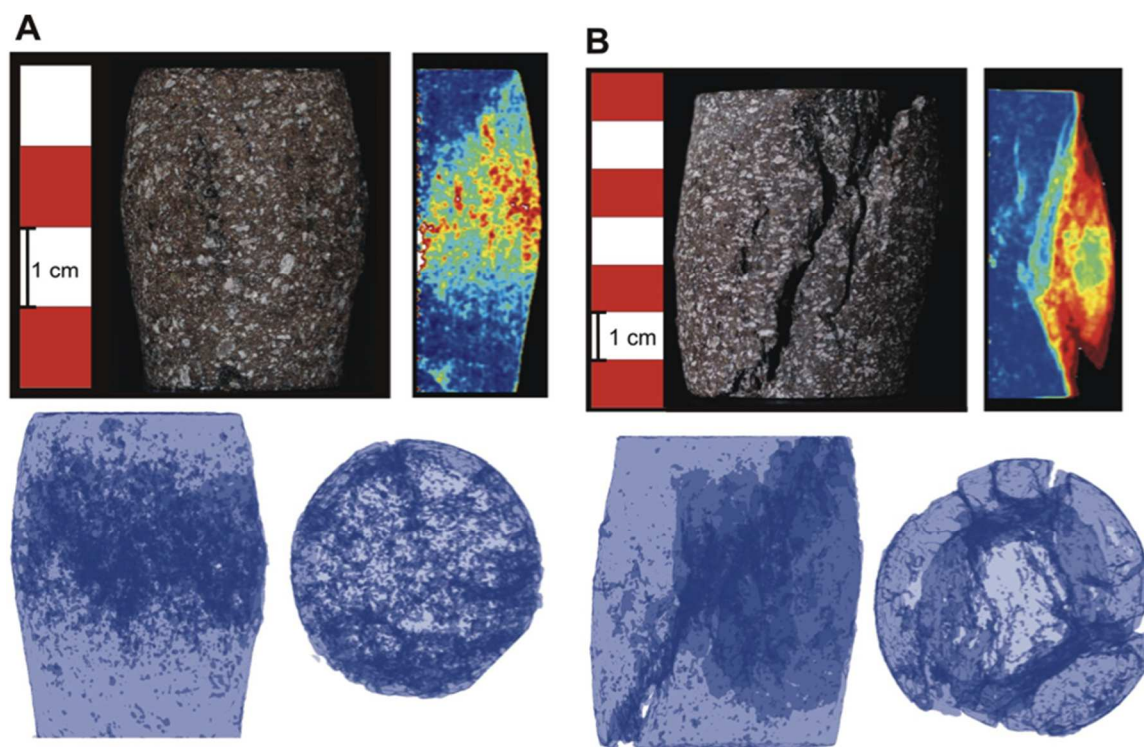
Figure 1-7. Fracture networks induced by magma failure. The photograph of each sample is accompanied by the neutron-computed tomography (NCT) reconstructions of the fracture network (below) and the modelled density of fractures (color-coded, where red is heavily fractured and blue is intact) represented in a half-space (right). (A) The sample deformed at 28.5 MPa shows a pervasive distribution of tensional fractures predominantly in the barrelled area. Shear fractures focus along an hourglass shape at an angle of ~45° from the principal compressive stress. (B) Sample deformed at 76 MPa with strongly localised shear fractures along an hourglass geometry at an angle of ~20° from the principal compressive stress (From Lavallée et al. 2013).

1.4. Shearing & rock friction

In volcanic environments, the transition from endogenous to exogenous growth can be attributed to a shift in magma rheology into the brittle regime (Hale and Wadge, 2008), and thus the ascent of high-viscosity magma can form discrete shear zones along conduit margins. The conduit margin during dome-building eruptions may be considered analogous to a seismogenic fault, owing to the elastic response of a highly viscous magma subjected to stress variations shorter than the structural relaxation timescale. For example, the morphology of the 2004-2008 Mount St. Helens lava dome is considered to be dependent upon structural controls

rather than magmatic processes (Vallance et al., 2008). Exogenic growth and formation of a spine necessarily results from dynamic rupture of the lava and the dome carapace along shear/ fault zones (Tuffen and Dingwell, 2005) with or without gouge formation (Kennedy and Russell, 2011). Much work exists on the dynamics of seismogenic faulting and the products exhumed by it in tectonic settings (Bell and Etheridge, 1973; Bell and Etheridge, 1976; Chester, 1994; Chester and Chester, 1998; Hippert and Hongn, 1998; Kim et al., 2010; Lin, 1996; Lin, 1999; O'Hara, 2001). However, shearing and faulting at active volcanoes may differ to tectonic faulting due to their distinct temperature conditions above those of the Earth's geotherm.
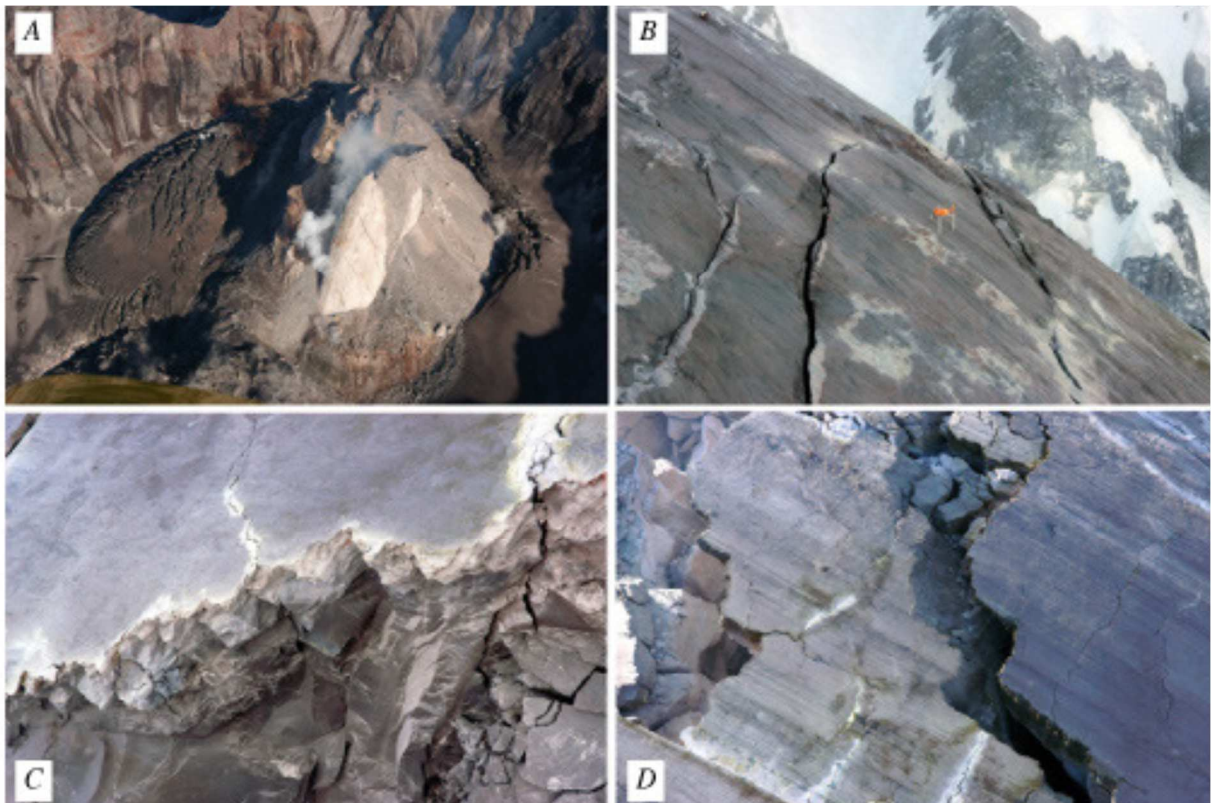
Figure 1-8. Features of the Mount St. Helens lava dome. USGS photos by J.S. Pallister. (A) Oblique aerial photograph of crater and 2004–2005 lava dome taken from the northwest on June 29, 2005. Spine 3 is in a shadow on the left; spine 4 is in the centre (highly fractured and altered); and spine 5 is on the right, with a white, striated gouge carapace on the north and west flanks, collapse scar on northwest face. The ash-covered Crater Glacier surrounds the dome. The following three photos were taken on January 14, 2005. (B)The striated surface of spine 4; direction of transport is from lower right to upper left. Orange box at centre 1 m long. (C) Contacts between gouge (grey, weathered surface lacking distinct striations), underlying cataclastic breccia, and dense dacite exposed on the collapsed south face of spine 4. Preserved thickness of gouge zone above contact is 1–2 m, although original thickness was greater. (D) Parallel striations on the surface of spine 4; transport direction

from lower right to upper left. Surface striations mark penetrative fabric that creates planar shear lamination of the cataclasite. Cashman et al. (2008).

Variations in fault-normal stresses result in seismogenic slip which produces wide-ranging fault products; from gouge, cataclasite, ultracataclasite, pseudotachylyte, mylonite and ultramylonite. The problem lies in understanding the differing conditions which result in faulting and the post-development influence of faulted rocks on slip behaviour (Ben-Zion and Sammis, 2003; Cowie and Scholz, 1992; Faulkner et al., 2011; Linker and Dieterich, 1992; Lyakhovsky and Ben-Zion, 2008; Marone and Richardson, 2010; Monzawa and Otsuki, 2003; Rempel, 2006; Scholz et al., 1993; Wells and Coppersmith, 1994).

Frictional sliding is velocity dependent and may be velocity strengthening (if resistance to sliding increases with increasing velocity) which promotes stable aseismic slip or velocity weakening (if resistance to sliding decreases with increasing velocity) i.e. likely to produce earthquake instabilities (Dieterich, 1979). Comminution during slip produces fault gouge, which is slip weakening (Ben-Zion and Sammis, 2003; Monzawa and Otsuki, 2003) due to powder lubrication (Reches and Lockner, 2010) and exhibits rate and state dependent behaviour (Abe et al., 2002; Dieterich and Kilgore, 1994; Nielsen et al., 2007; Samuelson et al., 2008). Gouge may be fluidised by dilation during rupture and form cataclasite which contains localised banding and flow textures (Chester and Chester, 1998; Monzawa and Otsuki, 2003). Extreme frictional processes may produce pseudotachylyte veins and injection structures which result from simultaneous frictional melting along the fault plane, and dynamic failure of the fault walls (Lin, 1996; O'Hara, 2001; Rempel, 2006; Spray, 2010; Swanson, 1992; Wenk, 1978). Pseudotachylyte generation greatly alters fault properties (Di Toro et al., 2006; Nielsen et al., 2010; Otsuki et al., 2003) such that viscous processes control the slip zone properties (Lavallée et al., 2012).

Mylonites display deformation partitioning and crystal-plastic processes which evolve into the stable-state microstructure and solution-transfer processes of ultramylonites (Hippert and Hongn, 1998) and are generally attributed to plastic / ductile deformation mechanisms (Bell and Etheridge, 1973; Handy et al., 1999; Herwegh and Handy, 1998), although they have been noted forming simultaneously with pseudotachylyte in the brittle regime (Kim et al., 2010; Passchier, 1982).
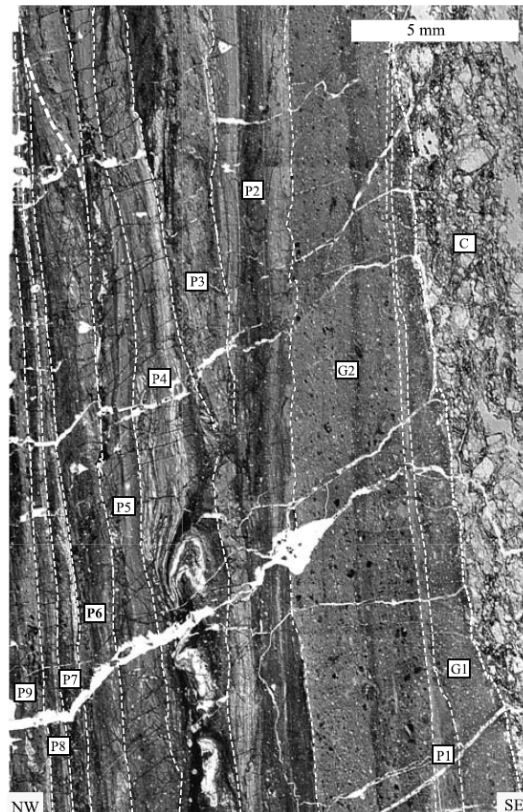
Figure 1-9. Photomicrograph of a thinly laminated fault rock. C: granitic cataclasite, G: fault gouge, and P: pseudotachylyte. Broken lines denote the boundaries between layers formed by different seismic slip events. A thick broken line in layer P6 indicates sinusoidal lamina (from Otsuki et al., 2003).

The difficulty with the characterisation of microstructures in natural fault rocks is that conditions such as temperature, strain rate and fluids likely fluctuated throughout formation and so cataclasites, mylonite, gouge and pseudotachylytes may coexist (Figure 1-9); hence identification requires a multi-disciplinary approach. Grain size and orientation analyses at macro- and micro-scale can identify brittle comminution (Monzawa and Otsuki, 2003), cataclastic banding (Chester and Chester, 1998), plastic rounding of phenocrysts, viscous deformation patterns (Herwegh and Handy, 1998) or recrystallization from frictional melting (Lin, 1999). For example pseudotachylytes form in a wide variety of host rocks in shallow crustal settings which results in fast quenching and crystallisation- to form distinctive microscopic textures (Otsuki et al., 2003) and compositions (Altenberger et al., 2010; Curewitz and Karson, 1999; Spray, 2010). Chemical analyses may identify changes in mineral compositions which result from melting (Spray, 1992) or deformation, including recrystallisation (Bell and Etheridge, 1976). Additionally, rheological distinctions between

fault rocks and their host rock may allude to the process of formation (Moecher and Steltenpohl, 2009; Taira et al., 2008).

Domain state analysis magnetic tests may also be important in revealing the thermal history and identifying the occurrence of frictional melting as a result of coseismic slip. Previous magnetic studies (Ferré et al., 2005; Freund et al., 2007; Nakamura et al., 2002) have shown differences in various rock-magnetic parameters between re-melted fault rocks (pseudotachylytes) and their host rock. For example Ferre et al. (2005) measured a 10 to 20-fold increase in low field magnetic susceptibility and the natural remanent magnetisation (NRM) of the pseudotachylyte was up to 300 times stronger than the one of the granitic host rock. In their laboratory experiments on artificial pseudotachylyte Nakamura et al. (2002) detected submicron inclusions of weakly interacting single-domain to pseudo-single-domain magnetite that was not present in the undeformed granite protolith and which resulted from oxidation of ferro-magnesian silicates during the melt-quench event.

In volcanic settings there is significant documentation of gouge and cataclasite formation at the conduit margin (Kennedy and Russell, 2011; Kennedy et al., 2009; Moore et al., 2008) and preserved on the spine surface (Figure 1-8). Pseudotachylytes have, until now, rarely been noted in volcanic environments. This is despite the simultaneous occurrence of large stress-strain fluctuations as well as intense events of mass transfer (e.g., magma ascent, sector collapse, caldera collapse, block and ash flows). During the onset of an eruption, high strain rates in the ascending magma lead to strain localisation and the formation of shear zones along the shallow conduit margin, where shear stresses are highest (Hale and Wadge, 2008). The shear zone can propagate deeper (Cashman et al. 2008) as the extruding magma continues to take the path of least resistance within the already sheared conduit walls. The stress required for shear sliding is believed to be lower than that required to initiate new fractures within intact host rocks (Scholz, 1998) even considering fault healing (Sparks 1999, Tuffen et al. 2003, Tuffen and Dingwell 2005) which would result in strengthening of the fault zone (Di Toro et al., 2006; Mizoguchi et al., 2006). Repeated slip events along the conduit margin leads to the formation of a gouge and cataclasite layer on the spine surfaces (Cashman et al. 2008) resulting in unstable, velocity weakening slip (Otsuki et al., 2003). Temporal development in fault zone products may be a result of locally fluctuating stresses (e.g. thinning of the shear zone would locally increase strain and strain rate (Smith et al., 2011)) or an influx of fluids, and the evolving

conditions could favour a shift into plastic mylonite formation or even facilitate frictional melting during the extrusion of highly viscous magma spines.
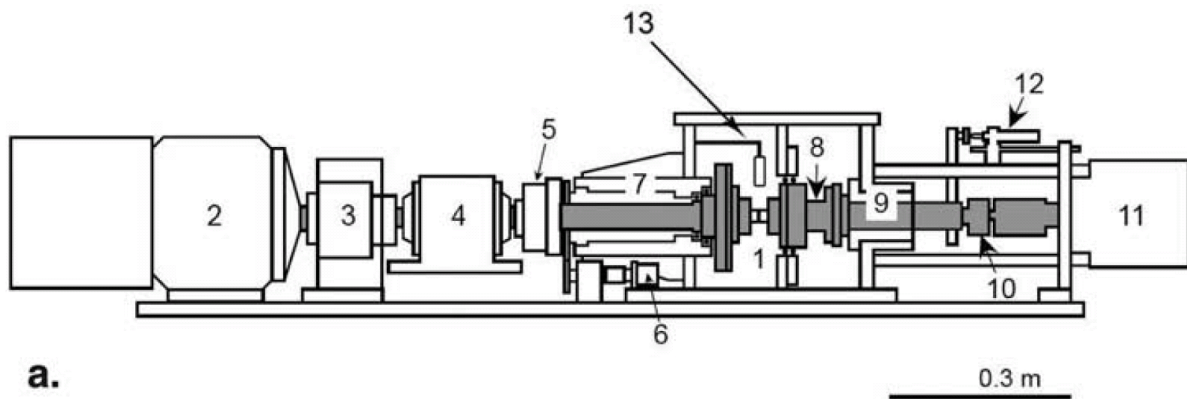
Figure 1-10. High-velocity rotary shear apparatus. Simplified sketch of the high-velocity frictional testing machine, where: 1, sample; 2, motor; 3, torque limiter; 4, torque gauge; 5, electromagnetic clutch; 6, rotary encoder; 7, rotary column; 8, torque-axial force gauge; 9, spline; 10, axial force gauge; 11, air actuator; 12, displacement transducer; 13, moisture sensor. Modified from Brantut et al. (2008).

Quantification of the conditions under which fault rocks form is possible by recreating natural samples with laboratory experiments. Room-temperature and –pressure conditions facilitate the production of gouge and cataclasite entirely within the brittle regime (Chester and Chester, 1998; Kennedy et al., 2009) while mylonite production in the ductile / plastic regime usually requires confining pressure and higher temperatures (Handy et al., 1999). High-velocity rotary shear (HVR) experiments (Figure 1-10) on volcanic rocks demonstrate the propensity for frictional melting after ~1m slip at upper conduit conditions, indicating that pseudotachylyte may be a common product of viscous magma ascent (Lavallée et al., 2012) which could have important implications for magma ascent and eruptions.

I had a dream, which was not all a dream.
The bright sun was extinguish'd, and the stars
Did wander darkling in the eternal space,
Rayless, and pathless, and the icy earth
Swung blind and blackening in the moonless air;
Morn came and went--and came, and brought no day,
…
Happy were those who dwelt within the eye
Of the volcanos, and their mountain-torch:
A fearful hope was all the world contain'd;
…

-Excerpt from Darkness, Lord Byron

Chapter 2

Tracking the permeable porous network during strain-dependent magmatic flow

Rheological variations have been postulated as the cause of transitions from effusive to explosive volcanic eruption style. Rheology is integrally linked to the composition and textural state (porosity, crystallinity) of magma as well as the stress, temperature and strain rate operative during flow. This study characterises the rheological behaviour and, importantly, the evolution of physical properties of two magmas (with different crystallinity and porosity) from Volcán de Colima (Mexico) - a volcanic system known for its rapid fluctuations in eruption style.

Magma samples deformed in a uniaxial press at a constant stress of 2.8, 12 or 24 MPa, a constant temperature of 940- 945 $^{\circ}$C (comparable to upper conduit or lava dome conditions) to strains of 20 or 30 % displayed different mechanical behaviour and significant differences in measured strain rates (10^{-2}-10^{-5} s^{-1}). The evolution of porosity, permeability, dynamic Young's modulus and dynamic Poisson's ratio point to a complex evolution of the samples, comprising initial strengthening and subsequent weakening manifested as strain-hardening, visco-elastic, constant-rate and strain-weakening deformation. Both magmas behave as shear-thinning non-Newtonian liquids and viscosity decreases as a function of strain in "strain-dependent" deformation.

We find that strain localisation during deformation leads to the rearrangement / closure of void space (a combination of pores and cracks) followed by preferentially aligned (in the direction of the maximum principal stress) fracturing in damage zones and the densification of other areas. In a dome setting, highly viscous, low permeability magmas carry the potential to block volcanic conduits with a magma plug, resulting in the build-up of pressures in the conduit. Above a certain threshold of strain (dependent upon stress / strain rate), the initiation, propagation and coalescence of micro-fractures leads to mechanical degradation of the magma samples, which then supersedes magmatic flow and crystal rearrangement as the dominant form of deformation. This results in lower apparent viscosities than those anticipated from magmatic state, especially at high strain rates. In a lava dome, this could result in dome collapse and the concomitant depressurisation could trigger an explosive eruption.

2.1. Introduction

2.1.1. Motivation

The frequent and as yet unpredictable transition from effusive to explosive volcanic behaviour is common to active composite volcanoes, yet our understanding of the processes which control this evolution is poor. The rheology of magma, dictated by its composition, porosity and crystal content, is integral to eruption behaviour (Caricchi et al., 2007; Cordonnier et al., 2009; Lavallée et al., 2007; Lejeune and Richet, 1995; McBirney and Murase, 1984; Petford, 2003). Indeed, rheological variations have previously been cited as the cause of effusive-explosive transitions on multiple timescales (Cordonnier et al., 2009; D'Oriano et al., 2005; Dingwell, 1996; Divoux et al., 2011; Lavallée et al., 2008). Fragmentation and explosive eruptions result from the brittle failure of magma at high temperature (Lavallée et al., 2008; Smith et al., 2011; Tuffen et al., 2008) and for a given material, the transition into the brittle regime is initiated by a decrease in temperature or increase in shear stress or strain rate (Dingwell and Webb, 1989; Lavallée et al., 2007; Webb and Dingwell, 1990).

Laboratory experiments which aim to simulate realistic volcanic conditions permit the controlled study of volcanic processes (Cordonnier et al., 2009; Heap et al., 2011; Heap et al., 2009; Hess et al., 2007; Kennedy et al., 2005; Lavallée et al., 2008; Pallister et al., 1992; Smith et al., 2005; Smith et al., 2011; Tuffen et al., 2003; Tuffen et al., 2008) and aid the development of models to describe the behaviour of magmas in conduit and dome settings (Caricchi et al., 2007; Costa et al., 2009; Deubelbeiss et al., 2011; Lavallée et al., 2007; Melnik, 2001; Melnik and Sparks, 1999). Experiments on magma show that the addition of crystals to a melt increases viscosity at low strain rates. At low crystallinity (<40 %), this non-linear increase has been described by the Einstein-Roscoe equation (Roscoe, 1952), parameterised by Marsh (1981). Beyond a threshold of crystallinity (related to the maximum packing fraction, which in itself is dependent upon the size, shape and distribution of the suspended crystals (Cimarelli et al., 2011; Picard et al., 2011)) particle-particle interaction permits the transmission of stress via the solid fraction (Petford, 2003) resulting in non-Newtonian rheological behaviour (Caricchi et al., 2007; Carreau et al., 1999; Cordonnier et al., 2009; Deubelbeiss et al., 2011; Lavallée et al., 2007; Lejeune and Richet, 1995). Lavallée et al. (2007) present a rheological law for this non-Newtonian behaviour based on experiments on a wide range of natural magmas which contain a fully connected crystal structure.

In this study we track the damage evolution in experimentally deformed natural magmas for the first time. A magmas ability to degas through the permeable porous network and its propensity for fragmentation are integrally linked to the physical state of the magma, which must be better understood to predict volcanic behaviour. The samples chosen are from Volcán de Colima, a volcano which experiences regular transitions in eruption style, and the properties of the magmas are studied using porosity and permeability measurements, X-ray fluorescence, scanning electron microscopy, thin section analysis, X-ray computed tomography and differential scanning calorimetry. Dynamic Young's modulus and Poisson's ratio are calculated (from ultrasonic wave velocity measurements) for the starting materials and deformed cores (these contrast to static moduli which are calculated using the stress-strain response of a sample under constant strain rate, and as a result, are frequency-dependent (see (Heap et al., 2010) and references therein)).

2.1.2. *Volcán de Colima, History and Erupted Products*

Volcán de Colima is an active volcano which, together with the extinct Nevado de Colima, forms the Colima Volcanic Complex, located in the Trans-Mexican Volcanic Belt. The current eruptive period is inferred to be drawing to a close and is part of a ~100-year cycle of explosive to effusive events which culminate in Plinian eruptions (Breton et al., 2002; Luhr, 2002; Luhr and Carmichael, 1980). The current period of activity was marked at its onset by an increase in volcano-tectonic (VT) seismicity which began in November 1997 (Dominguez et al., 2001; Navarro-Ochoa et al., 2002; Zobin et al., 2002), and which was swiftly followed by a dome-building episode and multiple lava flows (in November 1998). This transitioned into periodic explosive behaviour in 1999 and early 2001, and formed a summit crater. Subsequently, effusive behaviour recommenced forming a lava dome, which eventually overflowed the crater in February 2002, forming a lava flow (Lavallée et al., 2011). In March 2003 the eruption once again transitioned to explosive behaviour, whereby repeated Vulcanian explosions occurred over 18 months. These subsided as a new phase of block-lava extrusion occurred during late 2004 (Zobin et al., 2008), but resumed in December 2004. During May and June 2005, following numerous swarms of long period (LP) events which indicated ascending magma (Arámbula-Mendoza et al., 2011; Varley et al., 2010), a number of dome-building eruptions and larger Vulcanian events occurred, with associated column collapses and pyroclastic flows (Gavilanes-Ruiz et al., 2009). A new dome began to form in early 2007,

which in early 2010 was reported to have been growing by 2000 m^2 per day and eventually overflowed the crater rim (Lavallée et al., 2011). During late 2010 multiple incandescent landslides travelled down the North, South and Western flanks of the volcano. In January 2011 "dust plumes" from landslides were sighted over the 2.6 million m^3 lava dome, which finally stopped growing in June 2011, but speculation is rife as to whether this marks the end of the eruption or simply a quiescent pause.

Despite the frequent fluctuations in eruptive style at Volcán de Colima, there is little variation in the erupted products, which tend to be highly crystalline, intermediate, andesitic lavas (Mora et al., 2002; Valdez-Moreno et al., 2006). Lavallée et al. (2011) found that recent dome lavas contain approximately 30 vol. % phenocrysts, 25-50 vol. % microlites and 14-45 vol. % glass. Porosity is highly variable between 1 and 30 % (Kolzenburg et al., 2012; Lavallée et al., 2011), with a bimodal distribution showing peaks at 12 and 26 % (Lavallée et al., 2011). Plagioclase, diopside and hypersthene dominate the crystal assemblage, forming a porphyritic texture. Hornblende phenocrysts occur sporadically and olivine and iron-titanium oxides occur as xenocrysts, all of which reside in a peraluminous, rhyolitic interstitial glass. Exceptions are the more mafic (Luhr, 2002; Luhr and Carmichael, 1990; Savov et al., 2008) culminating explosive eruptions of the 100-year cycles (González et al., 2002), which are attributed to the influx of mafic magma into the magma chamber from a deeper reservoir. Magma is largely degassed by the time it reaches the surface, and Atlas et al. (2006) suggest vapour-saturated crystallisation during ascent at depths of less than 12 km. Melt inclusions measure H_2O concentrations of 0.1 to 2.5 wt. % and CO_2 concentrations of up to 800 ppm (Reubi and Blundy, 2008), indicating trapping conditions of 10-150 MPa and 959-1015 °C. Correspondingly, Savoy et al. (2008) suggest storage temperatures of 960-1020 °C based on geothermometry of pyroxenes.

2.2. Method

2.2.1. Sample Selection

The two sample materials chosen for this study are the andesites COL-B2 and COL-LAH4 (Table 2-1, Figure 2-1 A and E) from the dome-building eruptions and explosions that occurred during 2004. The two sample materials were selected on the basis of their contrasting initial porosities and crystal contents. The two lavas contain 9.5 and 27.2 % porosity (a combination

of cracks and pores), 34 and 20 % phenocrysts, 31 and 23 % microlites, and 26 and 30 % interstitial melt for B2 and LAH4, respectively.
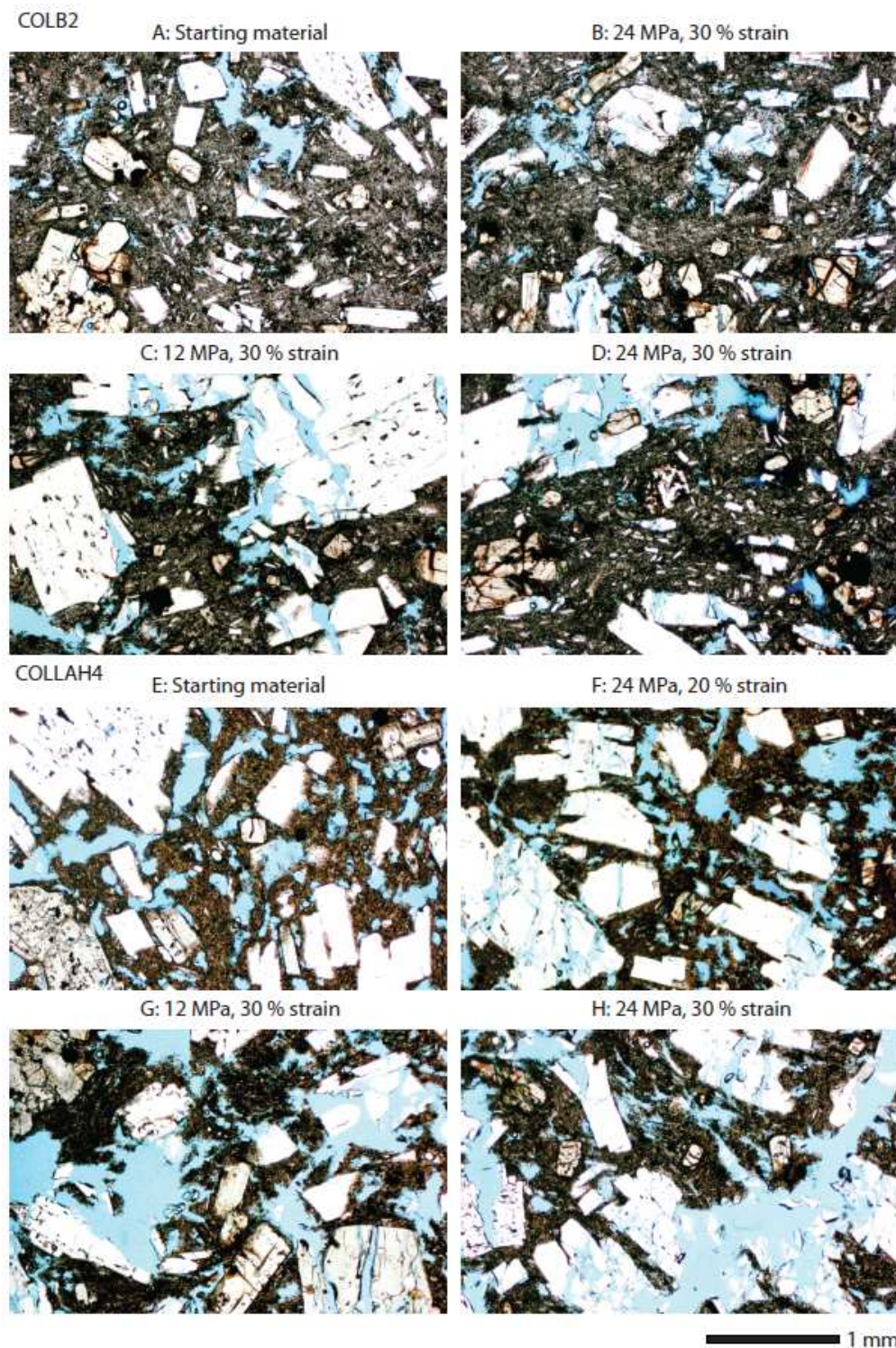
Figure 2-1. Damage evolution: Photomicrographs to show the appearance of Colima samples B2 (A-D) and LAH4 (E-H), and the evolution of phenocrysts, microlites, interstitial glass and pores / cracks after deformation.

The andesites from this particular eruptive period are isotropic, evidenced both seismically (by use of ultrasonic wave velocity measurements) and optically (by thin section and tomographic imaging). The glass transition temperatures (T_g) established by differential scanning calorimetry (DSC) at a heating / cooling rate of 10 °C per minute, are 746 ±3 °C for B2 and 751 ±3 °C for LAH4. Rheological measurements are used to track the non-Newtonian viscosity using experiments at realistic volcanic conditions and for comparison with complementary microstructural data.

*Table 2-1. Geochemical composition of bulk rock and interstitial glass for both samples normalised to 100%. *[1] Measured by X-ray fluorescence and *[2] measured by wavelength dispersive analysis in a CAMECA SX100 scanning electron microprobe. Where $_t$ = total.*

Sample	SiO2	Al2O3	FeO$_t$	MnO	MgO	CaO	Na2O	K2O	TiO2	P2O5	PF	Total
B2 bulk*[1]	60.93	17.95	5.15	0.10	2.83	5.82	4.76	1.34	0.60	0.20	0.32	100.00
B2 glass*[2]	73.35	13.37	2.14	0.04	0.24	1.70	5.10	2.90	0.67	0.08	-	100.00
LAH4 bulk*[1]	59.48	17.56	5.55	0.11	4.07	6.66	4.55	1.20	0.62	0.19	0.00	100.00
LAH4 glass*[2]	74.20	12.88	2.14	0.04	0.44	1.81	4.45	3.05	0.59	0.31	-	100.00

2.2.2. Viscosity Press

A high-temperature uniaxial press (Figure 2-2) was used to study the rheological evolution of crystalline andesite from Volcán de Colima under different applied stresses (see Hess et al. (2007) for experimental setup and procedure). Cylindrical samples 50 mm in length with 25 mm diameter (aspect ratio of 2:1, as per the guidelines of (Hawkins, 1998)) were heated at a furnace heating rate of 2 °C / min until the sample was at a steady 940-945 °C (measured using a thermocouple in the centre of the sample). This heating rate allows ample time for equilibration of the system in order to minimise the effect of thermal gradients (see (Yong and Wang, 1980)). The desired load of 1.4, 6 or 12 kN (which equates to stresses of 2.8, 12 or 24 MPa for the chosen sample size) was applied instantaneously and displacement measured at a rate of 10 measurements per second to 10 or 15 mm axial displacement (20 and 30 % strain). After deformation the samples were then cored back into cylinders of 25mm (removing the lateral bulge) before measuring the physical properties.
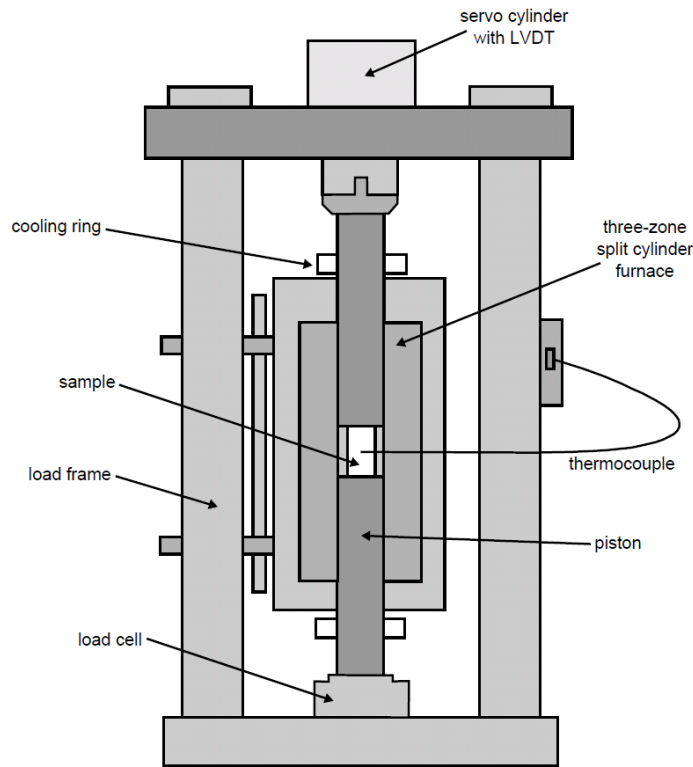
Figure 2-2. Deformation apparatus: Schematic diagram of the high-temperature uniaxial press used for the deformation experiments and viscosity measurements at Ludwig-Maximilians-Universität, Munich.

2.2.3. Physical Property Characterisation

Thin sections and tomographic images were made from the starting materials and the deformed cores. 3D high-resolution tomography images were acquired through v/tome/x s 240 micro-CT scanner from GE phoenix using a high-power X-ray tube and a drx-250 rt detector system (experimental conditions: Pixel / Voxel size: 30.0 µm, 1000 images for 360° (average of 3 single images, one image skipped), exposure time of 1 s, voltage of 80 kV and current of 250 µA). Connected porosity was measured via the Archimedes buoyancy method (Guéguen and Palciauskas, 1994). Water (distilled) permeability was measured in a servo-controlled steady-state-flow permeameter in the Rock & Ice Physics Laboratory at University College London (see also (Kolzenburg et al., 2012)) under effective pressures of 5 – 50 MPa (Figure 2-3). For the purpose of this study we assume that the effective pressure is simply the confining pressure minus the pore fluid pressure (i.e. we assume that the poro-elastic constant α is equal to one, see Guéguen and Palciauskas, 1994). The "upstream" (P_{up}) and "downstream" (P_{down}) pore fluid pressures were 9.5 MPa and 10.5 MPa, respectively (i.e., there was a 1 MPa pressure differential

across the sample). Once steady-state flow had been established, water permeability (κ_{water}) was calculated using Darcy's law:

$$Q / A = \kappa_{water} / \eta L (P_{up} - P_{down}) \qquad \text{(Eq. 2)}$$

where Q is the volume of fluid measured per unit time, A is the cross-sectional area of the sample, η is the viscosity of the pore fluid, and L is the length of the sample.

Bench-top ultrasonic wave velocity measurements, i.e. P- (V_p) and S-waves (V_s), were made on nominally-dry samples (vacuum dried at 40 °C) at the Laboratoire de Déformation des Roches (Strasbourg) and used to calculate dynamic Young's modulus (Eq. 3) and dynamic Poisson's ratio (Eq. 4):

$$E_d = \rho \, V_s^2 \, (3V_p^2 - 4V_s^2) / (V_p^2 - V_s^2) \qquad \text{(Eq. 3)}$$

$$\nu_d = (V_p^2 - 2V_s^2) / (2V_p^2 - 2V_s^2) \qquad \text{(Eq. 4)}$$

where E_d is Young's modulus, ρ is the bulk sample density and ν_d is Poisson's ratio. We note that the flow direction for our permeability measurements and the propagation direction for our elastic wave measurements are parallel to the maximum principal stress (i.e. the direction of loading) in our deformation experiments.
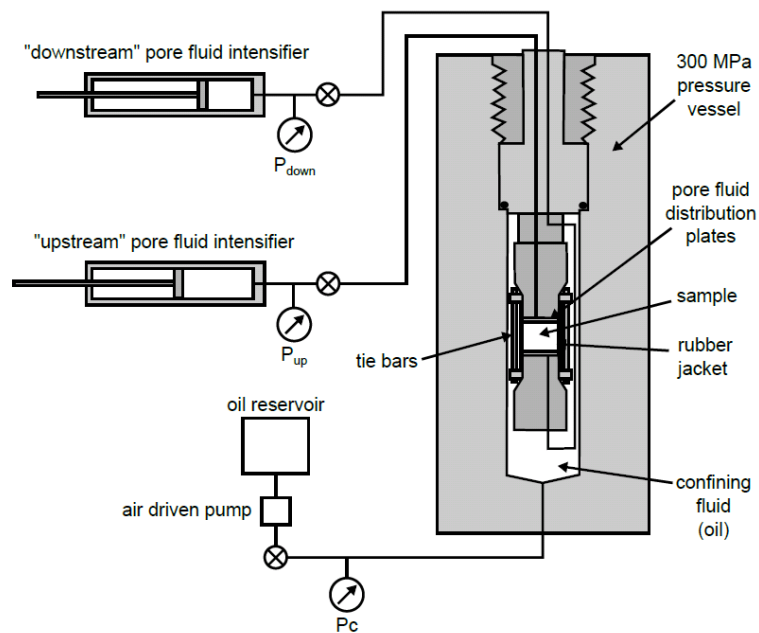
Figure 2-3. Schematic diagram of the permeameter at University College London.

2.3. Results

2.3.1. Magma Rheology

The two magmas deform differently at any given temperature and applied stress, with resultant strain rates varying between 10^{-2} and 10^{-5} s^{-1} (Figure 2-4). Strain rates are always higher at higher stress, and higher for LAH4 (10^{-2} to 10^{-4} s^{-1}) than for B2 (10^{-3} to 10^{-5} s^{-1}) under the same applied stress. Thus LAH4 is either weaker or less viscous. A difference in the evolution of strain rate with increasing total strain presents an interesting contrast between samples. All of the magma deformation experiments show initial reduction in strain rate with increasing strain, known as strain-hardening (Figure 2-5). Under just 2.8 MPa of stress, both samples continue to exhibit strain-hardening until at least 20 % strain, though the effect lessens as total strain increases and the total effect is larger for B2 (Figure 2-5a). For B2 strain hardening transitions to constant strain rate deformation at ~5 % and ~3 % strain at 12 and 24 MPa, respectively, and continues to a total strain of up to 30 %. For LAH4, strain hardening ends at 1-2 % strain and deformation proceeds at a constant strain rate, however, at 24 MPa this further transitions into strain-weakening behaviour at ~25 % strain (Figure 2-5a). This is an indication that B2 and LAH have significantly different mechanical properties, which, given the similarity in composition and T_g, must relate to the structural attributes of the samples, including crystal content, crystal size distribution and porosity (including pore size / shape distribution and pore versus crack porosity).
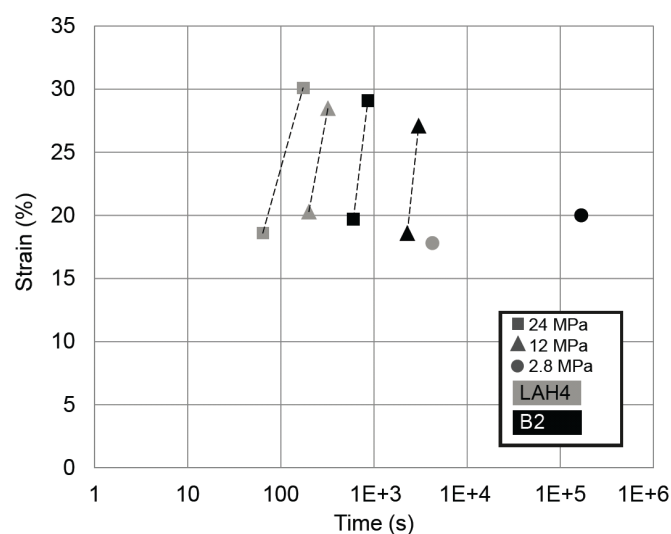
Figure 2-4. Experimental timescale: The timescales of different high-temperature uniaxial deformation experiments for samples B2 and LAH4 under 2.8, 12 or 24 MPa stress.
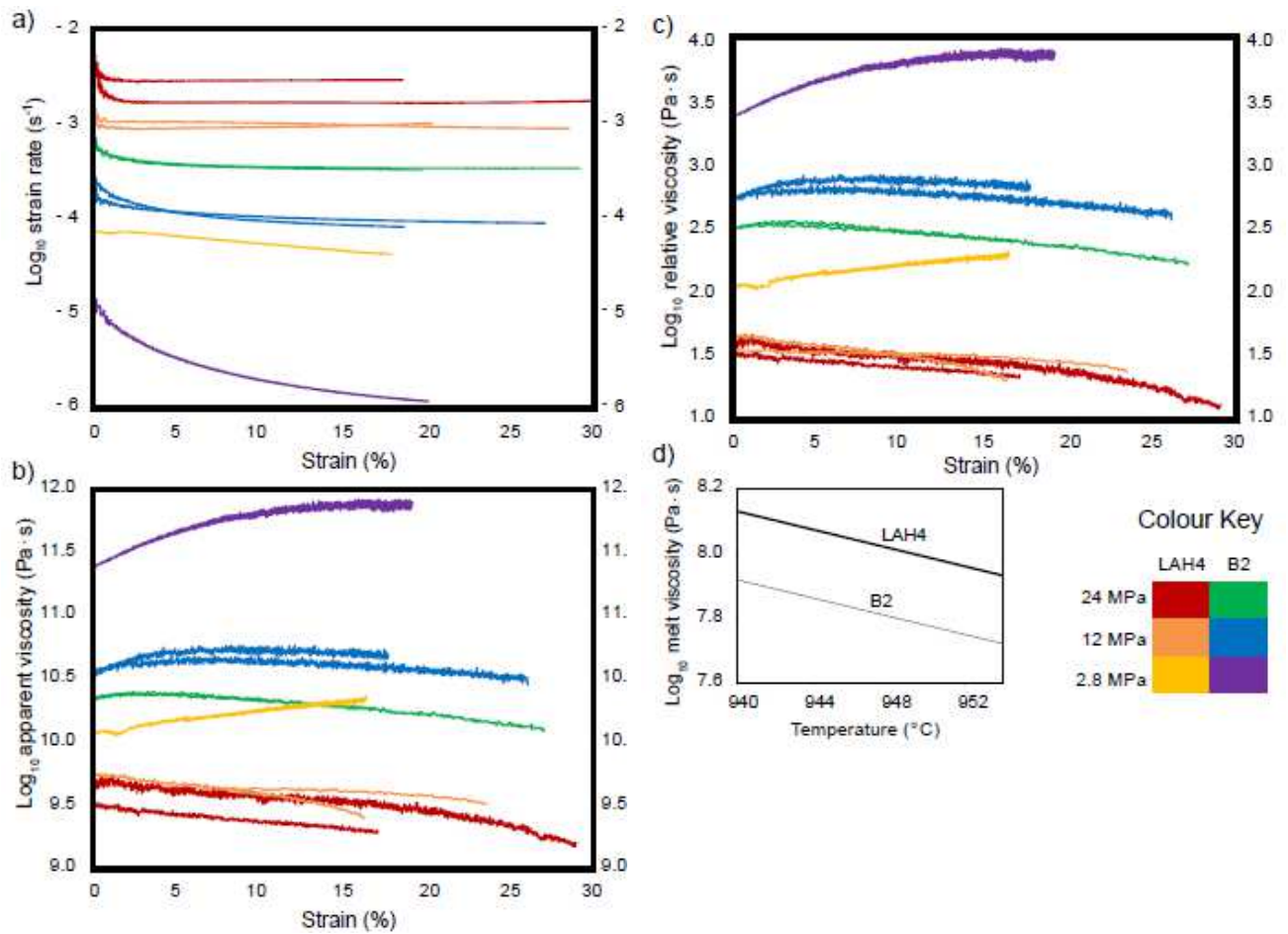
Figure 2-5 Rheological development: a) The evolution of strain rate with total strain for samples B2 and LAH4 under 2.8, 12 and 24 MPa stress. b) Rheological behaviour of samples B2 and LAH4 under 2.8, 12 and 24 MPa stress, showing the changing apparent viscosity as a function of total strain. c) "Strain-dependent" deformation; relative viscosity as a function of strain, with the effect of temperature excluded shows concomitant deformation rate independent of stress and crystallinity. d) Interstitial melt viscosities over the experimental temperature range as calculated from the GRD viscosity model (Giordano et al., 2008) using glass chemical composition established by WDA.

The apparent viscosity (η_a) of the samples during flow was calculated using Eq. 5 from Gent (1960), where F is the force (in N), h is the change in length during the experiment (in m), V is the initial volume of the sample (in m^3) and t is time (in s):

$$\eta_a = 2\pi \, Fh^5 / 3V \, ((dh / dt) \, 2\pi h^3 + V) \tag{Eq. 5}$$

Under the same applied stress, apparent viscosity was higher in B2 (10^{10} to 10^{11} Pa·s) than in LAH4 (10^9 to 10^{10} Pa·s) (Figure 2-5b). For both samples the viscosity was lower at higher

44

applied stress, demonstrating dominantly pseudo-plastic (shear-thinning) material characteristics (Caricchi et al., 2007; Cordonnier et al., 2009; Lavallée et al., 2011). Both B2 and LAH4 exhibit strain-hardening behaviour to at least 20 % strain at just 2.8 MPa (Figure 2-5b). At 12 and 24 MPa this does not occur in LAH4 and persists to less than 5 % strain in B2, after which viscosity decreases over time (and strain, Figure 2-5b), a phenomenon termed "time-dependent" deformation (Cordonnier et al., 2009). For sample LAH4 at 24 MPa there is an acceleration in the rate of viscosity decrease after 25 % strain, concordant to the slight increase in strain rate (Figure 2-5a).

The non-Newtonian character of the melt is further investigated by plotting the relative viscosity against strain (Figure 2-5c), which isolates the effect of crystal content from the temperature dependence (Lejeune and Richet, 1995). The relative viscosity (η_r) relates the apparent viscosity (η_{app}) of the sample to the viscosity of the melt (n_{melt}) in Eq. 6:

$$\eta_r = \eta_{app} / \eta_{melt} \qquad \text{(Eq. 6)}$$

where η_{melt} was calculated for the experimental temperature range using the GRD viscosity model (Giordano et al., 2008) from chemical composition of the interstitial melt (measured by WDA, Table 2-1).
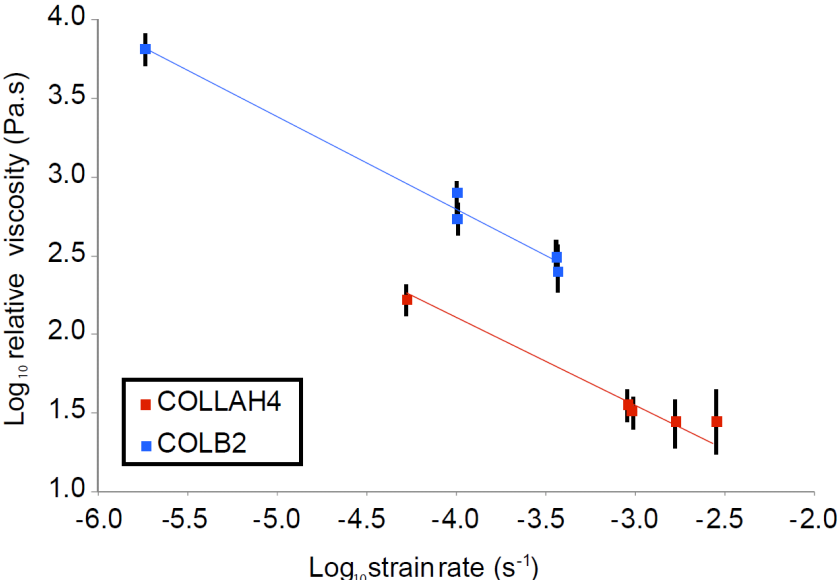
Figure 2-6. Viscosity variation with strain rate: The change in relative viscosity with strain rate depicts a linear negative trend for both samples under the investigated range, evidence of the shear-thinning behaviour of magma.

We find that the relative viscosity is always higher for B2 than LAH4 (Figure 2-6), due to the higher apparent viscosity (Figure 2-5b) and lower interstitial melt viscosity of B2 (Figure 2-5d). The strain-hardening behaviour of the low-stress experiments (2.8 MPa) and the shear-thinning effect of the higher-stress experiments (12-24 MPa), reveal similar trends for both samples when plotted against strain (it is not dependent upon crystal content within the ranges measured, Figure 2-5c), indicating that, as different applied stresses resulted in such different timescales of experiments (Figure 2-4) the degradation, deformation and structural reorganisation of magma (Figure 2-7) may be strain, rather than time, dependent.
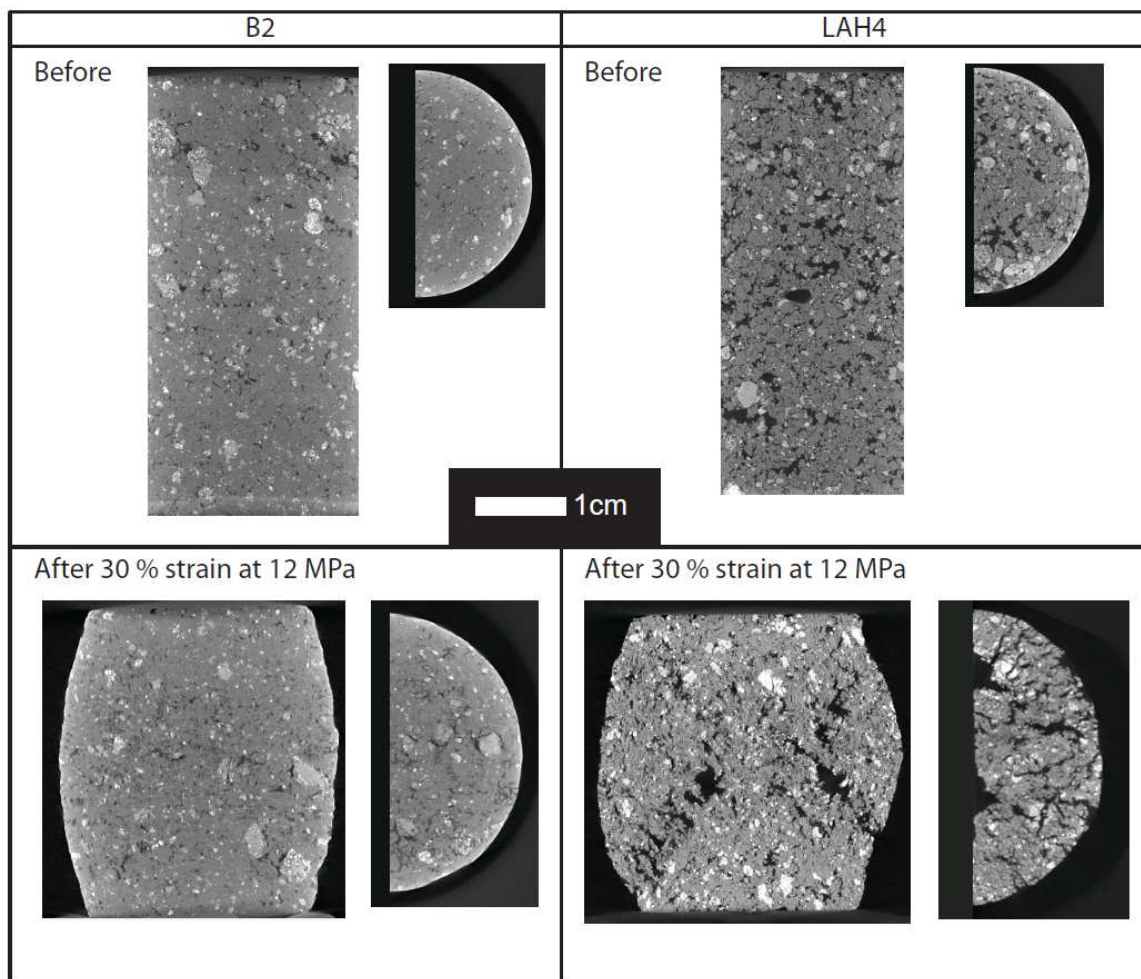
Figure 2-7. 3D reorganisation due to deformation: X-ray computed tomography images of starting materials and cores deformed to 30 % strain at 12 MPa. Images show a vertical and horizontal cross section and are to scale, highlighting the shortening and extensive lateral expansion of the deformed samples. The reorganisation of pore space is clear in both samples, and in LAH4 2 clear damage zones are seen running diagonally through the sample.

In order to verify our findings, the data from Lavallée et al. (2011) were incorporated with those from this study in Figure 2-8. We find that the resultant strain rate for samples B2 and LAH4 under a given applied stress at known temperature is in accordance with previous data (within the errors stated in Lavallée et al. (2011)). It thus follows that the non-Newtonian exponent of 0.5, and the rheological relationship between strain (σ), strain rate (γ) and temperature above the glass transition (T-T_g), stated by Lavallée et al. (2011) in Eq. 6 are therefore likely to be applicable to these magmas:

$$Log\sigma = 0.5 Log\gamma + 606.9 / T - T_g + 0.29 \qquad \text{(Eq. 6)}$$

The data for sample LAH4 falls slightly below and B2 falls slightly above the predicted viscosities (within the error stated in Lavallée et al. (2007)), a difference surely caused by the different structural properties of the samples (as clearly evidenced in Figures 2-1 and 2-7), which may have a larger impact than previously acknowledged.
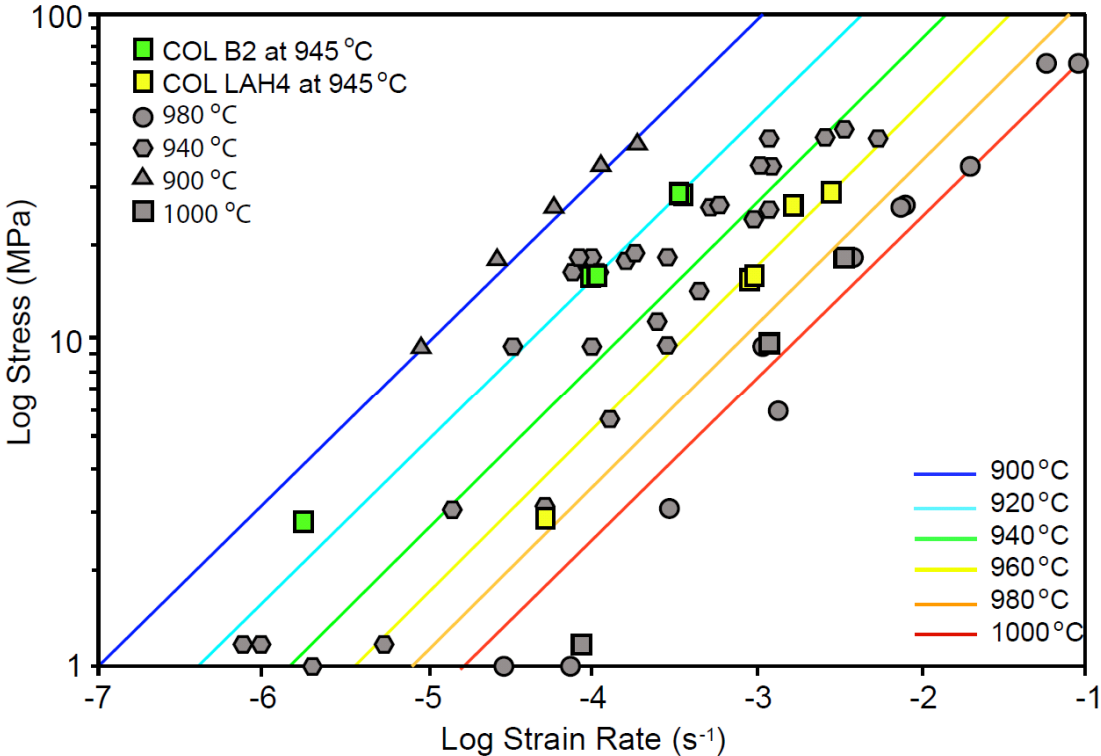
Figure 2-8. Shear-thinning behaviour of magma: Shear-thinning effect evidenced by the linear relationship of Log stress versus Log strain rate established by (and including data in grey from) Lavallée et al. (2011). Sample LAH4 has a lower viscosity than expected and B2 has a slightly higher viscosity, highlighting the importance of understanding the physical magma properties.

2.3.2. Physical properties

The evolution of porosity, dynamic Young's modulus, dynamic Poisson's ratio (Figure 2-9) and permeability (Figure 2-10) with changing deformation quantifies the damage induced by high-temperature uniaxial compression depicted in the tomography images (Figure 2-7). For B2 high-temperature uniaxial deformation leads to an increase in porosity, whereas for LAH4 porosity is decreased under 12 MPa to 20 % strain. The 12 MPa and 20 % strain experiments did not change permeability (although the sample of LAH4 lost its cohesion at an effective pressure of 20 MPa during the permeability measurements, Figure 2-10), and Poisson's ratio decreased and Young's modulus increased (Figure 2-9), indicating stiffening of the material in the axial direction.
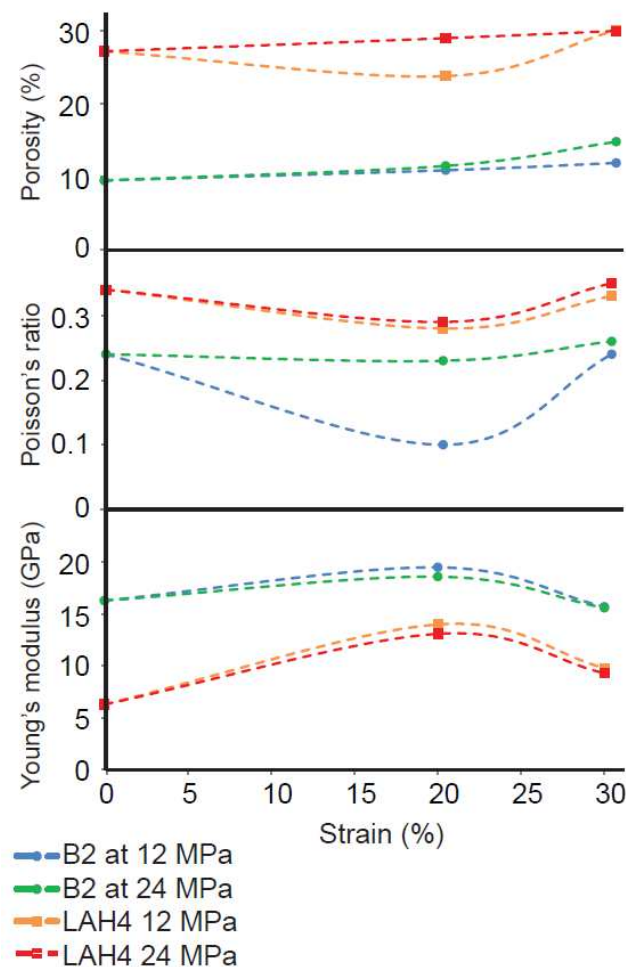
Figure 2-9. Physical properties of the samples: The evolution of porosity, Poisson's ratio and Young's modulus from the starting material to deformed products, points represent measured values and dashed lines infer the evolution.

By increasing strain to 30 % at 12 MPa, the Poisson's ratio increases and Young's modulus decreases, such that both values become comparable to the starting material (Figure 2-9). At 30 % strain, the permeability of the material is reduced for sample B2 (Figure 2-10). However, the sample of LAH4 deformed to 30 % strain was unable to sustain pressure in the permeameter to even 5 MPa effective pressure and ruptured (indicating further weakening compared to the starting material and the sample deformed at 20 % strain). The permeability of LAH4 was however decreased at the lower stress of 2.8 MPa to 20 % strain (Figure 2-10).
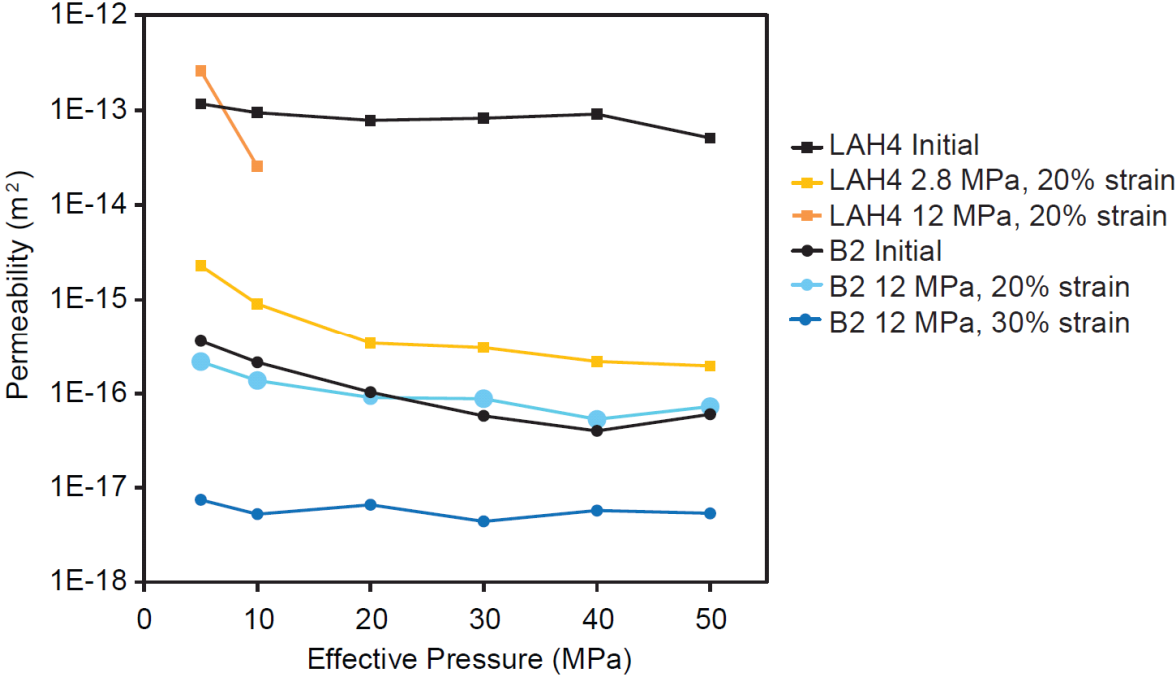
Figure 2-10. Permeability evolution: Steady-state water permeability measured at effective pressures of 5 - 50 MPa for samples B2 and LAH4 (natural and deformed at 2.8 or 12 MPa to a total of 20 or 30 % strain).

Upon increasing stress to 24 MPa and deforming to 20 % strain, Poisson's ratio and Young's modulus also indicate a stiffening of both materials, although in this instance the porosity of LAH4 is now also increased, contrary to 12 MPa. By increasing strain to 30 %, the Young's modulus decreases (for B2, to slightly below the starting material, whereas for LAH4, still considerably above) and Poisson's ratio increases (Figure 2-9). However, even in the most deformed samples, Poisson's ratio and Young's modulus values are similar to the starting material, but there is a complex evolution of strengthening and weakening beforehand. We note that increasing strain has a larger effect on porosity, Young's modulus and Poisson's ratio than increasing stress over the investigated ranges, and that the effect of both stress and total strain

on permeability evolution is significant, with lower stresses and higher strains reducing permeability the most.

2.4. Discussion

The rheological and dynamic evolution of the samples is complex. It may be summarised as follows:

1) Recoverable elastic strain during which no fracturing occurs.

2) Beyond 1 % strain the behaviour of the samples deviates: both sample sets deformed at 2.8 MPa proceed with strain-hardening behaviour to at least 20 % strain, corresponding to a decrease in permeability. At 12 or 24 MPa samples of B2 have a strain hardening portion at the onset of loading (to ~5 % strain). In contrast, despite the sudden drop in strain rate early in the loading, samples of LAH4 does not exhibit strain-hardening at either 12 or 24 MPa (Figure 2-5).

3) For the experiments at 12 or 24 MPa, constant strain rate is achieved after the elastic strain portion for LAH4 and after the strain-hardening for B2 (Figure 2-5a). This stage initiates marginally sooner (lower strain) at higher stresses (and thus strain rate). For both samples the behaviour is shear-thinning (Figure 2-6). Under a uniaxial stress of 12 MPa, both samples achieve 30 % strain without evidence of an approach to brittle failure, although fractures are seen to coalesce in LAH4 (Figure 2-7). Here, permeability remains unchanged at 12 MPa and 20 % strain, but structurally degrades LAH4 (evidenced by sample rupture during permeability measurements). As strain increases permeability is reduced for B2, but sample LAH4 is weakened despite elastic moduli which indicate stiffening for both samples; hence the strain is primarily controlling the reorganisation of the crystals in multi-phase magma.

4) At 24 MPa there is an acceleration in the rate of viscosity decrease for LAH4, which must result from the structural breakdown of the material after 25 % strain. Fractures coalesce and form pervasive damage zones (Figure 2-1, Figure 2-7). This is not seen in the B2 samples.

The rheological behaviour of B2 is in accordance with the rheological relationship depicted in Lavallée et al. (2011) for magmas with solid-fraction crystal contents of at least 50 vol. % (Figure 2-8), but for LAH4 a lower-than-anticipated viscosity results from a structural reorganisation and weakening of the material. Viscosity varies as a function of applied stress,

and deformation is as such, strain rate dependent. For both samples the viscosity was lower at higher applied stress, but under the same applied stress, apparent viscosity was higher in B2 than in LAH4 (Figure 2-5c). Relative viscosity was also higher in B2 than LAH4, which attests to the higher apparent viscosity (Figure 2-5b) and higher interstitial melt viscosity (Figure 2-5d), but is also a result of rapidly increasing damage in LAH4 (Figure 2-1, Figure 2-7). The fact that LAH4 is both less viscous and weaker must relate to the structural attributes of the samples, including crystal content, size and distribution and porosity (including pore size / shape distribution and pore versus crack porosity). Indeed, the Young's moduli of the starting materials (Figure 2-9) verify that LAH4 is less stiff than B2, and the higher Poisson's ratio attests to the higher porosity of LAH4.

Apparent and relative viscosity increased with increasing strain at low stress (2.8 MPa) for both samples, showing strain-hardening behaviour. Additionally the elastic portion at the onset of loading in sample B2 at higher load was strain-hardening. In the higher stress experiments (12-24 MPa) viscosity decayed under constant stress, a phenomenon known as pseudo-plastic behaviour and previously referred to as "time-dependent" deformation (Cordonnier et al., 2009). Over time, this effect was faster at higher stress, and also faster in LAH4 than in B2. However, this difference was negated by comparing diminishing viscosity with strain, for which the rates were comparable for B2 and LAH4 (Figure 2-5b). It becomes more apparent still by comparing relative viscosity changes with strain (Figure 2-5c), that this "time-dependent" deformation of multi-phase suspensions under constant stress is not dependent upon crystal content (under the ranges investigated) or indeed time and instead, is controlled primarily by total strain. The "strain-dependent" deformation must then result partially from magmatic flow and rearrangement of the suspended crystals (as evidenced by thin section and tomography imaging in Figures 2-1 and 2-7) and partially from deformation of the crystals during the unavoidable crystal-crystal interactions which occur when a maximum packing fraction is exceeded, such that particles are forced to interact and transmit stresses (Petford, 2003). The acceleration in the viscosity decrease exhibited by LAH4 at 24 MPa at strain above ~25 % (Figure 2-5b and c), marks the onset of bulk sample failure, as fractures reach the stage of growth and coalescence (Figure 2-1, Figure 2-7).

The evolution of Poisson's ratio and Young's modulus differs between samples, but may be summarised as an initial stiffening of the samples during the strain-hardening period where pre-existing cracks and compliant pores orientated sub-perpendicular to the applied stress are

closed. The subsequent period of visco-elastic deformation comprises further sub-perpendicular pore and crack closure and ductile deformation of the glass and groundmass, which increases the Young's modulus and lowers the Poisson's ratio. The competition between the closure of sub-perpendicular cracks and pores, and the opening of parallel (i.e. orientated axially) cracks inside the crystals, results in a net reduction in porosity (which contributes to the shear-thinning nature of the magma). However, permeability remains unchanged in the samples deformed at 12 MPa to 20 % strain. We contend that, although the net porosity was reduced, the porosity used for fluid flow (i.e. cracks and pores aligned parallel to the flow direction) will remain open (and new cracks orientated parallel to flow are restricted to phenocrysts and do not connect), thus explaining the unchanged permeability. However, the sample of LAH4 deformed at 12 MPa to 20 % strain failed under pressurisation for permeability measurements above at an effective pressure of 20 MPa, an indication of weakening as compared to the starting material.

By further increasing strain to 30 % the Young's modulus in B2 is finally decreased, indicating a reduction in sample stiffness (independent of stress), but the sample deformed at 12 MPa actually has a lower permeability than the starting material. We postulate that this is a result of sample geometry, whereby at the top and bottom of the sample deformed under uniaxial compression there is a densification of the material (see Figure 2-7) between the diagonally-aligned shear zones. Despite presumably elevated permeability along the shear zones and in the central portion, the permeability in the axial direction is controlled by the least permeable layer. From thin section analysis we find that fractures initiate in phenocrysts, which are weaker than surrounding melt (Cordonnier et al., 2009) and during inevitable crystal-crystal interaction, and that these fractures tend to propagate along the axis of principal stress in both sample sets (i.e. vertically in Figure 2-1) to eventually form diagonal damage zones seen in Figure 2-7. For LAH4 the sample deformed at 12 MPa to 20 % strain failed under an effective pressure of 20 MPa during the permeability measurements, which must have forced coalescence of adjacent fractures seen in Figures 2-1 and 2-7. Rheological data supports the physical observations; constant-rate, shear-thinning deformation persists for B2 until at least 30 % strain, however in LAH4 it gives way to the onset of mechanical degradation above ~25 % strain. Bulk sample failure ensues, evidenced by a rapid increase in strain rate under constant stress. The sample deformed to 30 % was weakened so substantially that it was unable to sustain any pressurisation for permeability measurements, despite the fact that the dynamic elastic moduli indicate stiffening. Alternative measurements made on the sample deformed at 2.8 MPa show a

significant decrease in permeability, a result of on-going strain-hardening behaviour (Figure 2-5b and c).

The damage accumulation in the originally-isotropic samples is highly anisotropic (pre-existing cracks and compliant pores orientated sub-perpendicular to the applied stress will close, and new cracks will form parallel to the applied stress). As a result, our ultrasonic wave velocities and dynamic elastic moduli (measured in the axial direction) will contain some bias. Therefore, we consider that our values represent a "minimum" in the evolution of elastic properties of deforming magma. We must also note that, since the deformation at a volcano could be considered to evolve quasi-statically, rather than dynamically, it has been suggested that static elastic moduli are more appropriate for the modelling of volcanic hazards (Heap et al. 2009; Manconi et al. 2010).

2.5. Volcanological Significance

Understanding the behaviour of multi-phase magmatic suspensions under realistic volcanic conditions is vital to predicting volcanic activity. However, the processes which control the common transition from effusive to explosive eruption style remain poorly understood. The results of the experiments reported in this study, in conjunction with analysis of the physical properties measured allow us to examine the transition in deformation style in detail, which will help to improve models of volcanic unrest (Caricchi et al., 2007; Costa et al., 2009; Deubelbeiss et al., 2011; Lavallée et al., 2007; Melnik, 2001; Melnik and Sparks, 1999). We find that highly crystalline magmas exhibit significantly higher viscosities when deformed more slowly. An order of magnitude change in stress, manifested as 2 orders of magnitude change in strain rate, changes the viscosity by 1-2 log units, providing evidence of shear-thinning behaviour. Such changes, experienced over the timescale of volcanic unrest, could result in the transition from effusive to explosive behaviour such as that experienced frequently at Volcán de Colima (Breton et al., 2002; Luhr and Carmichael, 1990). Indeed rheological variations have frequently been cited as the cause of effusive to explosive transitions (Cordonnier et al., 2009; D'Oriano et al., 2005; Dingwell, 1996; Divoux et al., 2011; Lavallée et al., 2008). By increasing the viscosity of magma, especially when simultaneously decreasing the permeability, the potential for explosivity is drastically increased: an increase in shear stress or strain rate could shift magma into the brittle regime (Lavallée et al., 2008) and result in fragmentation. Deformation of magmas can result in a rearrangement of porosity, from void spaces and fractures distributed

evenly throughout the sample, to preferred orientations and coalescence into damage zones. Permeable zones form preferentially where strain is localised, affecting the ability of volcanoes to effectively degas through the permeable porous network. Hence, highly viscous, low permeability magmas carry the potential to block volcanic conduits with a magma plug, resulting in the build-up of pressures in the conduit. Plug formation may lead to repetitive "drumbeat" seismicity (Iverson, 2005; Lensky et al., 2008), spine extrusion (Nakada et al., 1999; Sparks and Young, 2002; Vallance et al., 2008) and eventual explosive eruption. Here, we demonstrate that the apparent viscosity of multi-phase magmas is not only dependent on the melt viscosity and crystal and pore contents, but is also dependent upon the strength of the sample; mechanical degradation of a material can result in lower apparent viscosities than anticipated, especially at high strain rates, but this is because failure of the sample has already occurred. In a lava dome setting this is manifested as dome collapse (which may not be predicted if the material properties are not understood), which can initiate catastrophic explosive eruptions due to unloading and depressurisation (Edmonds and Herd, 2007; Melnik and Sparks, 2005) and is a significant risk at Volcán de Colima and other stratovolcanoes.

2.6. Conclusions

This study shows that, at a given temperature and stress, chemically similar lava types can display a significant range of measured strain rates as a result of crystallinity and porosity, which emphasises the need to quantify the influence of these characteristics. Higher stresses result in lower apparent viscosities for multi-phase melt suspensions, and viscosity is strain rate dependent. Relative viscosity decreases as a function of strain, independent of crystal fraction under the range investigated, thus the previously termed "time-dependent" deformation should more properly be called "strain-dependent" deformation. With increasing strain, crystalline magmas follow a complex evolution of: elastic; strain hardening; constant-rate, and finally strain weakening behaviour in the approach to bulk failure. The strain at which these stages occur is dependent upon crystallinity, and other physical attributes (porosity and crystal size and shape distribution) which also significantly influence the mechanical characteristics. Strain-hardening results from the closure of pores, evidenced by porosity and permeability evolution while the constant-rate period is characterised by crystal rearrangement and magmatic flow and initiation of fractures in phenocrysts and groundmass. After a certain threshold (of strain, dependent upon stress) fracture coalescence and damage zone development begins to control the apparent viscosity, and behaviour deviates from that of magmatic flow. Although physical

evidence shows that the samples experience significant damage, the axially-measured dynamic elastic moduli do not change significantly (due to the significant anisotropy developing in the deformed samples), and thus do not represent the true characteristics of the samples. We recommend that extreme care should be taken when using ultrasonic wave velocities as a proxy for strain (or damage).

χρυσὸν γὰρ οἱ διζήμενοι γῆν πολλὴν ὀρύσσουσι καὶ εὑρίσκουσιν ὀλίγον.
“The seekers of gold burrow through much earth and find little”

-Clement: Stromateis IV. 4.

Chapter 3

Crystal plasticity as a strain marker of the viscous-brittle transition in magmas

Quantifying magma transport requires rheological models. Models of suspension rheology have long attempted to deal with crystal fraction, shape and aspect ratio as rheological variables. Recent advances in experimental magma deformation and imaging now provide a substantial opportunity for completing our picture of the viscous behaviour of multi-phase systems.

This study reports the first observation of crystal plasticity, identified using electron backscatter diffraction (EBSD), in the phenocrysts and microlites of two natural andesitic magmas that have been deformed experimentally at magmatic temperatures. The deformation yields a plastic response of the crystalline fraction, observable as a lattice misorientation, which grows with increasing stress and strain. Misorientations are less pronounced in pyroxene than in plagioclase (which is both less coherent and strongly anisometric). Phenocrysts which contain brittle fractures show crystal-plastic deformation in the intact segments. Apparently, crystal plasticity plays a significant role in strain accommodation under volcanic conditions. Thus the viscous-brittle transition during magma ascent may incorporate a regime of crystal-plastic deformation, the remains of which may be used as a strain marker. With higher crystal fraction, and a correspondingly larger proportion of strain accommodated in the crystal fraction, internal misorientations are larger. A phenomenon that will favour strain localisation, shear zone formation and plug flow.

3.1. Introduction

Understanding the behaviour of magma at volcanic temperatures and pressures is fundamental to the inference of volcanic hazards. Although many advances in the fields of magma rheology and rock mechanics signal increasingly common goals, one area of mutual interest, that of the role of crystal plasticity in magmas, has been overlooked. This paper documents the first study of crystal-plastic deformation in magma using electron backscatter diffraction (EBSD), an innovative technique which can measure misorientations of the crystal lattice, a physical manifestation of strain accommodation.

3.2. Rheological Background

Silicate liquid may be classified as a Maxwell visco-elastic fluid (Webb and Dingwell, 1990) which acts as a Newtonian liquid at low strain rates, transitioning to a non-Newtonian behaviour as deformation approaches the timescale of structural relaxation. The exsolution of gas bubbles (e.g. Lejeune et al (1999) and Manga et al. (1998)), as well as the nucleation of crystals, provide further complexities in the rheological behaviour of magma (see Petford et al. (2009) for a review). Studies using analogues (Cimarelli et al., 2011; Mueller et al., 2011), synthesised materials (Caricchi et al., 2007; Picard et al., 2011) and natural, partially crystalline melts (Caricchi et al., 2007; Cordonnier et al., 2009) indicate that once a critical packing fraction is exceeded, crystals interact (Picard et al., 2011), which facilitates strain-partitioning and shear thinning. In ascending dome lavas, the shear-thinning rheology favours formation of discrete shear zones and, as strain localises along conduit margins, plug flow allows the bulk of the magma to ascend relatively undeformed (Lavallée et al., 2013).

Until now, the effect of plastically deformable particles on magma rheology has been overlooked. Crystal-plastic deformation occurs when the critical resolved shear stress (CRSS) on favourably oriented lattice planes is exceeded (Poirier, 1995), resulting in an irreversible, permanent strain (accommodated by "misorientation" of the crystal lattice). In magma, strain could be accommodated, in part, by plastic deformation of the phenocrysts, instead of wholly partitioned as viscous strain in the melt between a network of rigid suspended particles. Although crystal plasticity has been cited as a contributing factor to the non-Newtonian behaviour of magma (Deubelbeiss et al., 2011), it is a phrase which is commonly misused in magma rheology. No evidence of the role of crystal plasticity has ever been observed in natural

or experimentally deformed magmas. Here we present the first direct evidence of atomic lattice re-arrangement in experimentally deformed magmatic phenocrysts.

3.3. Methodology

3.3.1. Magma Deformation

Two types of natural andesitic lava from Volcán de Colima (Mexico) were chosen for this study, the lavas have a crystal assemblage of plagioclase and ortho- and clino-pyroxene set in silicic, rhyolitic glass with significantly different porosities and crystal contents (Table 3-1).
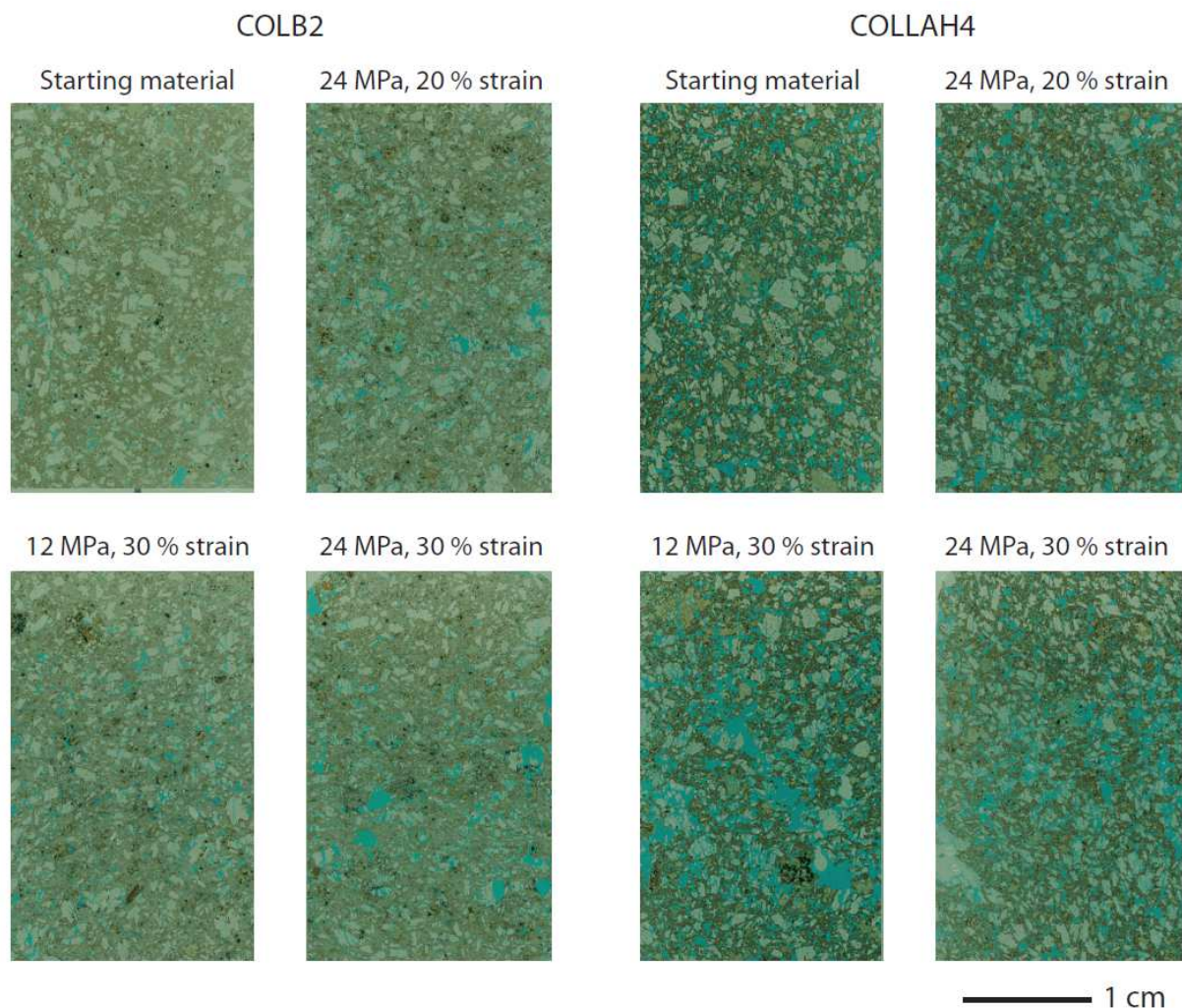
Figure 3-1. *Thin section scans from the starting materials COLB2 and COLLAH4 and from the central portion (across the diameter, parallel to the length) of the six experimentally deformed cores. Images give an overview of the distribution of cracking throughout the samples when the principal stress is applied in the vertical direction, thus individual fractures are predominantly parallel to applied stress in both COLB2 and COLLAH4. An increasing*

amount of damage with increasing stress and /or strain is evident in both samples. At low stresses / strains fractures are largely restricted to phenocrysts, whereas at higher stresses / strains fractures propagate through the groundmass as well and fractures coalesce to form pervasive fractures and damage zones, which form at approximately 45º to applied load. The central portion is used for this study, where the deformation is not influenced by edge-effects or friction from contact with the apparatus at the top and bottom.

Cylindrical cores of the magma were deformed at 945 $^{\circ}$C under a constant uniaxial load of 12 or 24 MPa to a total strain of 20 or 30 % (see Hess et al. (2007) for apparatus setup and procedure) to finally provide eight sample sets with different shear stress and strain histories. Thin sections made across the diameter, parallel to the length of the six deformed cores show that, internally, fractures nucleate in crystals and propagate into the groundmass (Figure 3-1). The higher stress and / or strain experiments result in visibly increased amounts of deformation, in hand specimen exemplified by lateral bulging, and pervasive extensional fractures. A ~1 cm^2 area from each of the thin sections of the deformed samples and starting materials was then analysed using electron backscatter diffraction (EBSD).

Table 3-1. Physical attributes and chemical composition of the starting materials.

Rock type	Physical attributes (%)			
	Pores	Glass	Pheno-crysts	Micro-lites
COL B2	9.2	36.3	31.8	18.2
COL LAH4	27.5	28.6	25.0	14.3

Rock type	Chemical composition (Weight %)											
	SiO$_2$	Al$_2$O$_3$	Fe$_2$O$_3$	MnO	MgO	CaO	Na$_2$O	K$_2$O	TiO$_2$	P$_2$O$_5$	PF	Total
COL B2	60.59	17.85	5.69	0.10	2.81	5.78	4.73	1.34	0.59	0.20	0.32	100
COL LAH4	59.12	17.46	6.14	0.11	4.04	6.62	4.52	1.19	0.62	0.19	0.00	100

3.3.2. Electron Backscatter Diffraction

Crystal lattice orientation mapping was conducted in a Phillips XL 30 SEM using the acquisition software HKL CHANNEL 5 by Oxford instruments at 8 nA and 20 KeV, and

minerals were indexed in Flamenco using 7 bands, 70 reflectors, 120 Hough resolution, band edges and 3*3 binning, appropriate for indexing plagioclase and ortho- and clino-pyroxenes. Using the map manipulating program, Tango, in the same software, individual crystals in the EBSD maps were subjected to textural analysis, where each pixel (one EBSD data point) is colour coded according to the degree of misorientation of the crystal lattice relative to a previously selected pixel. Misorientations were also plotted as profiles to give a more quantitative description of the deformation experienced by the crystals, and this data was correlated for each sample set to provide a normalised misorientation angle per unit length for several hundred phenocrysts and microlites. The measured crystal lattice misorientations are considered to be a minimum value, as it is unlikely that the principal strain axis of the crystal lies along the plane of the thin section surface.

3.4. Development of Crystal plasticity

These samples exhibit crystal plasticity. Misorientations of the crystal lattice, with respect to a chosen reference point within individual crystals, are seen in all experimental samples for phenocrysts and microlites from both plagioclase and pyroxene (Figure 3-2), using misorientation profiles obtained from EBSD (see Data Repository for detail on the analysis). The amount of crystal lattice misorientation within a given sample is significantly higher in microlites than in phenocrysts (Figure 2-2, Figure 2-3), which may be attributed to its anisometric morphology with a mean aspect ratio of 2:1 for phenocrysts and 6:1 for microlites. Misorientation is also higher in plagioclase than in the pyroxenes (aspect ratio 1:1), which has a higher competence (Fletcher et al., 1997).

An increase of either strain or stress increased the amount of misorientation of the crystal lattice for both phenocrysts and microlites and also resulted in a concordant mean grain size reduction for the whole sample set (Figure 2-3). Over the range investigated, increasing stress (from 12 to 24 MPa) has a more pronounced effect on lattice misorientation than increasing strain (from 20 to 30 %).

COLB2

Starting material

24 MPa
20 % strain

12 MPa
30 % strain

24 MPa
30 % strain

COLLAH4

Starting material

24 MPa
20 % strain

12 MPa
30 % strain

24 MPa
30 % strain

Misorientation (°)

Distance (μm)
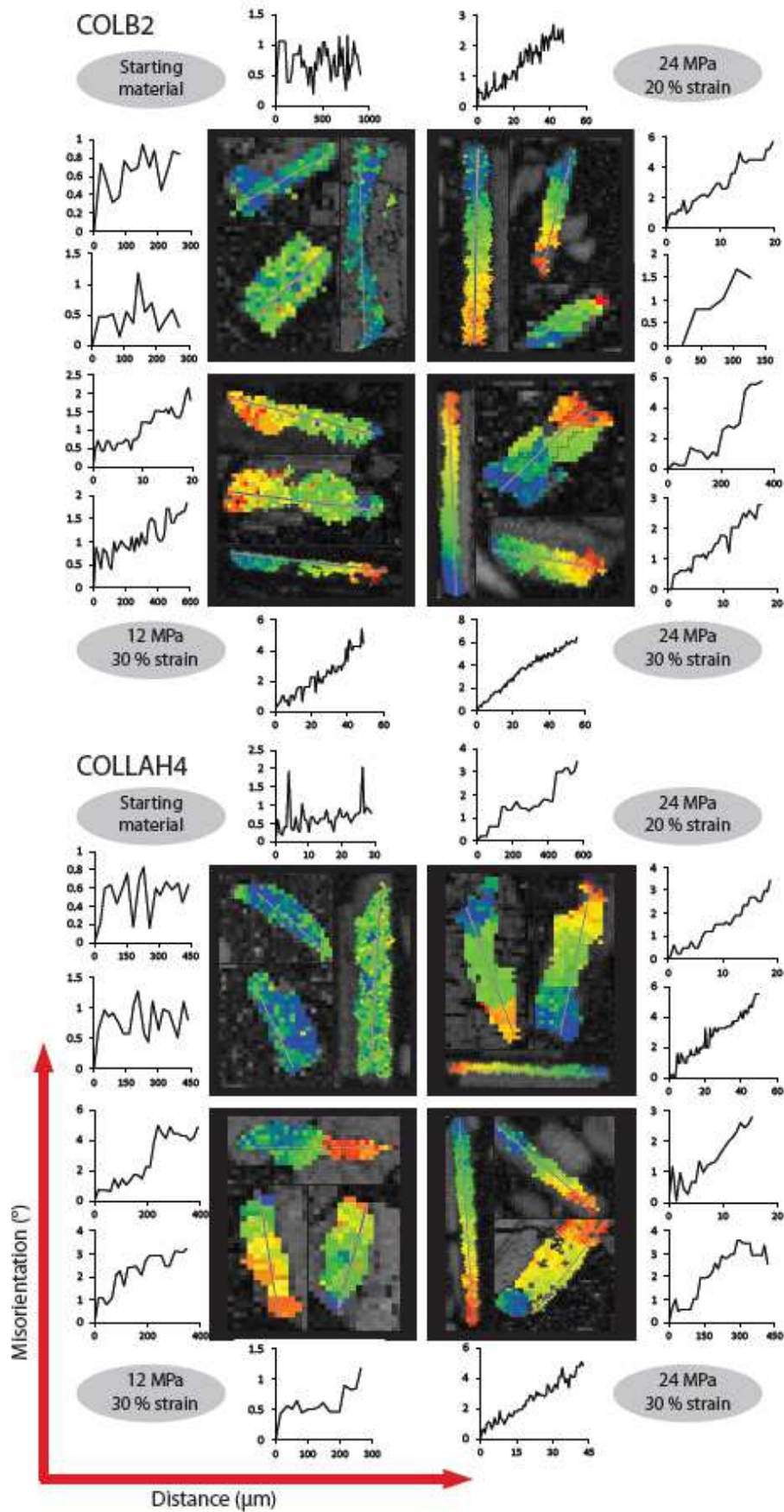
Figure 3-2. Crystallographic misorientation induced by magma deformation. A composite image of 3 phenocrysts or microlites from the two starting materials and each of the

experimental products. Each crystal is colour coded according to misorientation of the crystal lattice from a given reference point at one end of the crystal. Corresponding misorientation profiles run from blue to red on the crystal, and indicate the length and misorientation scales. Profiles highlight small, unsystematic misorientations in the starting materials and systematic lattice distortion in the experimentally deformed crystals.
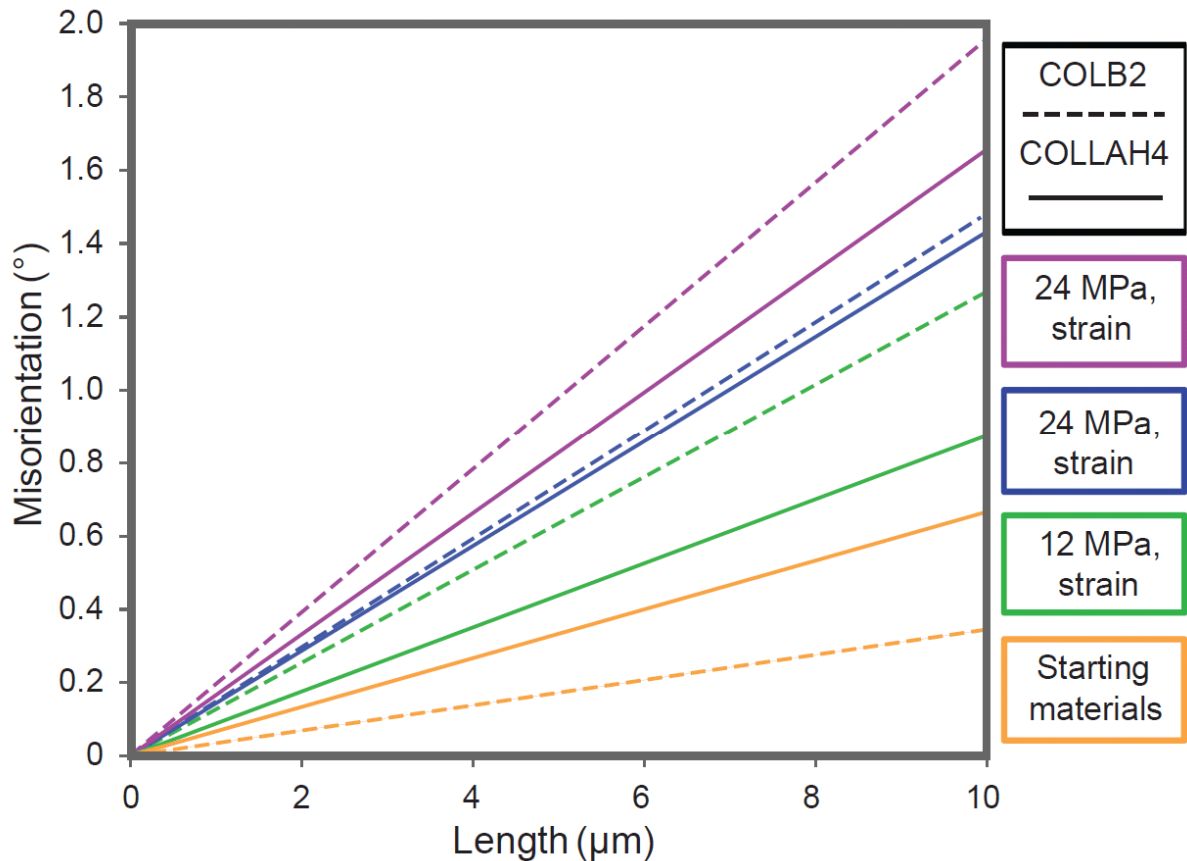
Figure 3-3. Quantified lattice misorientation in microlites. Normalised gradient of misorientation angle over a 10 μm length of microlites from the starting material (orange, COLB2 in dashed lines and COLLAH4 in solid), each set of experimental parameters (green, blue, purple), gradient is calculated by measuring the misorientation and length of >300 microlites of <50 μm and an intercept at 0°/0 μm. The graph indicates the increasing effect of stress and/or strain on misorientation, applicable to both samples.

Background levels of misorientation in the crystals of the starting materials (Figure 3-3, Figure 3-4) are accounted for by unsystematic (also <2°) variations in lattice misorientation (Figure 3-2), in stark contrast to the systematic misorientation profiles of the phenocrysts and microlites from the deformed samples (Figure 3-2). Under each set of experimental conditions

misorientations in phenocrysts and microlites alike are higher in sample COLB2 (Figure 3-3, Figure 3-4), which has a higher crystal fraction (Table 3-1).
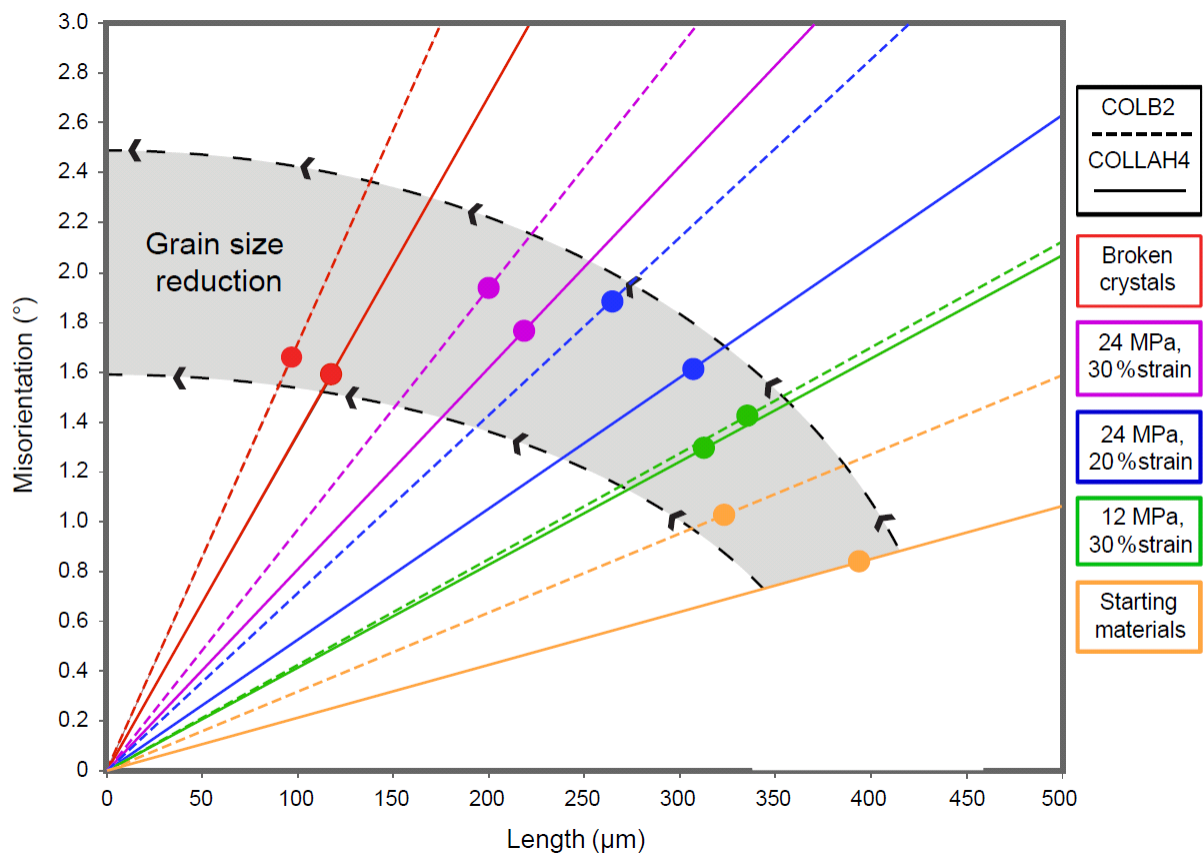
Figure 3-4. Quantified lattice misorientation in Phenocrysts and experimentally driven grain size reduction. Normalised gradient of misorientation for starting material and each set of experimental parameters (green, blue, purple) and phenocrysts with brittle fractures (red, only the contribution of the plastic misorientations were considered in these data) for both COLB2 (dashed) and COLLAH4 (solid) with trends extending to an intercept at 0º/0 µm, and based on >600 measurements of crystals >50 µm. The point marks the average grain size for the whole sample, measured from thin section images and plotted at the line intercept to indicate expected misorientation at that grain size. The plot highlights the increasing misorientation, and decreasing grain size with higher stress and/or strain conditions, the higher misorientations in the denser COLB2, and the higher misorientation of the plastic portion for crystals which contain brittle fractures.

There is an overall grain size reduction imparted by the experiments (Figure 3-4) due to brittle fracture of the crystals (see Figure 3-5). While the degree of misorientation across the fracture has no plastic significance, it may be the case that these fractures resulted from plastic

deformation that exceeded the plastic limit of the crystals. This is identified by a sweeping, gradual misorientation in the intact portions of the phenocrysts (blue in the plots in Figure 3-5), punctuated by an abrupt fracture (pink in the plots in Figure 3-5). For all experimental conditions, all of the phenocrysts which underwent brittle fractures had crystal lattice misorientation values (taking the plastic contribution only) which lay above all of the lines of mean misorientation angle per unit length (Figure 3-4), which may providing a threshold for maximum lattice misorientation, or a plastic limit (Poirier, 1985), if the plastic deformation occurred prior to fracture.
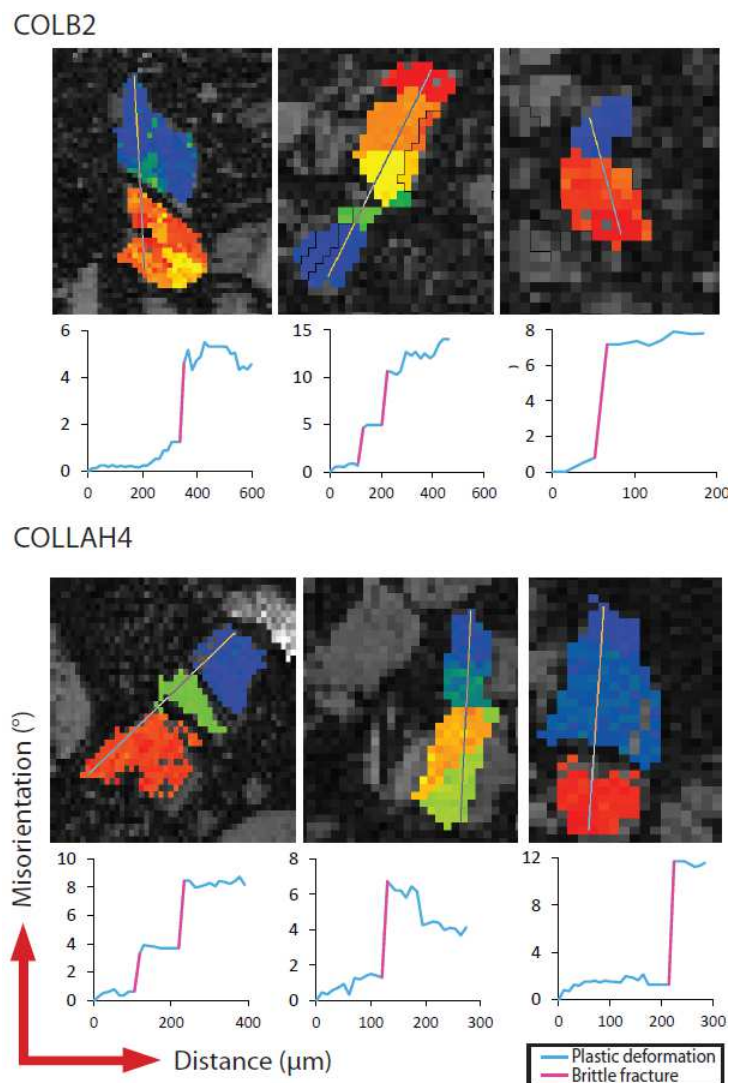
Figure 3-5. Brittle fractures in phenocrysts. Examples in which the phenocryst has undergone one or more brittle fractures. Phenocrysts (colour-coded), and are from COLB2 and COLLAH4 samples deformed at 24 MPa to 30 % total strain. Misorientation profiles begin at the blue end of the crystals, show the length and misorientation scale, and highlight transitions from plastic (blue) to brittle (pink) behaviour.

3.5. Discussion and implications

Using two different partially crystalline magmatic suspensions with limited initial crystal plasticity, and inducing variable amounts of strain at different applied stresses we find that crystal plastic deformation of plagioclase, diopside and hypersthene is attainable under magmatic conditions. Crystal-plastic deformation may serve as an important outlet for strain. Crystal plasticity may be viewed as the mechanism that accommodates some of the permanent, inelastic deformation imparted on magma that does not reside in the indefinitely deformable liquid phase.
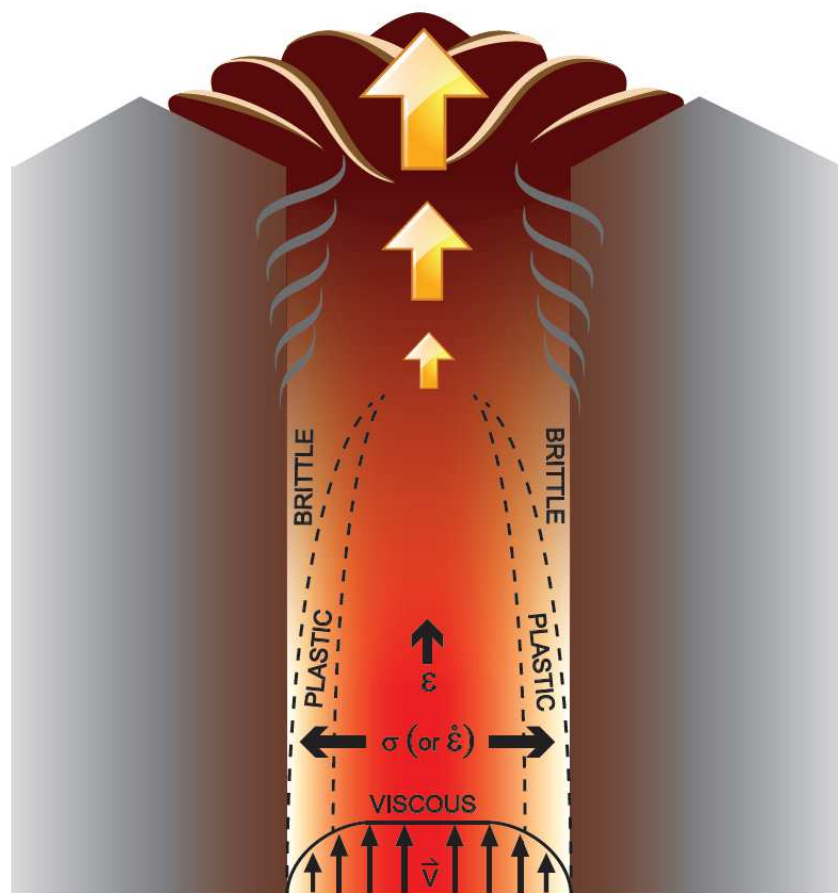
Figure 3-6. Deformation mechanisms in the conduit. Sketch of conduit processes and the locus of deformation mechanisms in ascending magma, transitioning from viscous to crystal-plastic to brittle deformation with increasing stress (proportional to increasing strain rate ($\mathring{\varepsilon}$)) toward the conduit wall or total strain (ε) during ascent.

Crystal plasticity may also be the precursor mechanism to a transition from viscous to brittle processes, and therefore bears significance in the deformation history of magma and can act as a strain marker. The amount of strain experienced by each crystal is higher in microlites than

in phenocrysts, suggesting that aspect ratio plays a key role. Misorientations are also higher in plagioclase than pyroxene crystals, which may be due to aspect ratio or the relative strengths of the minerals. The susceptibility of plagioclase to crystal plasticity is of particular relevance to the study of silicic volcanoes, where the mineralogy is frequently dominated by this phase.

During ascent of crystalline magma, the non-Newtonian rheology is controlled not only by the porosity and crystallinity, the packing fraction and the size, shape and dispersal of crystals, but also by the deformability of the suspended particles themselves. This necessarily complicates the viscous-brittle transition envisaged during magma ascent (Cordonnier et al., 2012; Dingwell, 1997), providing a time-space interval during which strain may be accommodated by crystal plastic deformation (Figure 3-6). The locus of this crystal-plastic interval is dependent upon total strain (~ ascent), total shear stress (which increases towards the margins of the conduit) and crystallinity (itself dependent upon composition and temperature). As deformation increases, the plastic limit of the suspended crystals may be exceeded, demonstrating the ability of plastic deformation to lead bulk ductile deformation toward brittle failure. In regimes where strain can be localised, specifically at conduit margins, crystal-plastic deformation is locked into the magma and may precede magma fracture. This aids the process of strain localisation, favours plug flow and is surely fundamental to a variety of magmatic and volcanic scenarios. With integration into rheological models, crystal-plastic deformation may well become a valuable strain marker that characterises magma ascent and lava dome eruption dynamics.

“Iteration, like friction, is likely to generate heat instead of progress.”

- George Eliot

Chapter 4

Extreme frictional processes in the volcanic conduit of Mount St. Helens (USA)

during the 2004-2008 eruption

The 2004-2008 eruption of Mount St. Helens saw the extrusion of seven high-viscosity spines and formation of discrete shear zones along the conduit margin. At spine 7 this shear zone consists of four structurally distinct layers: the outer surface gouge (L1) crosscuts; a dark, banded layer (L2) which grades into; a moderately sheared layer (L3) and; undeformed rock (L4) inside the spine. Field observations, porosity measurements, geochemistry, mineralogy, microstructure, crystal size- and shape-distribution, kinetic properties and magnetic analyses chart the evolution of deformation processes and products throughout the eruption.

Gouge formation was concomitant with characteristic microseismic "drumbeats" at depths 0.5-1 km. In addition, the seismic record shows two larger earthquakes with similar seismic signatures in August 2006, which we conclude represent larger slip amounts along the conduit margin of spine 7. Extensive slip resulted in frictional heating on the order of several hundreds of degrees, melting the highly-viscous, crystalline, ascending magma plug and forming a pseudotachylyte. High ambient temperatures in the conduit resulted in near-equilibrium melting and slow recrystallisation, thus impeding the development of signature pseudotachylyte characteristics and hindering identification. Thus, frictional melting and recrystallisation in ascending magma plugs may be a common, but unidentified, phenomena at composite volcanoes worldwide.

4.1. Introduction

4.1.1. Frictional Processes

During volcanic eruptions, the extrusion of high-temperature, high-viscosity magmatic plugs imposes frictional contact against conduit margins in a manner analogous to seismogenic faults. The near-solidus-temperature of extruding spines at Mount St Helens (USA) during the 2004-2008 eruption means extrusion was controlled by structural rather than magmatic processes (Vallance et al., 2008). The dynamics of seismogenic faulting is currently a highly active area of research in theoretical (Smith and Kilburn, 2010; Smith et al., 2007), experimental (Benson et al., 2008; Benson et al., 2010; Lavallée et al., 2008; Smith et al., 2009) and structural (Tuffen and Dingwell, 2005; Tuffen et al., 2003) volcanology.

Variation of differential stress, such that the Coulomb criterion for shear failure is exceeded, initiates ruptures in rocks on a laboratory to tectonic scale. Fault products depend upon slip rates and the friction coefficient of the ruptured material (Paterson and Wong, 2005; Scholz, 2002) and are governed by the tectonic setting and P-T conditions following the classification of Sibson (1977).

Within volcanic systems, background temperatures are significantly higher than the geotherm permits in other upper-crustal locations, whereas confining pressures are much lower than in high-temperature, lower-crustal settings: thus via their exceptional ambient P-T conditions, volcanic systems represent unique environments for faulting. Here, we assess the deformation mechanisms that took place during the extrusion of spine 7 at Mount St. Helens and discuss the potential for frictional melting along volcanic conduit margins.

4.1.2. Mount St. Helens background

Mount St. Helens (MSH) is the most active member of the Cascade Volcanic Arc, which stretches along the West coast of North America from British Columbia (Canada) through to Northern California (USA). September 2004 marked the onset of the most recent eruption, indicated by localised ground uplift and shallow seismicity, followed swiftly by small gas-driven explosions (Scott et al., 2008). Subsequent extrusion of a lava dome as a solid plug began on October 11th. The growth continued until January 2008, forming a series of seven spines

(Thornber et al., 2008). The spine margins were covered by a ~1-3 m thick, continuous layer of gouge with multiple planes of slickensides (Cashman et al., 2008; Kennedy et al., 2009) and was interpreted as an important control on ascent and extrusion.

The spines initially extruded at rates of 5.9 m^3s^{-1}, and slowed to 0.7 m^3s^{-1} later in the eruption (Schilling et al., 2008). The early spines extended directly south, with spines 3-5 (October 2004-July 2005) showing a whale-back morphology (Scott et al. 2008). The vent remained in an almost constant position during the early extrusion of the spines (Scott et al., 2008), but during later stages (Autumn 2005 onwards), spine 7 took on a dome-like morphology which spread to the West of the previous spines (Vallance et al., 2008). [For the temporal evolution of the dome growth see Vallance et al (2008) and Herriott et al (2008).]

Extrusion of the spines was accompanied by repetitive or "drumbeat" seismicity (Iverson et al., 2006; Matoza and Chouet, 2010). "Drumbeats" were long period (LP) or hybrid, M 0.5-1.5 events, generally located at <1 km depth (Thelen et al., 2008) and occurred at intervals of 40-80 s, based on daily averaged values (Moran et al., 2008). The seismic signature of dome extrusion at MSH has been described as fundamental to the distinction of source mechanisms and thus the underlying mechanical processes. Two sources of the "drumbeat" seismicity have been postulated, and there is evidence for each. Iverson et al. (2006) first proposed that stick-slip motion, an inevitable consequence of rate-weakening frictional slip (Moore et al., 2008) occurred along the surface of the spines, citing evidence in the form of fault gouge, slickensides and cataclasite. This linked the micro-seismicity to ~5 mm slip events along the conduit margin. Waite et al. (2008) analysed the waveform of the LP events and identified dilatational first motions, which indicate a net volume decrease of the source. Thus it was concluded that the "drumbeats" were more likely formed by resonance in a gas-filled horizontally aligned crack or chamber at ~1 km depth in the conduit (Matoza and Chouet, 2010). These apparently conflicting models represent end-member possibilities, whereas the cause of the "drumbeats" was likely a combination of such factors created by the complexity of the volcanic system. Indeed Neuberg et al. (2006) indicated that resonance in a crack or chamber may in fact be initiated by stick-slip events. Irrespective of the cause of the "drumbeats", their production was contemporaneous with the formation of gouge and other fault-like features noted along the spine margins (Kennedy and Russell, 2011; Kennedy et al., 2009).

Larger, impulsive or emergent seismic events (M 2.0-3.6) also occurred sporadically throughout the 2004-2008 eruption, and were generally LP or hybrid, many having negative first arrivals, similar to, but larger than, the "drumbeats". Both frequency and source depth of these events were also akin to the "drumbeats", though radial locations have a smaller spread of only 1 km^2, which could be a result of the increased accuracy derived from larger signals. These similarities indicate that if the source mechanism of the "drumbeats" is stick-slip, then these larger events could represent a larger slip amount on the same slip surface (Iverson et al., 2006), thus magnitude varies as a function of slip and seismicity is produced by lurching of the spine like the upward thrusting of a piston (Moran et al., 2008). Few volcano-tectonic (VT) earthquakes occurred during the eruption, with the exception of the very earliest onset of seismicity in September 2004 and a nine day interval at the end of December 2005 and start of January 2006 when 70 earthquakes occurred at <0.3 km. When events were recorded, they were generally of low magnitude (M <1.0) and shallow depth (<2 km). Moran et al. (2008) infer that the VT events correspond to brittle processes in the underlying rocks of the crater floor perhaps in a manner similar to hydraulic fracturing of the conduit wall (Chadwick et al., 1983). The failure induced in the conduit wall material would result in a static stress-drop, temporarily promoting movement along the conduit margin, thus altering the shallow frictional conditions of the extruding spines.

The holocrystalline, low-porosity nature of the dacite involved has led to the inference that crystallisation occurred as a result of devolatilisation at depths of approximately 1 km (Cashman et al., 2008). Petrographic analysis of the dome lava reveals a microlite-rich, glass- and gas-poor, porphyritic dacite (Pallister et al., 2008), which together with thermal infrared imagery (Snieder et al., 2006) indicates extrusion at temperatures below the rock's solidus, approximated to be 840-880 °C (Rutherford, 2008). Direct measurements by thermal imaging recorded temperatures of up to 600 °C at the surface (Scott et al., 2008), with gashes in the spines revealing internal temperatures of up to 730 °C (Vallance et al., 2008). Interstitial glass is present only in the dome rocks erupted during the first few months, then rapidly falls from >30 % to <2 % (Pallister et al., 2008). This may be accounted for by conduit residence time, during which the bulk of the dacitic magma had sufficient time to crystallise before reaching a depth of 1 km (Moran et al., 2008; Thelen et al., 2008), while the earliest magma was quenched faster as it pushed its way through the cool host rock and 150 m thick Crater Glacier (Vallance et al., 2010). Slowing of extrusion rate throughout the eruptive phase was contemporaneous

with an increase in density (decrease in porosity), crystallinity and strength of the rocks (Smith et al., 2011).

Cashman et al. (2008) have characterised the spine surfaces early in the eruption through January 2006 and have documented variations between gouge, cataclasite and ultracataclasite. This gouge has been recreated experimentally by Kennedy et al. (2009). Experiments were performed at room temperature as it was considered that the time-scales in nature were too short for post-faulting modification or fault healing (Chester, 1994) which might result in increased frictional strength of a fault zone (Di Toro et al., 2006; Mizoguchi et al., 2006). Kennedy et al (2009) established that fault products formed as a result of brittle deformation at the fault margin, with no indication of later annealing and no microstructural evidence for high-temperature, solid-state crystal plasticity in the natural gouge samples (Cashman et al., 2008; Kennedy et al., 2009). Their work constrains deformation to post-crystallisation at a depth of less than 1 km. It is estimated that the fault products formed along 0.8-5 mm thick, sub-parallel, gouge-filled slip surfaces with strike lengths (*i.e.*, conduit circumference) of 98-190 m and displacements of ~5 mm as well as strain rates of approximately $5 \times 10^{-2}\,\mathrm{s^{-1}}$ to $5 \times 10^{-1}\,\mathrm{s^{-1}}$ (Kennedy et al., 2009). This could accommodate extrusions of up to 6 m per day contemporaneous with the microseismic "drumbeats".

During a field survey of the spines in August 2010, we identified a narrow zone of high-strain-rate structures on the extrusion margin of spine 7, which had not been observed on the previous spines. Here, we present a thorough characterization of this structural zone to assess the temporal variability in erupted products and the conditions that may be sustained in volcanic conduits.

4.2. Methods and Results

Mechanical and rheological properties are established through physical analyses (porosity and density), chemical analyses [X-ray fluorescence (XRF), X-ray diffraction (XRD) and wavelength dispersive electron microprobe analysis (WDA)], micro-structural imaging [scanning electron microscopy (SEM)], rheological measurements [differential scanning calorimetry (DSC)], rock-magnetic tests (domain state analysis, natural remanent magnetisation, magnetic susceptibility, Curie temperatures) and grain characterisation (morphology and size distribution). Together the analytical data provide a comprehensive

overview of the transect from the outer layer of gouge through to the undeformed bulk rock in the spine centre, integral to understanding the developing eruption dynamics illustrated schematically in Figure 4-1.
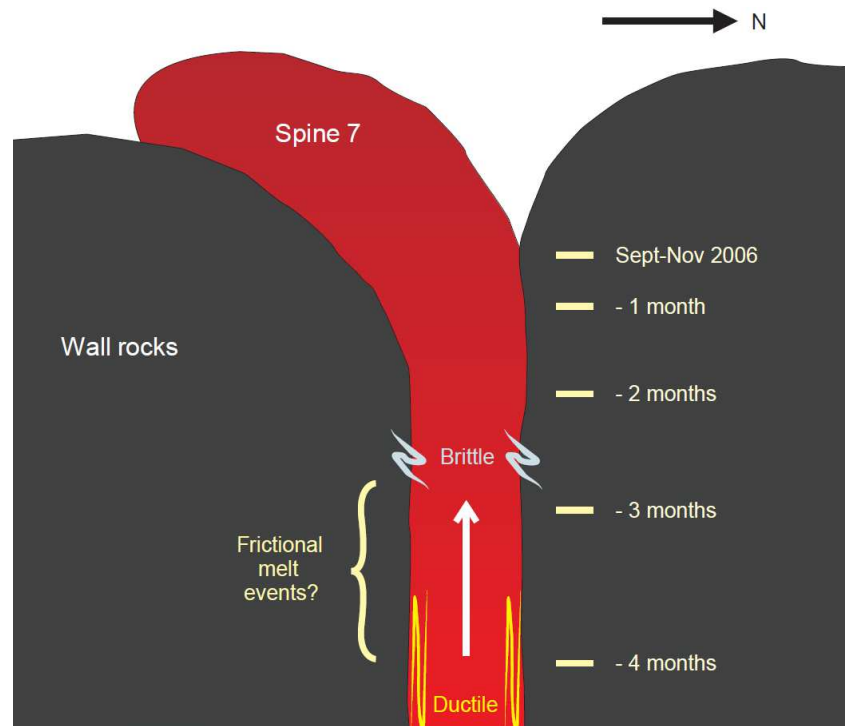
Figure 4-1. Schematic representation of the extruding spine 7 during the 2004-2008 eruption. Progressive slowing of extrusion rate is indicated by the depth-with-time scale adjacent to the conduit, highlighting the position of the sampled area in the months prior to surfacing.

4.2.1. Field observations

The samples were collected in August 2010 from an intact surface portion at the southern end of the eastern side of Spine 7, striking N259° (clockwise from north) and dipping at 47° towards the south-east. Analysis of time-lapse videos (available at http://vulcan.wr.usgs.gov/Volcanoes/MSH/Images/MSH04/movies_and_animations.html) constrained extrusion dates to September-November 2006. The gouge layer in this locality is much thinner than values of 1-3 m documented earlier in the eruption (Cashman et al., 2008). Samples from the outer ~20 cm of Spine 7 were split into four structurally distinct sets (Figure 4-2, Table 4-1) distinguishable by eye. These represent a quasi-continuous gradation from the fault surface through to seemingly undeformed rock inside the dome. The fault margin consists of a 1 to 3 cm thick, brittlely deformed gouge (L1), truncating a darker, 1-3 cm thick layer (L2) shown in more plan view in Figure 4-3. The unconformable boundary is seen clearly in Figure

4-2 as the transition from the dark, finely foliated layer with aligned, micro-granular lenses (L2) cut by a lighter, unconsolidated layer above (L1), with a wavy onset and angular steps with recurrence intervals of 20-40 cm. L2 grades into a ~2 cm thick, moderately sheared layer below (L3), which further grades into a decimetre-scale core of marginally deformed dome rock (L4).

Table 4-1. Description of sample sets (L1-L4) including density and porosity established through the Archimedes buoyancy method.

Layer	Sample Block Name	Thickness	Density (Kgm^{-3})	Porosity (%)	Description
1	MSHJK2A	1- 3 cm	2410±5	7.3±0.05	Gouge, slickensides
2	MSHJK2A	1- 3 cm	2770±5	3.9±0.05	Plastic deformation
3	MSHJK2B	2 cm	2580±5	4.0±0.05	Transitional zone
4	MSHJK2B	Decimetres	2470±5	5.7±0.05	Bulk material
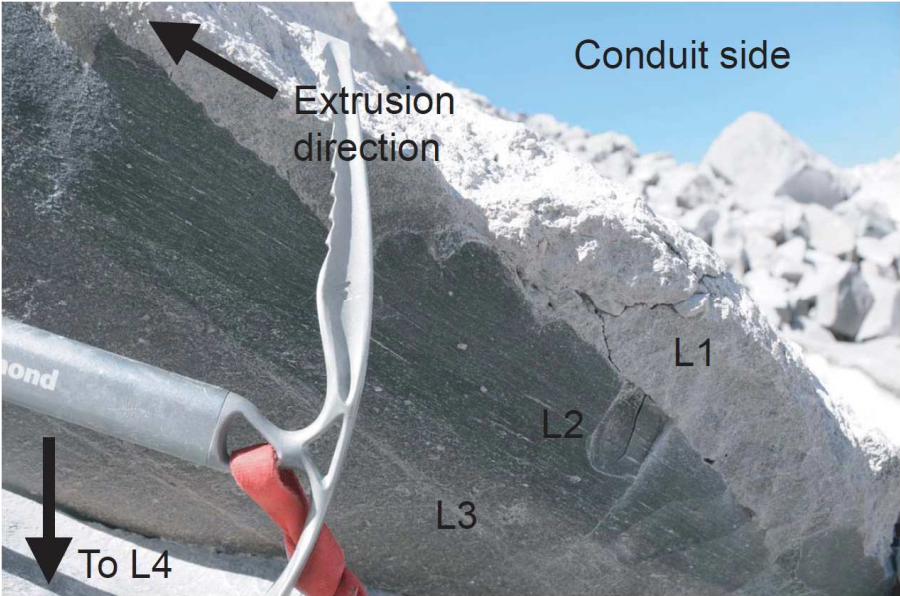
Figure 4-2. Photograph of the margin of Spine 7 showing the gouge zone (L1) with a cross-cutting, unconformable boundary to the darker layer below (L2) which grades into a transitional, moderate shear zone (L3). L4 (not shown) would be located below the ice-axe. The basal margin of the gouge shows a step-like feature which occurred every 20-40 cm along the ~5 m wide outcrop, and cross-cuts the lineated L2.
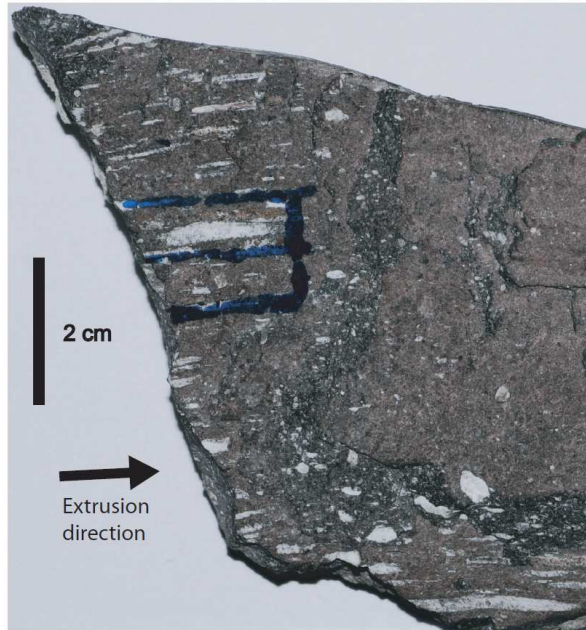
Figure 4-3. Plan view photograph, taken parallel to spine surface, of L2 showing elongate white microcrystalline bands. The arrow indicates the direction of extrusion. The drawn lines delineate the area for thin section preparation.

4.2.2. Porosity and density measurements

Porosity was measured using the Archimedes buoyancy method. In this case porosity is important as an indicator of the degree of compaction or dilation of the samples which result from differing deformation mechanisms along the conduit margin. Porosity varied through the section (Table 4-1) such that the highest porosity was recorded in the gouge (L1) and the lowest porosity in L2. This graded through the somewhat deformed L3 with intermediate porosity to the higher porosity of the undeformed dome rock (L4). Samples extruded earlier in the eruption have relatively higher porosities of 19.7 % reducing to 8.0 % (Smith et al., 2011) over time and finally to 5.7 % for the undeformed dome rock (L4) in this study. Porosity of the gouge is comparable to values of 3.5-8.2 % presented in Schneider (2009), but lower than the 30.3 % porosity presented for unconsolidated gouge in Cashman et al. (2008).

4.2.3. Geochemistry

Whole rock geochemical analysis was performed on fused glass discs in a Phillips Magix-Pro X-ray fluorescence spectrometer in order to establish the chemical homogeneity of the sample set, where heterogeneities would indicate external input into the system. Major element data

presented as oxides in Table 4-2 display only minor variation across the sample set, a quasi-continuous section through the outer surface of spine 7, and represent calc-alkaline dacites (SiO_2= 64.2 ± 0.2 %). Whole rock composition of the undeformed bulk rock, with an approximate extrusion date of September-November 2006, is within the range of other samples measured throughout the eruption, presented in Table 4-3 (Thornber et al., 2008). Loss on ignition (LOI) data acquired through mass change upon heating the sample to 1050 ºC reached values of -0.156 ± 0.4 wt. % thus indicating that little or no volatiles were present, but possibly that minor Fe oxidation occurred.

Table 4-2. Oxide composition from XRF for layers L1, L2, L3 and L4 plus standard deviation of results.

Layer	1	2	3	3	Standard Deviation (%)	Interstitial melt, L2
SiO_2	64.22	64.13	64.21	64.33	0.11	70.71
TiO_2	0.70	0.63	0.63	0.65	4.51	0.23
Al_2O_3	16.96	16.95	16.94	16.92	0.09	16.27
$Fe2O3$	4.70	4.67	4.68	4.69	0.23	1.28
MnO	0.08	0.08	0.08	0.08	0.49	0.03
MgO	1.83	1.87	1.87	1.87	0.90	0.36
CaO	4.75	4.77	4.72	4.70	0.60	3.87
Na_2O	5.02	5.28	5.26	5.17	2.02	5.22
K_2O	1.60	1.47	1.48	1.46	3.67	1.95
P_2O_5	0.14	0.14	0.13	0.14	3.96	0.06
Totals	100	100	100	100		

Table 4-3. Normalised bulk rock chemical composition of samples erupted in April and December 2006 (data from Thornber et al. 2008, collected at the Washington State University (WSU) or the USGS) compared with our sample extruded in September-November 2006.

Sample	SH329-1	SH329-1	MSHJK2B4	SH332-2	SH332-2
Date of eruption	15.04.2006	15.04.2006	09.11.2006	21.12.2006	21.12.2006
Data source	WSU	USGS	This study, LMU	WSU	USGS
SiO_2	65.27	65.18	64.33	65.08	65.16
TiO_2	0.61	0.62	0.65	0.62	0.63
Al_2O_3	17.21	17.18	16.92	17.30	17.20
Fe_TO	3.99	4.06		4.01	4.04
Fe_2O_3			4.69		
MnO	0.07	0.07	0.08	0.07	0.07
MgO	1.80	1.78	1.87	1.84	1.83
CaO	4.65	4.68	4.70	4.70	4.74
Na_2O	4.79	4.75	5.17	4.76	4.65
K_2O	1.47	1.49	1.46	1.47	1.47
P_2O_5	0.14	0.21	0.14	0.14	0.21
Totals	100.00	100.00	100.00	100.00	100.00

4.2.4. Mineralogy

Using optical microscopy the composition of the samples was identified as: plagioclase, amphibole, clinopyroxene, orthopyroxene, apatite and iron-titanium-oxide phenocrysts set in an aphanitic groundmass of predominantly plagioclase and quartz, in agreement with Cashman et al. (2008).

Samples were powdered and prepared for analysis in a Phillips X'Pert Pro Multipurpose X-ray Diffractometer. XRD can be used to identify differences in the mineral assemblage which may arise from isochemical alteration. X-rays diffract from the target sample according to Braggs Law, and data is output in the form of a 2D diffraction pattern (Loubser and Verryn, 2008) of scattering intensity against the scattering angle of the corresponding d-spacing of the diffracting target. X-ray diffraction patterns were examined in the program ADM V6 from Wassermann

(2003), where they were stripped of Kα_2 (a second reflection) and the thresholds were increased to reduce background noise and to make peak identification clearer. The positions, intensities, widths and shapes of peaks are used for identifying the composition of the material, where the various intensities of the peaks indicate the relative amount of each mineral present. XRD indicated the presence of plagioclase, quartz, amphibole, clinopyroxene, orthopyroxene, apatite and iron-titanium oxide with all layers displaying equal proportions with standard deviation of < 1.5 %. This composition was previously observed in thin section and is in accordance with previous works by Cashman et al (2008) and Pallister et al (2008). Semi-quantitative XRD analysis suggests that the rocks contain 77 $\pm$ 3 % of plagioclase and 7 $\pm$ 1 % of quartz, with variable, but less than 4 % each of amphibole, clinopyroxene, orthopyroxene, apatite and iron-titanium oxide.

Uncovered thin sections of each sample were carbon coated for quantitative analysis by wavelength dispersive analysis (WDA) in a CAMECA SX100 scanning electron microprobe. WDA was used to identify the specific minerals within the samples by precision picking points on individual crystals using the onscreen BSE image. WDA identified the same mineral assemblage as established by XRD, and in agreement with Cashman et al. (2008), of plagioclase, amphibole, clinopyroxene, orthopyroxene, apatite and iron-titanium oxide phenocrysts. The opaque iron-titanium oxides larger than 20 μm were found to contain Fe:Ti ratios of between 6:1 and 10:1, but smaller oxides of 1-2 μm, were too small to resolve by WDA (see section 4.2.8 magnetic properties).

Over 200 measurements made within the groundmass of the sample set indicated a difference between L2 and the other layers: Measurements made in L1, L3 and L4 had high variability, with compositions ranging from plagioclase to quartz, many points likely measured at least two microlites and thus WDA was unable to resolve the composition; in L2, compositions were much more stable, the majority of points recorded a rhyolitic composition (Table 4-2) with 71 – 76 % SiO$_2$, although plagioclase and quartz compositions were also noted.

4.2.5. Microstructure

Thin sections of each distinct layer were prepared perpendicular to the surface and parallel to extrusion direction. These were studied for the identification of mineral phases (Section 4.2.4),

for crystal size distributions (Section 4.2.9) and structural features which would constrain the deformation history along the conduit margin.

L4 contains numerous coarse-grained (<2 mm), tabular plagioclase phenocrysts which are largely idiomorphic (Figure 4-4a). The plagioclase has polysynthetic, carlsbad and pericline twinning, and commonly shows chemical zoning rings (Figure 4-4a and b). The crystals rarely show undulose extinction, but are occasionally fractured without further dislocation (Figure 4-4b); one exception arose where a cataclastic plagioclase was sheared into a thin, 1 mm long band. The cores of some of the largest phenocrysts show heavy dissolution textures and recrystallization rims concordant with the chemical zoning of other phenocrysts. The crystals are often internally fractured but the fragments remain intact, evidenced by their tabular shape (Figure 4-4a). The pyroxenes are present as smaller crystals (<0.5 mm) and are chemically homogeneous (Figure 4-4a). The amphibole crystals (< 0.2 mm) show disequilibrium features, with oxidised cores and reaction rims (Figure 4-4a). Overall, the crystals do not show structural fabrics from shearing; they appear to have no crystallographic preferred orientation and only minor amounts of plagioclase have been dislocated. Porosity is evenly distributed throughout, comprising voids between phenocrysts and minor fractures within crystals and the groundmass.
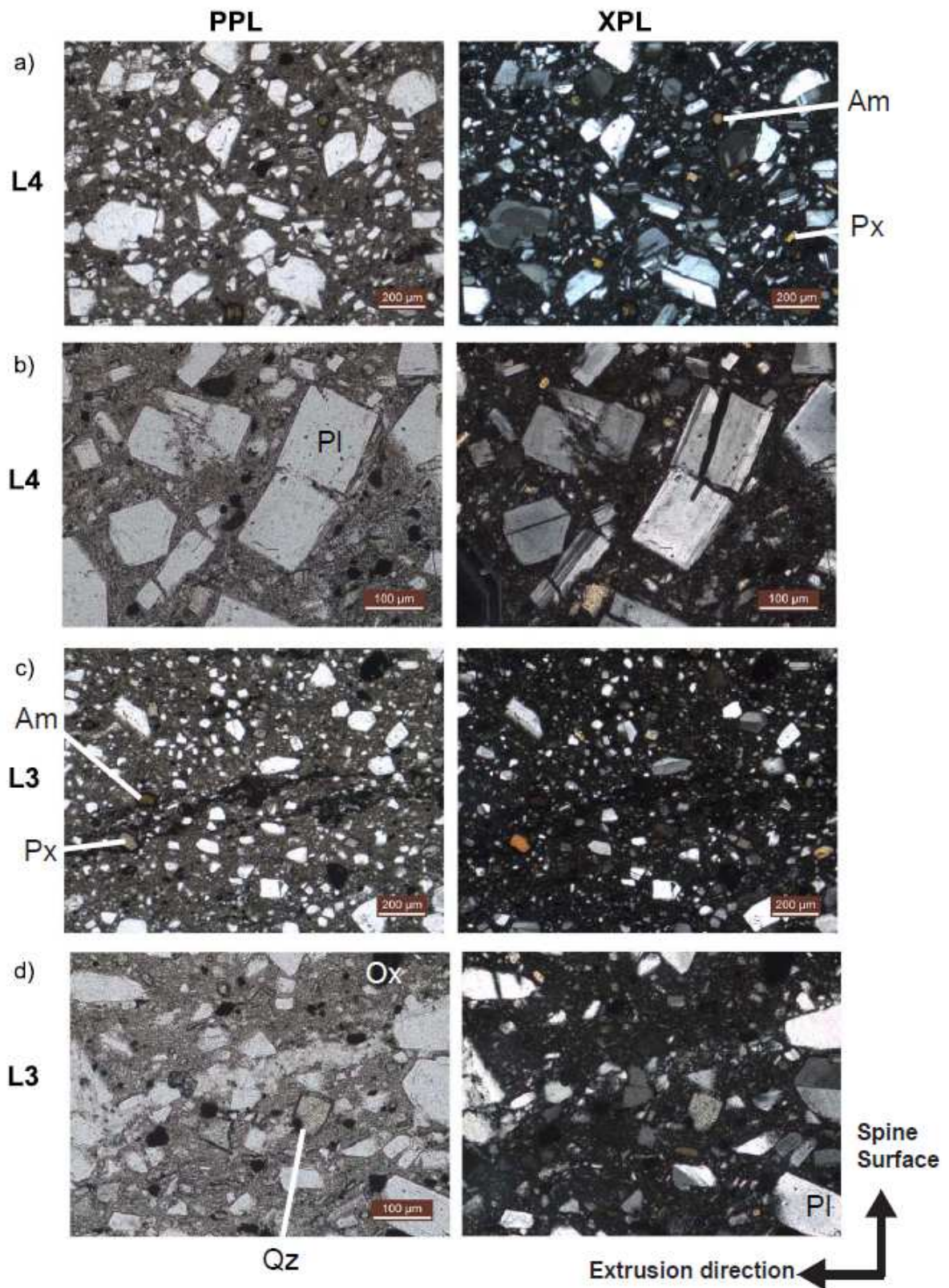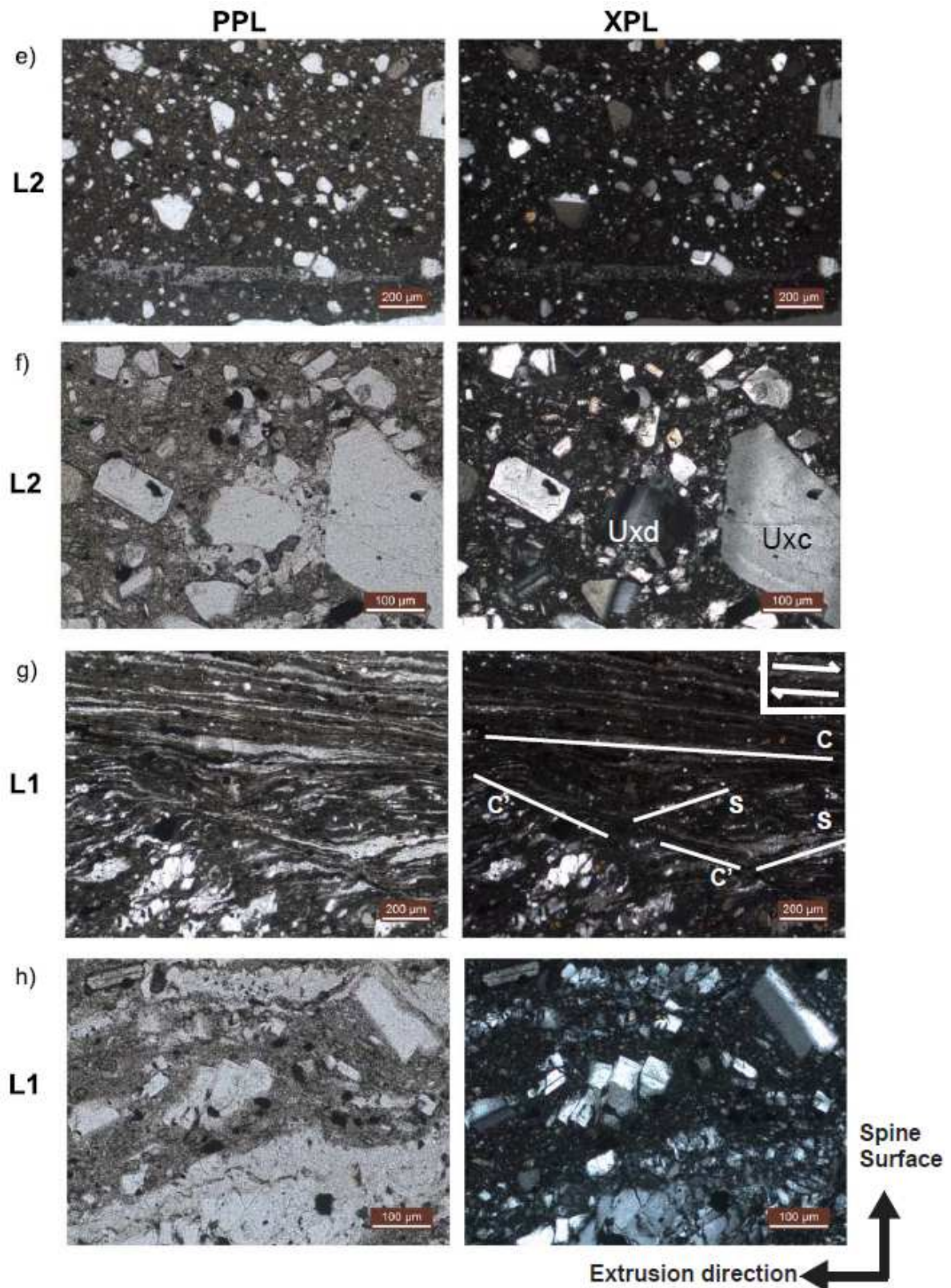
Figure 4-4. Photomicrographs in plain (PPL) and cross-polarised light (XPL). The extrusion direction and orientation with regard to the spine surface are indicated. Images (a), (c), (e) and (g) are taken with a 4x objectives, whereas (b), (d), (f) and (h) were taken with a 10x objectives. (a) L4 contains the highest fraction of phenocrysts which are here idiomorphic.

(b) Examples of plagioclase crystal (Pl) which fractured without further dislocation in L4. (c) L3 shows an increased proportion of larger hypidiomorphic phenocrysts and oxidised shear bands which incorporate a pyroxene (Px) phenocryst, coating it in an oxide rim. An amphibole (Am) with a reaction rim is also present. (d) Crystalline shear bands in L3, showing fine plagioclase fragments surrounded by hypidiomorphic plagioclase, quartz (Qz) and Iron-titanium oxides (Ox). (e) L2 hosts equant hypidiomorphic phenocrysts of plagioclase with undulose extinction and microcrystalline shear bands, (f) Undulose extinction of plagioclase crystals caused by plastic deformation (Uxd) and chemical zonation (Uxc). (g) Examples of partially dislocated and fragmented plagioclase crystals in L1. Shearing (indicated by the arrows) induced the development of cataclastic shear bands showing C-S fabrics. (h) L1 further evidences the development of bookshelf textures in some phenocrysts whereas others were highly fractured to micrometre sizes. In the images the abbreviations stand for: Pl - plagioclase, Px – Pyroxene, Ox – Iron-titanium oxides, Qz – quartz, Am – amphibole.

L4 grades into L3, where phenocrysts (especially plagioclase) become increasingly smaller and hypidiomorphic with rounded and fractured edges (Figure 4-4c and d). The plagioclase crystals host more fractures than in L4, but not always more undulose extinction. Porosity is localised into voids in close proximity to large phenocrysts and minor fracturing persists. We note the increasing presence of shear bands sub-parallel to the layer boundaries. Two types of shear bands are recognised. One type is evidenced by the local oxidation of Fe-Ti oxides and amphiboles, and are inclined slightly from extrusion direction (Figure 4-4c). The bands have irregular widths ranging between 0.1 and 0.3 mm and length reaching up to 25mm; yet, they are straight and parallel, spaced from each other by 3 to 5 mm. The other bands are characterised by cataclastic crystals of plagioclase, without preferred crystallographic orientation (shown in L2 in Figure 4-4e) which run parallel to extrusion direction and layer boundaries.

L2 contains finer and more equant crystals than L3 (Figure 4-4e). The plagioclase phenocrysts are hypidiomorphic, strongly rounded and highly fractured. The cores of the plagioclase show common undulose extinction indicating crystallographic distortion associated with plastic deformation (Figure 4-4f). The edges of some phenocrysts are highly fine grained, showing evidence of fragmentation or rapid recrystallization (Figure 4-4f). One horizon, parallel to the extrusion direction, shows recurrent in-train cataclastic plagioclase shear bands which begin with a bulbous onset and thin to termination away from the direction of spine extrusion (see

Figure 4-3; Figure 4-4e). Dissolution textures are observed within plagioclase (Figure 4-4e). The amphiboles show strong reaction rims and a degree of oxidation. The crystals of pyroxene, especially the smaller ones, are often rounded (Figure 4-4e). Only very few larger crystals remain hypidiomorphic. Few fractures are seen in the groundmass, rather porosity is concentrated into the microcrystalline plagioclase bands or in voids and fractures in and around phenocrysts.

L1 is in discordant contact with L2, cross-cutting the direction of the shear bands below the boundary, while eroding and incorporating material from L2. Structurally, L1 is divided into both banded (Figure 4-4g) and massive (Figure 4-4h) regions. The massive (non-banded) regions show a high degree of damage to plagioclases (exceeding that of the pyroxenes and the amphiboles), which are xenomorphic and do not exceed 1mm. Fracturing and dislocation of plagioclase crystals result in bookshelf textures (Passchier and Trouw, 2005; Siddoway et al., 2004) or broken crystal fragments accumulate in lenses (Figure 4-4e). The banded areas, in contrast, are very fine grained (generally $<<$ 0.1 mm) and show C-S fabrics, locally superimposed by C' foliation (Figure 4-4g). The higher porosity in this layer is accounted for by an increase in fracture density and larger voids between the phenocrysts in the non-compacted bands.

BSE images (Figure 4-5) from a CamScan X500 Crystal Probe FEG-SEM were used to evaluate microstructural differences between layers. The backscattering coefficient varies according to the atomic weight, where heavier elements have a lower backscattering coefficient and are lighter in colour in BSE images (Reed, 1996). Plagioclase crystals have a similar backscattering coefficient to the groundmass which makes their distinction challenging, whereas pyroxenes and iron-titanium oxides are lighter and amphibole and quartz are darker than the groundmass (Figure 4-5).
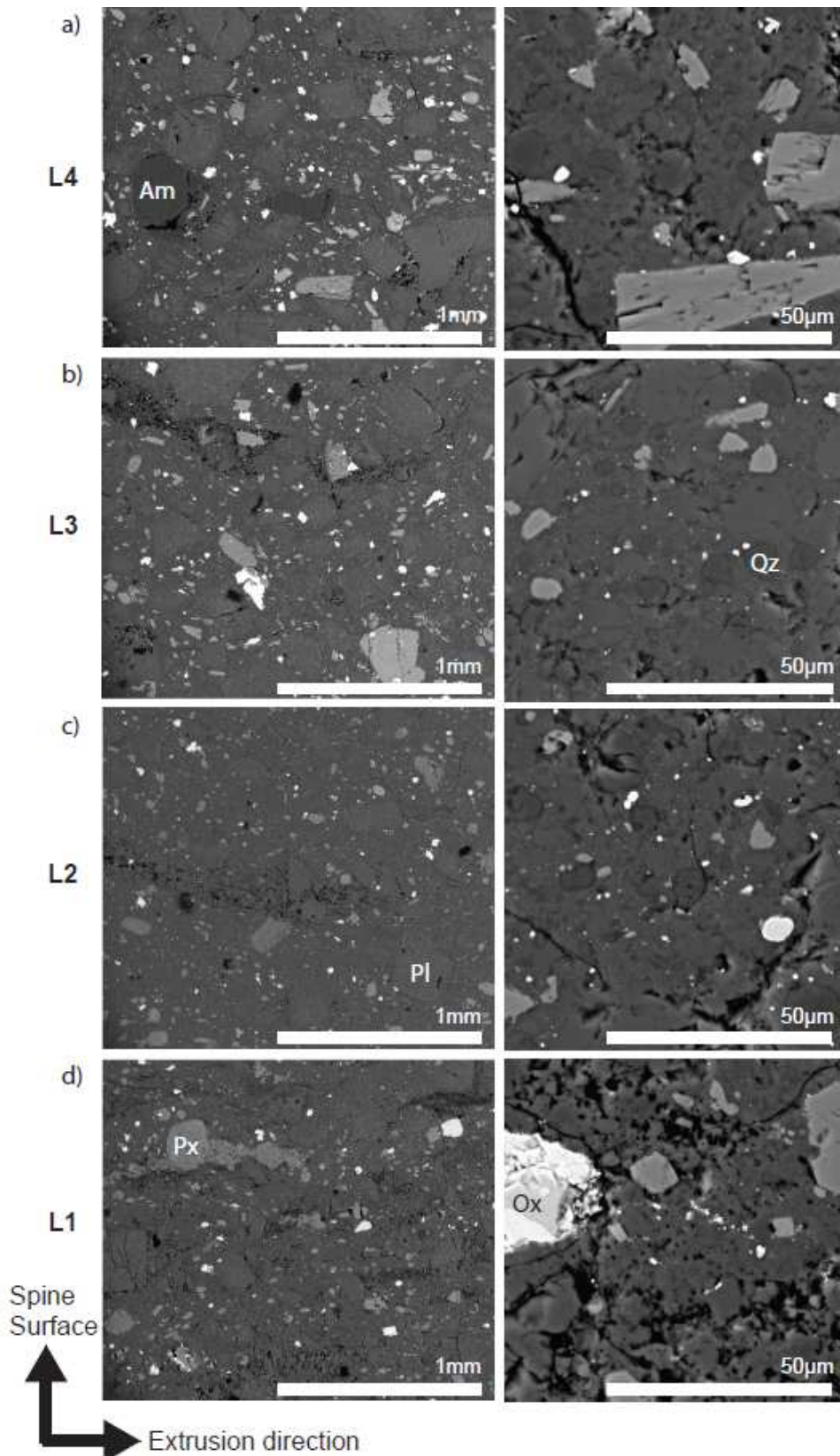
Figure 4-5. SEM back-scattered electron (BSE) images at low (left) and high (right) magnifications of (a) idiomorphic plagioclase and pyroxene phenocrysts with fractures that propagate out into the groundmass, in L4; (b) hypidiomorphic crystals and porous bands of plagioclase fragments as well as tears (voids/ pores) in pressure shadow of phenocrysts. At

high magnification, we again note the presence of restitic quartz; (c) equant phenocrysts and a porous microcrystalline plagioclase band. At high magnification we observe restitic quartz and occasional fractures propagating through a microlitic to glassy groundmass in L2; and (d) comminuted phenocrysts forming sub-parallel bands hosted in a fine grained porous matrix in L1. The extrusion direction and orientation with regard to the spine surface are indicated. In the images the abbreviations stand for: Pl - plagioclase, Px – Pyroxene, Ox – Iron-titanium oxides, Qz – quartz, Am – amphibole.

From BSE images we identified a decrease in grain size from the bulk rock through to the gouge (Figure 4-5), as also noted in thin sections (Figure 4-4). In L4 we see idiomorphic, tabular plagioclase phenocrysts and a porous network consisting of evenly-dispersed, fine fractures and occasional voids or vesicles (Figure 4-5a). In the higher magnification image it is possible to differentiate between grains in the groundmass, which appear to be micron scale. From L4 to L3 there is a notable increase in shear damage, evidenced by localised comminuted bands of plagioclase fragments (Figure 4-5b, left). Porosity in L3 tends to be restricted to these bands or pressure shadows around phenocrysts. In the higher magnification image of L3 (Figure 4-5b right), and even more clearly in L2 (Figure 4-5c), we see rounded microlites of <5 µm; these are interpreted as restitic quartz with dark reaction rims. The microlites of the groundmass in L2 and L3 (Figure 4-5c and b) are less readily identifiable than in L4 (Figure 4-5a) and overall, the groundmass is more single-tone and appears glassy. In L2 there are even fewer fractures than in L3 and porosity is localised into microcrystalline bands of plagioclase (as seen in Figure 4-3) which have a rounded front and tail-off away from the direction of extrusion (Figure 4-5c). A large amount of comminuted phenocrysts of plagioclase and pyroxene are present in L1 (Figure 4-5d), and fractures propagate in and around phenocrysts, passing through the microcrystalline matrix. In the higher magnification image it is possible to identify individual grains in the porous matrix (Figure 4-5d, right).

4.2.6. Plagioclase crystal size and shape distribution

Thin section scans were used for crystal-shape and -size distribution analyses on plagioclase phenocrysts above a detection size of $0.01mm^2$ (high confidence that all grains above this size were included and shape was representative). The scans represent a quasi-continuous transect through the fault zone, and were split into 11 segments of equal size (10 mm*4 mm). Image analysis was carried out using Image J (Abramoff et al., 2004). Scanned images were converted

to binary, where plagioclase crystals (which are the most abundant) were replaced by black pixels, and groundmass as well as other crystals and pores were converted into white pixels (Figure 4-6). Average numbers of detected crystals and the percentage of plagioclase phenocrysts decrease from L4 through to L1 (presented in Table 4-4). Errors in measurements stem from the segmentation process (Kittler et al., 1985) and are estimated by varying thresholds to be less than 3 % total.
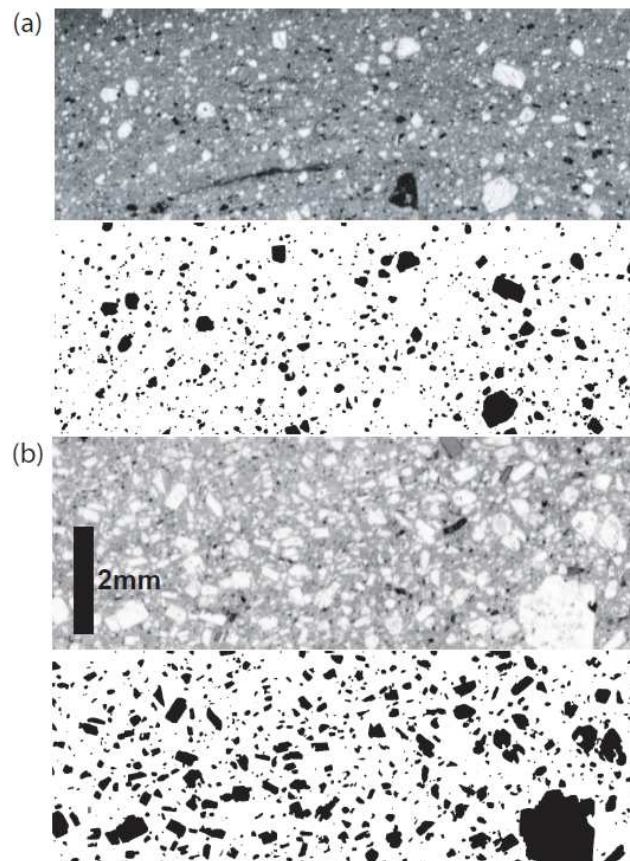
Figure 4-6. Thin section scans and resulting binary images for (a) plastically deformed L2 and (b) undeformed bulk rock. Binary images show light coloured crystals as black pixels and groundmass (as well as dark crystals such as amphiboles and Fe-Ti oxides) as white pixels. The binary images were subsequently used for grain size and shape analysis.

Table 4-4. Average number of detected phenocrysts, area occupied and plagioclase crystallinity (%) from an equal area of each layer, from binary images.

Layer no.	40mm^2 area		Plagioclase phenocrysts (%)
	number of plagioclase phenocrysts	total area plagioclase phenocrysts (mm^2)	
L1	729	5.71	14.3
L2	998	6.94	17.4
L3	950	7.93	19.8
L4	807	8.98	22.4
L1-2 boundary	1104		

Cumulative frequency of abundance of the crystal population was binned according to idealised crystal diameters (square-root area, as plagioclase are quadrilateral) into 60 µm bins using Origin Pro 8. A plot of Log cumulative frequency (from largest to smallest) against crystal diameter produced a negative trend with a linear central portion (Figure 4-7). [Deviation from linear occurs at minima and maxima due to a shortage of data.] The slope of this linear portion is a function of the spread of data, such that the most negative slope indicates a higher proportion of small crystals and vice versa (See Figure 4-7). The values of slope are plotted as a function of distance from the spine surface (Figure 4-8) and indicate that grain size is variably reduced from the starting material to L1-L3. The highest fraction of small crystals was observed for L2 (highest slope: Figure 4-7, Figure 4-8), followed by the top surface of the gouge (L1) which represents the contact to the conduit wall. This is proceeded by L3 and then the lower portion of the gouge (L1), in close proximity to its basal contact with L2 (L1-L2 in Figure 4-7). Finally, L4 has the highest fraction of larger crystals (lowest slope: Figure 4-7, Figure 4-8).
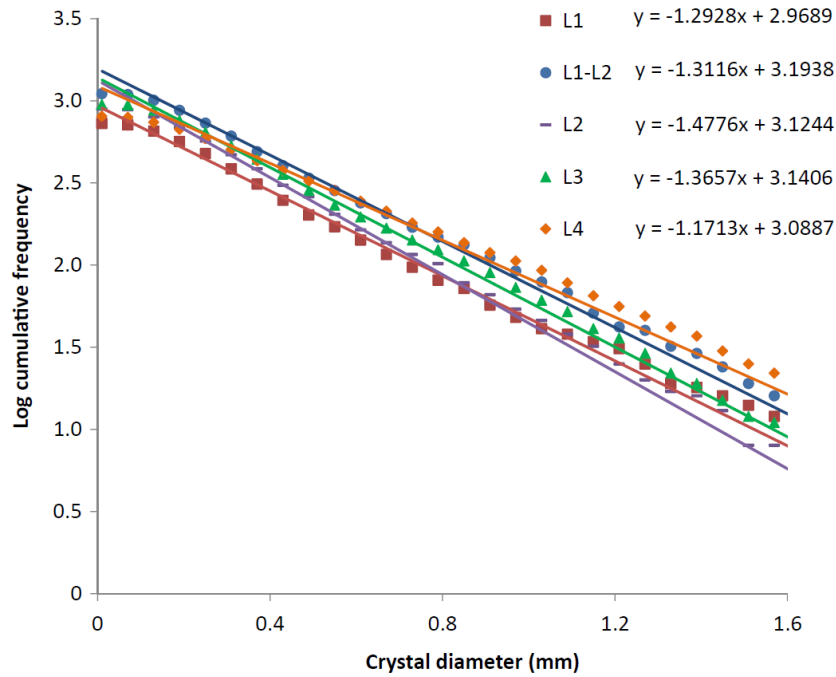
Figure 4-7. Log cumulative frequency (from largest to smallest) against crystal diameter, here the data from 11 analysed images have been split into their corresponding layers (L1 to L4). The cataclasite band at the boundary of L1 and L2 is labelled L1-L2. Slope is highest in L2 and lowest in L4 i.e. there is a higher proportion of small crystals in L2.

Using Image J the average circularity of grains (with contiguous grains, including plagioclase bands, excluded during acquisition of data) in the same crystal population was calculated using:

$$\text{Circularity} = 4\pi \, (A \, / \, p^2) \qquad\qquad\qquad\qquad \text{(Eq. 7)}$$

where A is crystal area and p is the perimeter. Circularity is a measure of the compactness of a shape decreasing from 1, a circle, as elongation increases toward 0, which would idealise a geometrically impracticable line [As a reference, a square equals 0.785]. The circularity varied between layers concomitantly with slope, such that the values for L2 and L3 were higher than either the gouge or the starting material (Figure 4-8).
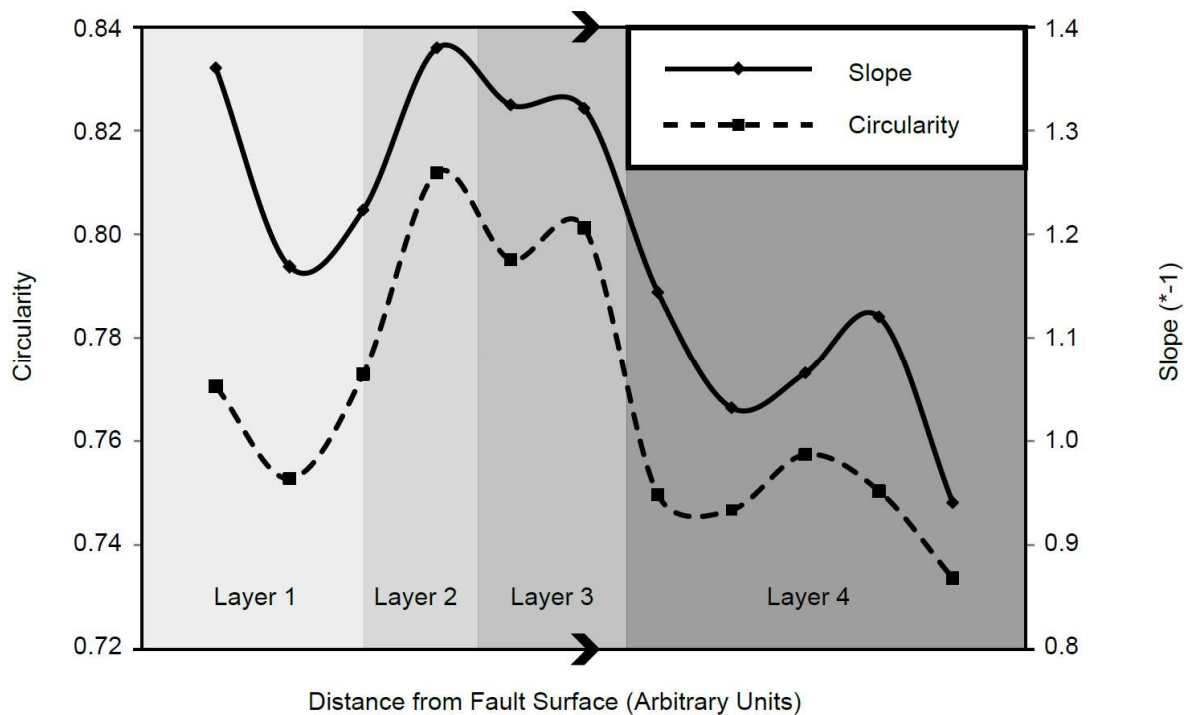
Figure 4-8. The inverse linear fitting from a semi log plot of cumulative frequency against crystal diameter, or "slope", and circularity variation from the 11 binary images which represent a quasi-continuous section through the spine surface (through L1-L4). Errors for circularity are negligible and for slope are less than 3 % and originate from the segmentation process.

In an undeformed rock the primary axis of crystals should average 45° from any given plane in 3D to represent random orientation. In the 2D binary images this plane was defined as a line parallel to the movement direction of the extruding spine. As anticipated L4 shows no preferred orientation owing to the near absence of deformation, average X-axis orientation was ±45°. This value was also seen in both L2 and L3 where crystals were more equant due to comminution and rounding during deformation, thus the primary axis is difficult to distinguish. The majority of the gouge, which aligns into cataclasite bands (as illustrated in Figure 4-5d), had a significantly lower value of ±21°, which indicates at least partial crystal alignment due to brittle processes.

4.2.7. Kinetic properties

Thermal analysis using differential scanning calorimetry (DSC) was performed in a NETZSCH DSC 404 F1 Pegasus, calibrated against the specific heat capacity (Cp) of a single crystal of sapphire at constant pressure and temperature (calibration is tested against standards of known

melting points). DSC is used to establish Cp as a function of temperature, which can then be used to identify the differences in thermal history between samples, including recognition of melting temperatures, detection of glass fractions produced by frictional melting and to ascertain of the glass transition temperature (Tg). If glass is present both Cp and the thermal expansion coefficient will diverge from a linear trend at Tg (Gottsmann et al., 2002; Ojovan, 2008).
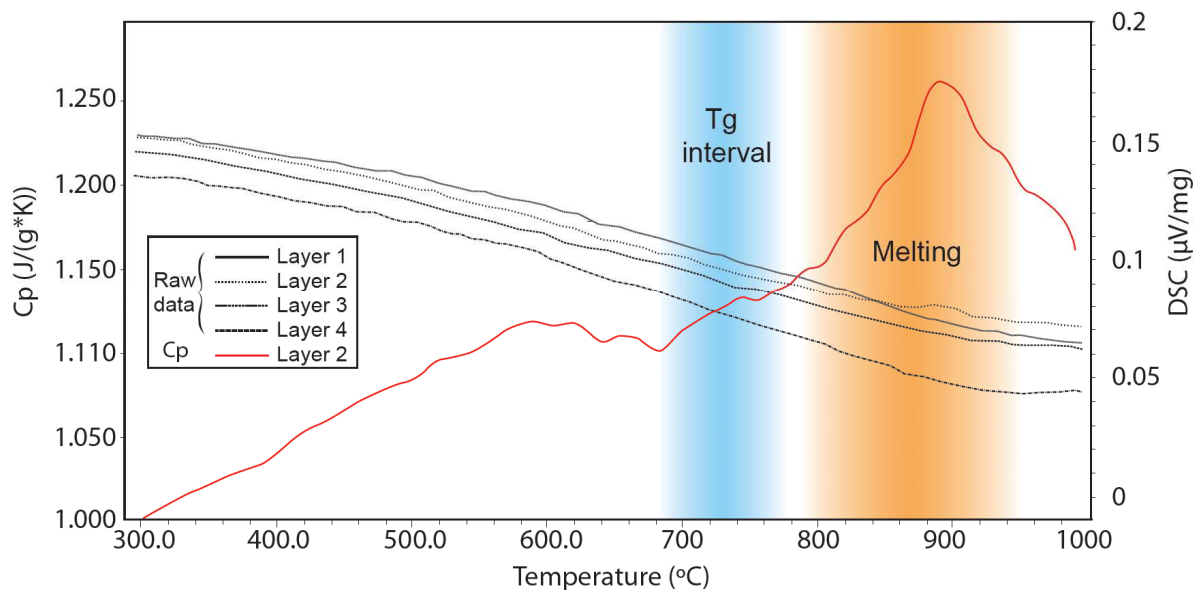
Figure 4-9. DSC curves for L1-L4 and specific heat capacity (Cp) for L2. Note the deviation from the linear trend in DSC for L2 at ~745 ᵒC corresponding to a minor peak in Cp which we interpret to be the glass transition temperature (Tg). The major peak in Cp at ~890 ᵒC may represent the melting temperature of the mineral assemblage.

The Cp curve reveals two endothermic features in L2, which do not occur in L1, L3 and L4, thus indicating that L2 behaves in a kinetically distinct manner. Noticeably, there is a very large peak at about 890 °C. We attribute this large endogenic event as melting of the L2 groundmass as the increase in Cp is larger, and occurs at too high a temperature to correspond to the glass transition of a melt phase (Giordano et al., 2005; Giordano et al., 2008; Gottsmann et al., 2002). In the region of 690-770 °C the Cp curve from L2 shows a significant rise, with a peak at ~745 °C. We attribute this peak to the glass transition of a melt phase in the groundmass of L2. In order to verify this finding we have independently estimated the expected signature of a glass transition event in the Cp trace of L2 in two ways.

Firstly, we have calculated the expected Tg based upon the chemistry of the melt phase (see Table 4-2) using the calculation method for viscosity and Tg provided by the global viscosity model (GRD) of Giordano et al. (2008). Taking a calorimetric heating rate of 10 °C/ min, together with the shift factor for deriving viscosity at Tg, from Gottsmann et al. (2002), we obtain an estimated Tg of 727 °C. This is in excellent agreement with our observation of the small endothermic peak at 745 °C for the L2 sample.

We have also estimated the magnitude of the "relaxational heat capacity" (*i.e.*, the difference between the extrapolated glassy heat capacity value and the observed relaxed liquid value) just above the glass transition peak. This value varies greatly with melt composition. An entirely glass sample of calc-alkaline chemistry, similar to the composition of our samples, would yield a relaxational heat capacity of 7 %. This is entirely consistent with the observed magnitude of the relaxational heat capacity here (a few %), given that our samples consist of at most 20-30 % melt.

4.2.8. *Magnetic properties*

Fault zones may display magnetic anomalies associated with magnetic carrier alignment along the fault plane (Hayman et al., 2004) or as a result of frictional heating (e.g. Nakamura et al., 2002; Ferre et al., 2005). Thus, the bulk magnetic susceptibility of the sample set was measured in a Bartington HS2 susceptibility meter for two specimens of each of L1-L4 (Table 4-5), with the primary aim to establish whether any frictional heating or alignment of the magnetic carriers had occurred during frictional sliding. The magnetic susceptibility was observed to remain constant across all layers. The natural remanent magnetisation (NRM) of each layer was then measured in a 2G cryogenic magnetometer. Mass normalised NRM intensity increased from L4 through to L1 (15 times higher). The same factor is found when further normalising the mass normalised NRM intensity with the concentration dependent saturation remanence (M_{rs}).

Table 4-5. Results of magnetic susceptibility; natural remanent magnetisation and Curie temperature measurements which highlight differences between for L1, L2, L3 and L4.

Using a Variable Field Translation Balance (VFTB) by Petersen Instruments, the Isothermal

Layer	Magnetic Susceptibility (10^{-5} SI units)		Variability (%)	NRM		Curie Temperatures (ºC)	
	Specimen A avg.	Specimen B avg.		NRMm intensity (Am^{2}kg^{-1})	NRMm/ Mrs	Peak 1	Peak 2
1	106.1	105.2	0.8	1.99E-03	4.95E-02	375	535
2	96.1	85.7	10.8	1.25E-03	2.07E-02	348	532
3	97.2	91.4	6.0	6.61E-04	1.61E-02	360	528
4	113.9	87.0	23.6	1.26E-04	3.24E-03	337	527
Variability (%)	15.6	18.5					

Remanent Magnetisation (IRM), backfield, hysteresis and thermomagnetic curves were measured in this order to identify magnetic remanence carriers and domain states. The dataset was analysed using the RockMagAnalyzer software by Leonhardt (2006). IRM and backfield curves saturate at approximately 200 to 300 mT (Figure 4-10a), indicative of low coercive material (Leonhardt 2006). Quantitatively this is shown by the S300 parameter (Bloemendal et al., 1992) of 0.97-1.00. This value is calculated from the backfield measurement via (1-($M_{at\text{-}300mT}/M_{rs}$))/2 and hence is a measure of the degree of saturation at 300 mT. Values close to 1, as observed here, indicate low coercive material such as titaniferous-magnetite. Coercivity of remanence (B_{cr}) values are 25-30 mT, and hysteresis plots of all four specimens are very similar (Figure 4-10b, inset). Hysteresis and backfield data combined in a Day plot (Day et al., 1977) with borders and mixing lines by Dunlop (2002) show almost identical values for L1-4 (Figure 4-10b). All specimens plot clearly in the pseudo-single-domain range, close to a single-/ multi-domain (SD/MD) mixing line. But L2 stands out from the other layers by having both slightly larger M_{rs}/M_s and slightly lower B_{cr}/B_c (coercivity) values, which suggest that it is closer to the single-domain range than the others.
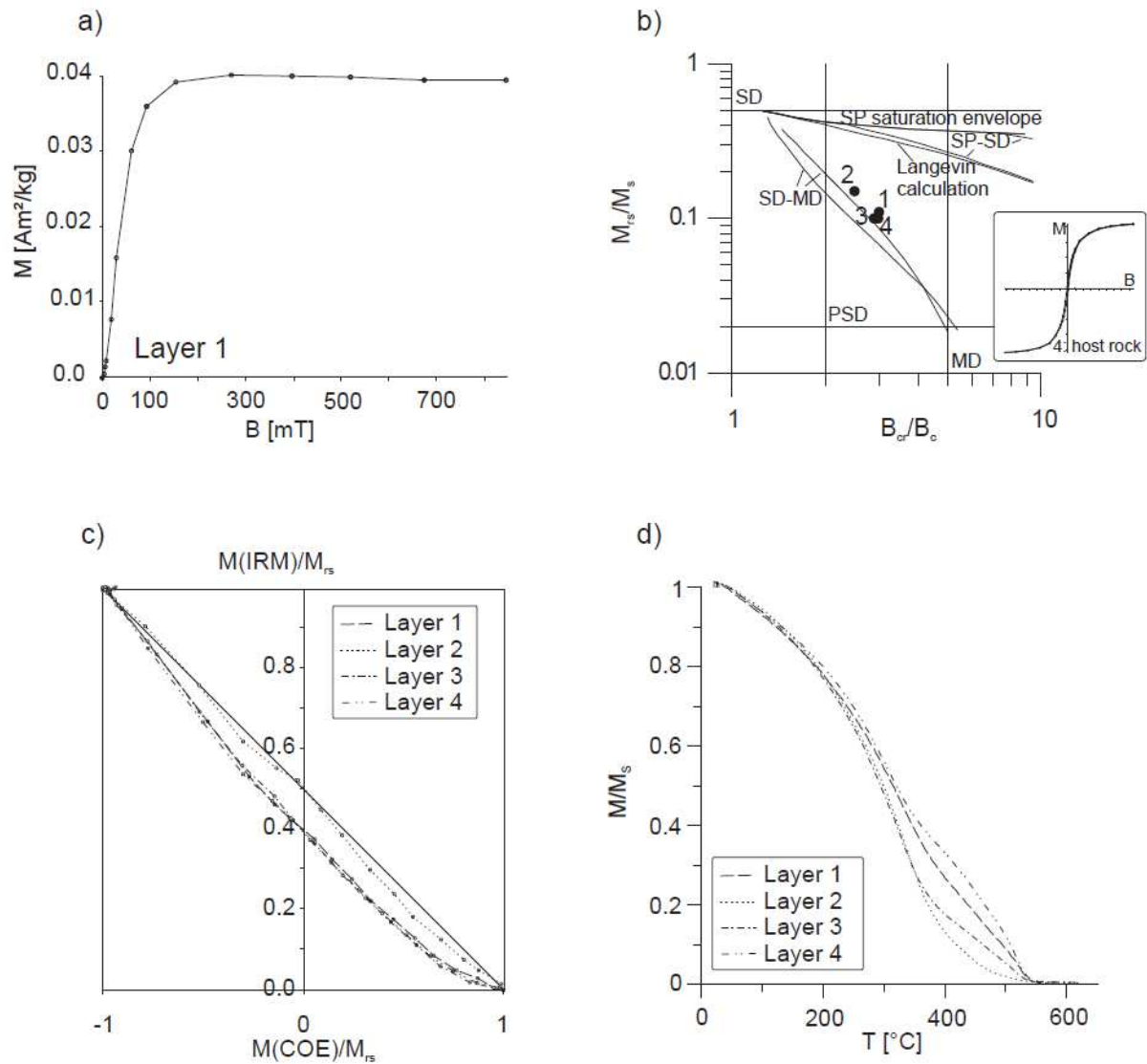
Figure 4-10. Magnetic analyses: (a) Fast saturating IRM curve of the gauge. (b) Day plot (Day et al., 1977) with borders and mixing lines by Dunlop (2002): All samples plot in the pseudo-single domain range close to a single-multi domain mixing line. L2 is closer to the single domain range than the rest of the samples. Inlay: hysteresis curve of the bulk rock. (c) L2 plots close to the ideal line in the Henkel plot (1964), i.e. close to single domain. (d) Normalised thermomagnetic heating curves show trend from two to mainly one Curie temperature.

Henkel plots (Henkel, 1964) further identify differences between layers. For these plots backfield and IRM data (*i.e.* remanence data) are plotted together (Figure 4-10c), as opposed to the Day plot which uses in-field data and is therefore influenced by paramagnetic and multi-domain contributions and cannot give a definitive answer to the grain size of remanence carriers. The diagonal of the Henkel plot represents ideal Stoner-Wohlfarth particles; that is,

uniaxial non-interacting single-domain particles (Wohlfarth, 1958). The line of L2 is close to this ideal (Figure 4-10c), whereas the other samples plot below the line, indicating remanence carriers in the pseudo-single-domain range or a mixture of different grain sizes.

All thermomagnetic heating and cooling curves (no alteration occurs during the measurement) show two Curie temperatures, which are identified as kinks in the M/M_s versus temperature plot (Figure 4-10d): the first at 340-370 °C and the second at ~530 °C. When the magnetisation is normalised to M_s a difference in the prominence of the two Curie temperatures and, hence, of the two contributing mineral phases is observed for the different layers. For the undeformed rock (L4) both kinks in the thermomagnetic curves are equally important. The second Curie temperature becomes less distinct in the gouge (L1), and in L3, and is almost undetectable in L2; hence increasing amounts of the total magnetisation from L4 to L2 seem to be due to the mineral with the lower Curie temperature.

The magnetic carriers can be observed in BSE images with the SEM, but their small size (1 to 2 μm) restricts their identification via optical microscopy or WDA, unlike the coarser, anisotropic ilmenites (20 to 60 μm), which have a Curie temperature below room temperature. Surface red flow marks in very thin films suggest the presence of hematite, but in such small concentrations that it cannot be monitored during the VFTB experiments.

4.3. Interpretation

The multitude of analyses performed on the four structurally distinct layers across the outer surface of spine 7 permits the distinction of their rheology. Bulk composition by XRF confirms a calc-alkaline dacite, in agreement with Thornber et al. (2008). Composition varied little across the fault surface transect, indicating that the gouge of spine 7 consists almost entirely of the 2004-2008 dacite and input of conduit wall material from any prior eruption was negligible. XRD analysis also showed no variation in the mineral assemblage across the sample set, indicating that there was no major alteration.

The undeformed dome rock has a measured density of 2470 Kgm^{-3} and an evenly dispersed, vesicular porosity of 5.7 vol. % (Table 4-1). Dilation due to fracturing led to higher porosity in the gouge, whereas the deformation undergone in L2 and L3 reduced porosity such that the

porous network consisted primarily of tears which result from ductile or plastic deformation of the groundmass around the rigid phenocrysts (Schultz and Fossen, 2008; Smith et al., 2001).

The invariance of geochemical and petrological state through the section suggests that the different structures documented in our samples must be due to the dynamics of the eruption. Indeed, this study provides evidence that deformation mechanisms, not previously reported in lava dome extrusion scenarios, played an important part in the ascent-controlled deformation of spine 7. The grain characterisation, kinetic behaviour and magnetic data highlight L2 in particular as having undergone a markedly different mechanical and thermal history.

L2 contains both the highest circularity and highest proportion of fine-grained phenocrysts (Figure 4-8), suggesting that frictional deformation processes are likely to have participated in the reduction of crystal size and enhancement of circularity. This is accounted for by the pulverisation and comminution of elongate, tabular plagioclase crystals into smaller, more equant, but still-angular shapes, followed by partial frictional melting and plastic deformation to reduce angularity and exceed the circularity value of a square. However, the equant nature of the crystals masks the observation of any preferential alignment of the grains, which have a random orientation of $\pm45^{\circ}$ according to the grain analysis.

The crystal shape analysis showed a lower circularity for the phenocrysts of L1, due to the fracturing, by comminution and cataclasis, of sub-rounded crystals present in L2-L3. This process ought to increase the population of finer crystals (increase in slope; Figure 4-8), whereas a relative increase of coarser crystals is seen (decrease in slope; Figure 4-8). This discrepancy is explained by the continued comminution (Kennedy et al., 2009; Monzawa and Otsuki, 2003) of phenocrysts to a size below the detection threshold of 0.01 mm^2 in our analysis. Thus the observed relative increase in the larger fraction is in fact better described as a relative decrease in the finer detectable fraction (Kennedy et al. (2011) note grain sizes <2 µm in the fault gouge); indeed, a significant increase in detected crystals was observed in the L1-L2 boundary (see Table 4-4), which likely captures this comminution in progress. The continued breakup of the smaller phenocrysts led to a lower overall fraction of crystals from L4 through to L1. This process also resulted in localised areas of crystal alignment within cataclastic shear zones (see Figure 4-4), a result of brittle processes, as evidenced by an average grain alignment $\pm21^{\circ}$ from horizontal in the banded region of L1.

BSE images show that the microlite size and shape in the groundmass is variable between layers. The microstructures of L2 (and to some extent, L3), dissolution textures and undulose extinction in plagioclase, rounding of pyroxene and alteration and oxidation of amphibole rims indicate the occurrence of heating and melting in its formation (Curewitz and Karson, 1999; Lin, 1999; Spray, 2010; Swanson, 1992). Restitic quartz in the groundmass of L2 and L3 (Figures 2-5c and b, respectively) display silica-rich, glassy rims (Holness, 2002) which could result from suspension in a partial melt (Altenberger et al., 2010; Holness, 2002; Masch and Preuss, 1977; Wenk, 1978). The melting temperatures of the crystal assemblage, hornblende at 700-1000 °C, plagioclase at 1100-1600 °C (with temperature increasing with Ca content), pyroxene at ca. 1400 °C, and quartz at 1515 °C to 1730 °C (Spray, 1992), help constrain the temperature at which the observed deformation may be achieved. From the modest occurrence of melting of the plagioclase crystals coupled with the presence of restitic quartz, we interpret frictional heating in L2 to have reached approximately 1100 °C.

The observation of the glass transition exclusively in the L2 sample is further evidence that this layer is unique in that it contains a substantial fraction of glass in the groundmass. All other layers therefore contain little or no glass, in keeping with Pallister et al. (2008) who found < 2 % glass in dome and gouge samples, erupted since 2005. Also unique to L2 is the onset of melting at ~890 °C during DSC, which indicates that the glass-bearing L2 also behaves in a thermodynamically distinct fashion during heating.

Magnetic results also support a difference between L2 and the other layers: When NRM is normalised with saturation remanence or saturation magnetisation, the value for L2 is six times higher than in the undeformed dome rock (L4). The gouge (L1), which results from comminution of the earlier L2 shows an even higher value (15 times), which might be due to inhomogeneous dispersion of crushed L2 in the gouge. L2 shows close proximity to the single-domain range, whereas the other samples have remanence carriers in the pseudo-single domain range or a mixture of different grain sizes. Thermomagnetic heating curves for all samples show two Curie temperatures (at 340-370 °C and 530 °C) with the higher temperature becoming less prevalent from L4 to L2. The disappearance of the second Curie temperature together with the more single-domain-like behaviour of L2 suggests that the carrier with the lower Curie temperature is closer to single-domain whereas the one with the higher Curie temperature is more multi-domain-like. Due to the low coercivity of the samples it is most likely that the remanence carriers are titanomagnetites. Following the relationship between Ti-content and

Curie temperature (Dunlop and Özdemir, 2001) the low Curie temperature corresponds to a Ti-content of 0.4 (TM40) and the high Curie temperature to one of 0.1 (TM10). The trend towards the lower Curie temperature carrier (TM40) in L2 might be due to reduction of TM10, which could result from frictional heating at temperatures exceeding 1000 ℃ (Chen et al., 2011).

Differences in susceptibility, NRM and Curie temperatures between the different layers are significant, but not as high as those observed in granites by Nakamura et al. (2002) or Ferre et al. (2005). This is probably due to the different geological setting in which they develop. Granitic host rocks under adiabatic (Nakamura et al., 2002)lithospheric conditions bear a negligible amount of ferromagnetic particles, whereas the MSH dacite formed in a volcanic environment with elevated thermal conditions and contains titanomagnetite and thus, carries a strong remanence. Even though the NRM of L2 would be overprinted during frictional melting, no strong difference to the NRM intensity of the host rock is to be expected: Much of the remanence is still carried by the original TM40 and an additional amount is carried by new TM40 which formed by reduction of the TM10.

Our interpretation is that extreme frictional processes on the margin of spine 7 led to frictional melting. Given the low lithostatic pressure and high geotherm, active volcanic settings represent unique environments for faulting and carry high potential for frictional melting. The preserved signature of frictional melt is pseudotachylyte, characterised by microlitic, cryptocrystalline or glassy textures and spherulites resulting from rapid cooling of frictional melts (Di Toro et al., 2009; Lin, 2007). Experimental studies estimate frictional melting of igneous rocks at 1100-1550 ℃ (Lavallée et al., 2012; Lin and Shimamoto, 1998). Thus in high temperature extruding magma only a small temperature increase is required to induce melting. The frictional melt would remain at elevated temperatures for longer than usual due to the high geotherm of volcanic environments, permitting near-equilibrium melting followed by slow crystallisation, preventing the development of signature pseudotachylyte characteristics.

4.4. Discussion

Significant differences in the investigated fault zone have been observed compared with earlier studies of MSH (Cashman et al., 2008; Kennedy et al., 2009). These studies of the spine margins noted a 1-3 m gouge layer (Cashman et al., 2008) with multiple sub-parallel layers of slickensides parallel to strike direction (Kennedy et al., 2009). This contained zones of

cataclasite to ultracataclasite formed entirely within the brittle regime, post-crystallisation, in the upper 1 km of the conduit (Cashman et al., 2008). Formation of fault products throughout the eruption was concomitant with microseismic "drumbeats" of M 0.5-1.5 which persisted at intervals of 40-80 s based on daily averaged values (Moran et al., 2008). Kennedy et al. (2009) took each "drumbeat" to represent ~5 mm slip (Iverson et al., 2006) along a strike length of 98-190 m on alternating sub-parallel fault planes, to estimate that each event produced an approximately 0.4 mm thick layer of gouge. These "drumbeats" are interpreted as the physical manifestation of a stress drop which occurs during failure, or slip, along the fault surface (Kennedy and Russell, 2011; Kennedy et al., 2009).

Spine 7, like previous spines, shows evidence for extreme frictional processes in the form of a gouge layer with slickensides. We also observed cataclasites first identified by Cashman et al. (2008) interspersed within the gouge layer, and which likely developed during transportation of the pre-formed gouge to the surface (Kennedy et al., 2009). In addition to this we also note a seemingly plastically deformed layer.

Although the gouge layer is much thinner at our locality than that observed in the earlier part of the eruption, we see no reason to employ an explanation of formation other than the coseismic slip proposed by Kennedy et al. (2009). We concur that extreme grain size reduction and cataclasite formation in the brittle gouge is evidence of the strain-weakening behaviour of the MSH dacite (Cashman et al., 2008). The difference in total thickness of the gouge can be explained by a combination of decrease in "drumbeat" event rate (which was noted, but perhaps not to the extent of a 99 % gouge-thickness reduction from 3m to 3cm) and a reduction in displacement for each individual event, as slip was found to be linearly proportional to the thickness of the gouge layer formed (Kennedy et al. 2009). Extrusion rate slowed from 5.9 m^3s^{-1} to 0.7 m^3s^{-1} during late 2006 (Schilling et al., 2008) concordant to this thinning in fault zone thickness.

We postulate that the temporal development of the slip surface along the conduit margin proceeded as follows: During the onset of the eruption in 2004, high strain rates in the ascending magma led to strain localisation and the formation of shear zones along the shallow conduit margin, where shear stresses were highest (Hale and Wadge, 2008). This shear zone then propagated deeper (Cashman et al. 2008) as the extruding magma continued to exploit the existing surfaces along the pre-sheared conduit margin. The shear stress required for sliding

along a pre-existing fault plane is lower than that required to initiate new fractures within intact host rocks (Scholz, 1998). Repeated mm-scale sub-parallel slip events at the conduit margin led to the formation of a 1-3 m thick gouge layer (Cashman et al., 2008) with cataclasite bands that represent areas of locally higher shear strain and multiple planes of slickensides which preserve individual slip surfaces.

Later in the eruptive phase, the gouge layer thinned from 1-3 m to <3 cm, with the whole shear zone encompassing less than 10 cm from the spine surface. Thinning in shear zone thickness is indicative of slip-weakening behaviour (Ida, 1972; Mikumo et al., 2003; Otsuki et al., 2003; Palmer and Rice, 1973) and could have locally increased strain and strain rate along the conduit margin (Smith et al., 2011) promoting further thinning of the fault zone in a positive feedback cycle. Continued strain localisation would result in evolution of fault zone characteristics from the metre-scale unconsolidated gouge layer with cataclasite bands seen early in the eruption to the more compact shear-zone described here.

The crosscutting relationship of L1 over L2 indicates that, if gouge forms at 0.5-1 km depth (Cashman et al., 2008; Kennedy and Russell, 2011; Kennedy et al., 2009), as inferred from "drumbeat" source locations (Thelen et al., 2008), then L2 must have a source deeper than 1 km. Kennedy et al. (2009) infer strain rates of approximately $5 \times 10^{-2}\,\mathrm{s}^{-1}$ to $5 \times 10^{-1}\,\mathrm{s}^{-1}$ for slip events of ~5 mm to form the gouge during the early part of the eruption. The assertion of Kennedy et al. (2009) that there was no microstructural evidence for significant high-temperature, solid-state crystal plasticity during early spine growth coupled to the observation that spine morphology evolved from whale-back to more dome-like endogenous growth for spine 7 (Vallance et al., 2008) confirms an evolution in eruption dynamics.

Late-stage deformation of high-temperature silicic magmas is beleaguered by concomitant brittle and ductile to plastic features (Lavallée et al., 2008; Tuffen et al., 2008); with the transition from ductile to brittle behaviour varying according to temperature, porosity, crystallinity and strain rate (Dingwell, 1996; Lavallée et al., 2007; Webb and Dingwell, 1990). The observed characteristics of L2 require that formation temperatures must have been above the melting point of some mineral phases. As temperatures are well constrained to 600 ºC on the carapace of the extruding spine (Scott et al., 2008) and 730 ºC internally (Vallance et al., 2008), the occurrence of higher temperatures could be easily achieved via the conversion of frictional work along the conduit margin to heat (Bizzarri, 2011; Hirose and Shimamoto, 2005;

Nielsen et al., 2010). Momentary increase in strain rate and total slip along the conduit margin could produce sufficient shear heating (Rice, 2006) to induce melting and create pseudotachylyte, our interpretation of L2.

We note from the seismic record at Mount St. Helens that the extrusion of spine 7 was accompanied by two important, LP, hybrid seismic events which we suggest could have promoted the occurrence of frictional melting. These are a magnitude 3.6 earthquake which occurred at 6.15 am (GMT) on 5th August and a magnitude 3.3 earthquake at 1.01 pm (GMT) on 8th August 2006. Similarities to the "drumbeats" indicate that these larger events could represent a larger total slip along the same slip surface (Iverson et al., 2006). The source locations of these events are both at ~1 km depth, where the ambient temperature was likely >860 ^{o}C (Rutherford, 2008), and the extruding spine would have been fully crystalline (Cashman et al., 2008). Time-lapse videos from the USGS display that the ascent of a portion of spine 7 stalled for up to ca. 1 day prior to each event, and subsequently resumed extrusion as usual. This pause in extrusion and "drumbeat" occurrence would allow the ascending spine to accumulate enough stress to produce a larger seismic event.

Using the empirical relationship of magnitude to seismic moment defined by:

$$\log M_o = 1.5 \, M_s + 16.1 \tag{Eq. 8}$$

where M_o is seismic moment and M_s is magnitude (Purcaru and Berckhemer, 1978). We calculate moment magnitudes of 3.16e+14 and 1.12e+14 Nm for the magnitude 3.6 and 3.3 earthquakes respectively.

Since seismic moment is dependent upon rupture length and displacement, we may calculate the displacement of the event using the relationship:

$$M_o = \mu d L W \tag{Eq. 9}$$

where, d is the average slip, μ is the shear modulus, L is the rupture length, and W is the down-dip rupture width (modified from Biasi and Weldon (2006), Hanks and Kanamori (1979) and Scholz (2002)). The shear modulus is taken here as 3.24e+10 Pa (Alidibirov et al., 1997) from the previous eruption of Mount St. Helens, which produced compositionally and mechanically

similar dacite, and is in close agreement with the value of 3e+11 dyne cm^{-2} (3e+11 Pa) taken by Hanks and Kanamori (1979) for upper crustal settings. A rupture length of 98 – 190 m is used, based on the best-estimates of conduit circumference from Kennedy et al. (2009), while *W* is taken to be 1/3 of *L* based on small-scale rupture geometry. These calculations provide us with an upper and lower value for displacement during each of the events. For the magnitude 3.6 earthquake we find a maximum displacement of 3.05 m for a rupture length of 98 m and a minimum displacement of 0.81 m for a rupture length of 190 m. For the magnitude 3.3 earthquake we find that maximum slip is 1.08 m for rupture length 98 m, and minimum slip is 0.29 m for rupture length 190 m. The displacement and fault length relationship is consistent with the catalogue of displacement versus rupture length compiled by Schlische et al. (1996) over several orders of magnitude.

Once slip amount is known we can use the relationship of Cardwell et al. (1978) to relate a fault of finite thickness (applicable to widths >1 cm), with a known displacement, to the temperature increase caused by such an event:

$$T_m - T_o = \frac{\sigma_f D}{\rho C_p w}.$$

(Eq. 10)

where T_m is the temperature achieved, T_o is the starting temperature, σ_f is pressure, D is displacement, ρ is density, Cp is specific heat capacity and *w* is the thickness of the fault. Using a starting temperature of 860 °C, density of 2.8 kgm^{-3}, C_p of 1.25 J (g* K)$^{-1}$ and fault thickness of 3 cm, (assuming lithostatic pressure of approximately 30 MPa, corresponding to a depth below 1 km) and by varying displacement according to the values found above, we assess the increase in temperature resulting from the two LP seismic events according to slip on the entire conduit circumference. The maximum temperature increase during the magnitude 3.6 event is 871 °C and minimum is 231 °C, while for the magnitude 3.3 event the maximum and minimum values are 309 °C and 82 °C respectively. The minimum temperature increases are based upon slip around the full circumference of the largest possible estimated conduit (*e.g.* Kennedy et al., 2009). Slip over a shorter strike length, representing only a portion of the conduit surface, would result in a greater temperature increase (approaching our calculated maximum).

As experimental studies estimate frictional melting of igneous rocks at temperatures above 1100 °C (Lin and Shimamoto, 1998) and given the high ambient temperature in the volcanic conduit, the calculated temperature increases from both events would have been sufficient to

induce at least partial melting of the crystal assemblage to form a pseudotachylyte. Based on this calculation, microstructural, mineralogical and rheological evidence and the alteration reduction in TM10 within L2, we expect that frictional heating to at least 1100 ^{o}C occurred at depths >1 km. Subsequently, during ascent, the plug margin was subjected to further frictional processes which resulted in plastic deformation in the higher-temperature zone of frictional melt and which then resumed gouge formation after cooling, re-crystallising and entering the brittle regime in the upper ~1 km of the conduit.

4.5. Conclusions

During the 2004-2008 eruption of Mount St. Helens, a spatial and temporal differentiation of mechanical behaviour took place during spine extrusion, as evidenced by the progression of spine surface characteristics, which represent an evolution of conduit margin dynamics. Field observations, porosity and density measurements, geochemical, mineralogical, and microstructural studies, crystal size and shape distribution, kinetic properties and magnetic analyses were used to distinguish deformation regimes acting on the extrusion of Spine 7. We identify four structural layers, two of which had strong rheological control on the extrusion of the spine; L2 evidencing melting by friction and L1, a gouge layer. We infer that the gouge layer, which has been interpreted as the physical manifestation of microseismic "drumbeats" (Kennedy and Russell, 2011; Kennedy et al., 2009), thinned throughout the eruption and was contemporaneous with the slowing of extrusion rate and reduction in "drumbeat" recurrence.

The fault gouge truncates a previously undocumented rock unit, showing evidence of plastic deformation (L2). Grain size, circularity, remanence magnetisation, variable Curie Temperatures and the identification of a glass transition and a lower melting point by DSC suggest that this particular unit underwent a phase of heating and melting after initial crystallisation during magma ascent. We attribute this to extreme frictional processes at the spine surface at a depth below 1 km. We postulate that two larger LP seismic events, which had source mechanisms akin to the microseismic "drumbeats", represent larger (0.3-3.0 m) slip amount along the conduit margin. This displacement heated the rocks by up to 871 ^{o}C to over 1100 ^{o}C, which induced frictional melting to produce the pseudotachylyte. This layer remained above the melting temperature longer than typical pseudotachylytes, permitting near-equilibrium melting, due to high ambient temperatures. This facilitated slow re-crystallisation and localised plastic deformation during continued ascent, preventing the development of

signature pseudotachylyte characteristics. Further frictional processes, after re-crystallisation, led to gouge formation at depths above 1 km. This study explores the spatial variation in deformation mechanisms that regulate lava spine extrusion.

Alone in the clouds all blue.
Lying on an eiderdown.
Yippee!
You can't see me, but I can you.

Lazing in the foggy dew.
Sitting on a unicorn.
No fear!
You can't hear me, but I can you.

- Flaming, Pink Floyd

Chapter 5

Pseudotachylyte formation in volcanic conduits; signature features from Soufrière Hills volcano, Montserrat.

Lava dome eruptions subjected to high extrusion rates commonly evolve from endogenous to exogenous growth and limits to their structural stability hold catastrophic potential as explosive eruption triggers (Voight and Elsworth, 2000). The endogenous to exogenous shift in eruptive activity reflects strain localisation in magma (Hale and Muhlhaus, 2007; Hale and Wadge, 2008) accompanied by the seismogenic failure (Lavallée et al., 2013) which marks the onset of brittle magma ascent dynamics (Cashman et al., 2008). The rock record of exogenous dome structure preserves vestiges of cataclastic processes (Kennedy et al., 2009) and of thermal anomalies (Chapter 4)– both phenomena which are similarly at work in tectonic fault zones (Lin, 1996). The 2010 eruption of the Soufrière Hills (SHV), Montserrat is an example of such a regime shift. Here, a combined structural, thermal and magnetic investigation of a vein crosscutting a large block erupted in 2010 at Soufrière Hills reveals evidence of faulting and frictional melting within the magmatic column. The mineralogy of this pseudotachylyte vein offers evidence of complete recrystallisation with an isothermal remanent magnetisation signature that typifies local electric currents in faults (Ferré et al., 2005). Recrystallisation ultimately decreased the porosity of the vein; yet, the presence of cristobalite in the host rock suggests a formerly permeable damage zone in this region of strain localisation. We conclude that frictional melting plays a significant rheological control on lava dome eruptions.

5.1. Introduction

Dome-building eruptions have the potential for volcanic catastrophes, with dome collapse leading to devastating pyroclastic flows with almost no warning (Carn et al., 2004; Herd et al., 2005; Voight and Elsworth, 2000). During dome growth, the driving forces of the buoyant magma may be superseded by controls along conduit margins; where brittle fracture and sliding can lead to formation of lubricating cataclasite and gouge (Cashman et al., 2008; Kennedy et al., 2009). Extrusion of high-viscosity magma at arc volcanoes is frequently accompanied by seismic activity in the form of repetitive "drumbeat", long-period (LP) events (Iverson, 2005). At SHV this seismicity has been attributed to cyclic plug extrusion governed by magma supply rate, conduit geometry (Rowe et al., 2004), overpressure build-up (Edmonds and Herd, 2007) and rheological stiffening (Voight et al., 1999) ultimately resulting in stick-slip behaviour. Frequent transitions from explosive to effusive behaviour at SHV may have been governed by formation of localised shear zones formed in viscous andesitic magma (Carn et al., 2004; Watts et al., 2002). Fracturing and increased damage in these shear zones could build up the permeable networks that enable degassing, and as such, the critical overpressure required for explosive eruption would not be met n(Edmonds and Herd, 2007). Hence, shear fracturing of ascending magma is of critical importance to the explosivity of volcanic eruptions (Castro et al., 2012; Okumura et al., 2010; Tuffen et al., 2003).

5.2. Methods

5.2.1. Thermal measurements

Thermogravimetric measurements (TG) and low sensitivity scanning calorimetry (LS-DSC) were carried out using a Netzsch STA 449 C simultaneous thermal analysis equipment. Small chips of about 50 mg were heated in a Pt crucible (with lid) with a heating rate of 10 K/min up to 1500 °C in air. High sensitivity scanning calorimetry measurements (HS-DSC) were carried out using a Netzsch DSC 404 C. Small chips of about 25 mg were heated in a Pt crucible (with lid) with a heating rate of 10 K/min up to 1000 °C in air, cooled with 10K/min to 100 °C and than reheated to 1000 °C.

5.2.2. Magnetic measurements

Rock magnetic measurements were made on the Variable Field Translation Balance by *Petersen Instruments* at the University of Liverpool. Remanence carriers defined as low coercive materials (saturation of an isothermal remanence, IRM, below 200 mT). A second experiment used alternating field demagnetisation of different remanent magnetisations. This experiment was run in a magnetically shielded room at LMU Munich, using the SushiBar, an automated system for paleomagnetic investigations (Wack and Gilder, 2012). First, the natural remanence NRM was measured and then demagnetised using 14 steps of increasingly higher alternating fields. Then an anhysteretic remanent magnetisation (ARM) was implied. An ARM is produced by the combination of a slowly decaying alternating field and a steady unidirectional field. For the ARM a maximum field of 90 mT was applied. This ARM was measured and then demagnetised in the same manner as the NRM. Finally an IRM using a 1.2 T magnetic field was implied, measured and again stepwise demagnetised.

5.2.3. Scanning electron microprobe

Uncovered thin sections of each sample were carbon coated for analysis in a CAMECA SX100 scanning electron microprobe. Backscatter electron (BSE) images highlight grain-size and density differences. Specific minerals within the samples were analysed using wavelength dispersive analysis (WDA) to verify the mineralogy identified by optical analysis. Additionally, an element map was made for a cross-sectional area across the host rock to pseudotachylyte boundary to identify the different mineral distribution.

5.2.4. Tomography

3D high-resolution tomography images were acquired through v/tome/x s 240 micro-CT scanner from GE phoenix using a high-power X-ray tube and a drx-250 rt detector system (experimental conditions: Pixel / Voxel size: 30.0 μm, 1000 images for 360° (average of 3 single images, one image skipped), exposure time of 1 s, voltage of 80 kV and current of 250 μA and Cu-filter with 0.3 mm thickness).

5.3. Frictional melting in the conduit

Meter-scale blocks from block-and-ash flow deposits at SHV facilitate the study of textural and structural information from the pre-existing conduit and dome that would otherwise remain practically inaccessible due to the threat posed by the current unrest. Of specific interest is a vein located in an andesitic block erupted in 2010 due to its morphology, vitreous appearance and lateral extent. Its location, which traverses its host rock, confirms its origin in the magmatic column. The shear band consists of interlayered aphanitic pseudotachylyte and granular cataclasite up to 2cm thick which pinches out, widens and bends along its ~1m length (Figure 5-1, Figure 5-2) demonstrating post-formation ductile deformation in the still-flowing, conduit-dwelling, viscous magma.

Figure 5-1. Field photo of the shear band. Aphanitic pseudotachylyte layers of the shear band are interspersed with cataclastic layers. Photograph illustrates the lateral variation in thickness and its morphology, which suggests formation in viscous magma in the conduit.

The host rock, a porphyritic andesite, has a crystalline assemblage of plagioclase, amphibole and orthopyroxene phenocrysts, with some quartz grains and FeTi oxide (total crystallinity <60 %) set in a groundmass of clinopyroxene, orthopyroxene and plagioclase (Figure 5-2). Amphiboles are broken down into pseudomorphs containing plagioclase, pyroxene and abundant FeTi oxides as has been reported from earlier in the eruption (Zellmer et al., 2003). These result from dehydration reactions of amphibole during ascent, or from long repose intervals in the conduit, as well as from late-stage oxidation to form opacite (Garcia and Jacobson, 1979; Murphy et al., 2000), which is common in this sample. What interstitial glass may have existed is fully devitrified; indicating a relatively low extrusion rate (Baxter et al., 1999). Glass has been replaced by silica residue, predominantly cristobalite, through high-temperature vapour-phase reactions along degassing pathways in the conduit (Baxter et al.,

1999; Horwell et al., 2010), which may have been aided by the permeable damage zone around the shear band, highlighting its importance on the evolution of the permeable porous network. In earlier stages of the eruption at SHV silica polymorphs, including cristobalite, have comprised up to 15 wt. %.
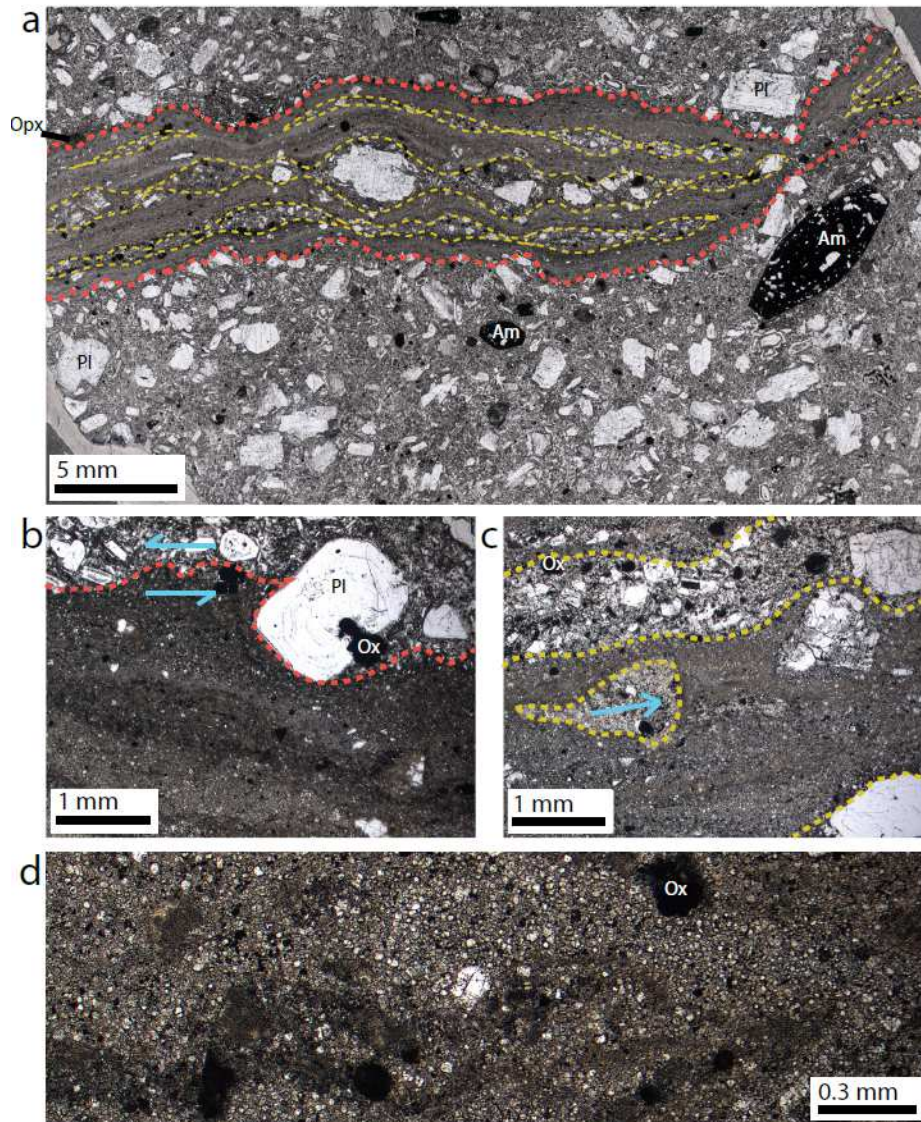
Figure 5-2. Photomicrographs of the shear band. (a) a wide view of pseudotachylyte (dark grey) and cataclasite (grey) layers in the shear band cutting through the andesite host rock, containing plagioclase (Pl), amphibole pseudomorphs (Am), orthopyroxene (Opx) and FeTi oxides (Ox). Morphology of the vein shows shear band pinching out and lenses of cataclasites between pseudotachylyte veins of more constant thickness. (b) inferred shear direction from flow morphology of the pseudotachylyte around a host-rock phenocryst at the vein boundary. (c) cataclastic lens hosted in a pseudotachylyte layer with bulbous onset and elongate tail indicating flow direction of the band. (d) internal structure in the pseudotachylyte-cataclasite

interface indicating turbulent flow. Red dashed lines mark the boundary of the shear band, yellow dashed lines show boundaries between pseudotachylyte and cataclasites, arrows represent inferred flow / shear directions.

The presence of cristobalite here was verified using differential scanning calorimetry (DSC) (Figure 5-3). High sensitivity (HS)-DSC measurements on the host rock groundmass revealed an endothermic peak at 190°C, which recurred after cooling and reheating, indicating a phase transition. While the ideal α-β phase transition of cristobalite occurs at 272 °C, highly distorted crystals originating from a gel or glass can have a lower transition temperature, and inversion temperatures of 120-272 °C have been recorded (Sosman, 1965).
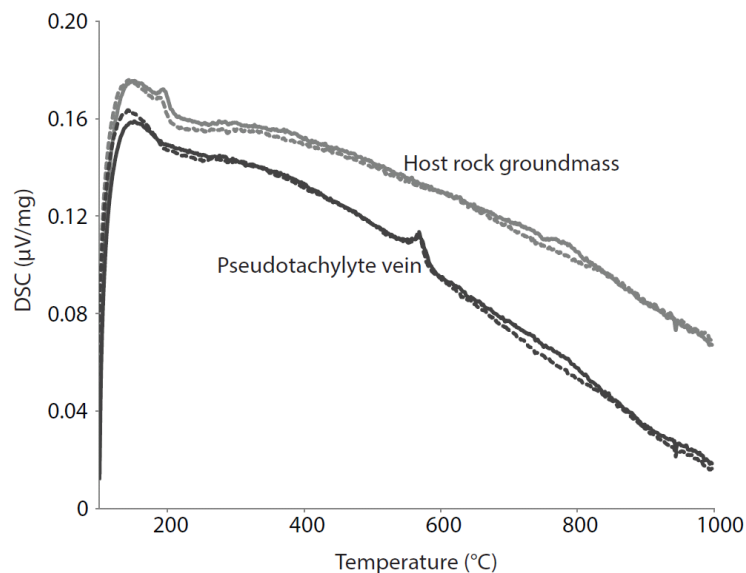
Figure 5-3. High sensitivity scanning calorimetry measurements (HS-DSC). Measurements were carried out using a Netzsch DSC 404 C. A sharp endothermic peak at about 190 °C in the host rock (grey trace) corresponds to a critobalite α-β phase transition and the trace shows no evidence of a potential glassy phase. An endothermic peak at about 570 °C corresponding to the α-β phase transition in quartz is seen in the pseudotachylyte vein (black). The same exothermic peaks are visible on the second run (dashed lines) of the experiments with the same sample confirming their respective phase transitions.

The shear band reveals no such endothermic peak as a result of cristobalite, however, a repeatable endothermic peak at 572 °C (Figure 5-3) can be attributed to the α-β phase transition of quartz (Sosman, 1965). The melting temperature of the shear zone also differs from the host rock. Low sensitivity (LS)-DSC measurements on the groundmass of the host rock show two broad melting peaks between 1100°C-1250°C and 1350°C-1450°C (post optical analysis of

samples after runs to 1300 °C and 1500 °C indicate partial and complete melting of all phases respectively) whereas the aphanitic pseudotachylyte vein shows a broad melting peak between 1200°C-1400°C (post optical analysis indicates complete melting of all phases). This difference arises from a contrasting mineralogy (Figure 5-4), indicative of a different crystallisation history.
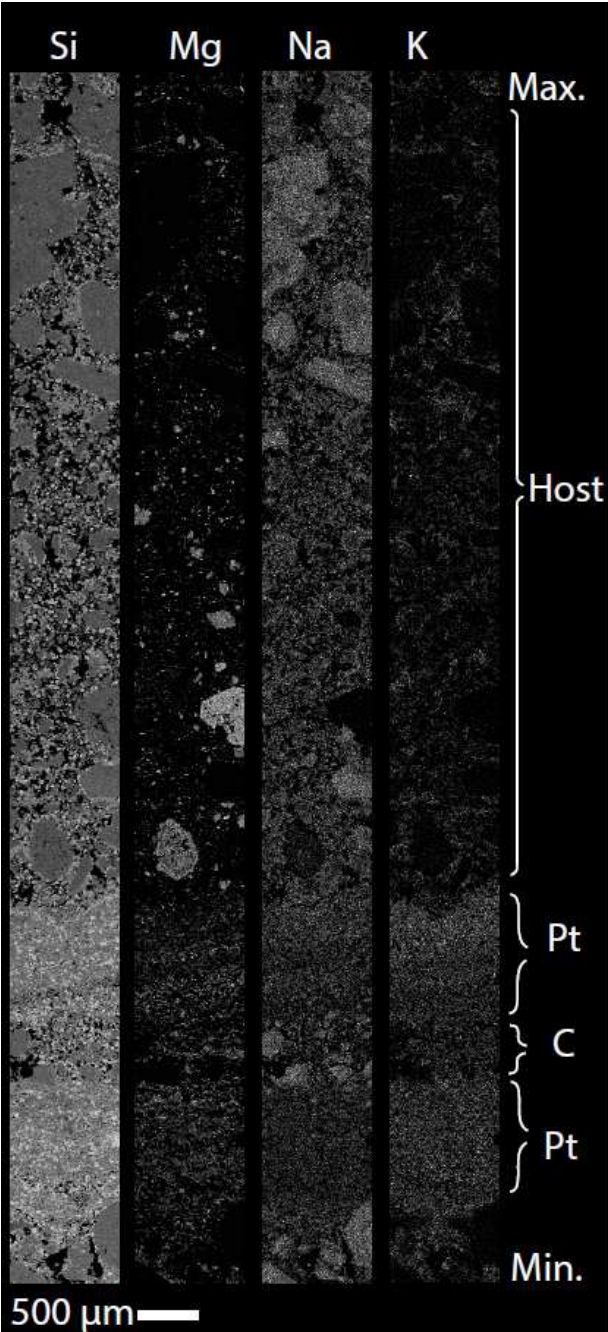
Figure 5-4. Element maps of the sample. The abundance of each element (silica, magnesium, sodium and potassium) across the mapped region (the brightest region of each individual image represents the peak occurrence of that element) including host rock, pseudotachylyte (Pt) and Cataclasite (C) bands.
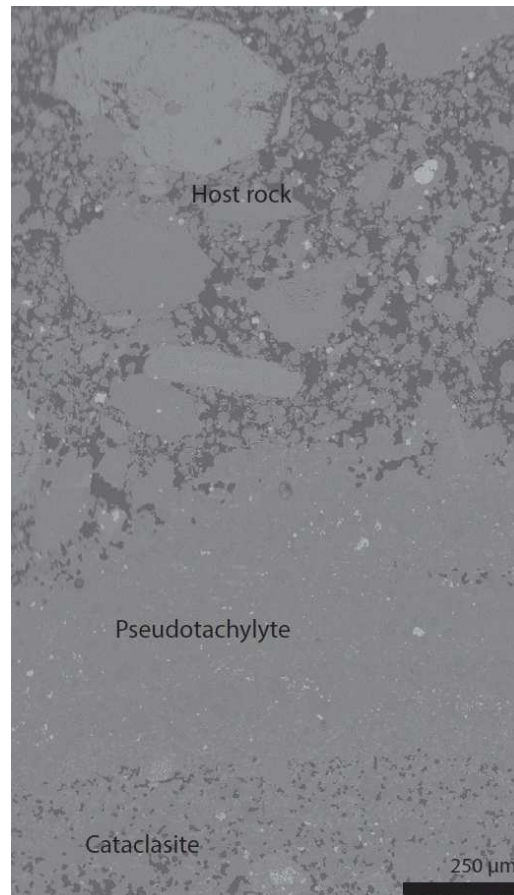
Figure 5-5. BSE Image of the sample. The backscattering coefficient varies according to the atomic weight, where heavier elements have a lower backscattering coefficient and are lighter in colour in BSE images. In the host rock the porosity is unevenly distributed and grain size varies from 10's to 100's of μm. The pseudotachylyte is significantly denser, and has a very fine grained (< 40 μm) texture. The cataclasite in this region has intermediate density and grain size. There are more FeTi oxides ([white, Figure 1] which are the magnetic carriers) in the pseudotachylyte than in the host rock, but they are smaller, and there seems to be a tendency for higher Ti content in the magnetic carriers in the vein (5:1 rather than 10:1 Fe:Ti).

The pseudotachylyte consists of fine grained (10-40 µm), equant and well sorted quartz, FeTi oxides and cordierite, in contrast to the host rock groundmass. The cataclasite layers in between have the same mineralogy as the host rock as they are granular aggregates and contain grains up to several mm in diameter, although more typically 20-400 µm (Figure 5-2). The drastic contrast in mineralogical assemblage (Figure 5-4) and petrographic texture (Figures 5-5 and 5-6) suggest that the vein formed due to complete melting of the host rock during faulting and frictional slip of the viscous magma in an area of strain localisation near the conduit margin. The metastable melt was then able to crystallise slowly due to the high volcanic geotherm,

118

forming the pseudotachylyte. The fine-grained, equant nature of the crystals formed during the slow crystallisation (Figure 5-6) accounts for the very low porosity of the pseudotachylyte layers (1%) as compared to the cataclastic layers in the shear band (15%) or the host rock (23%)(see Figure 5-7).
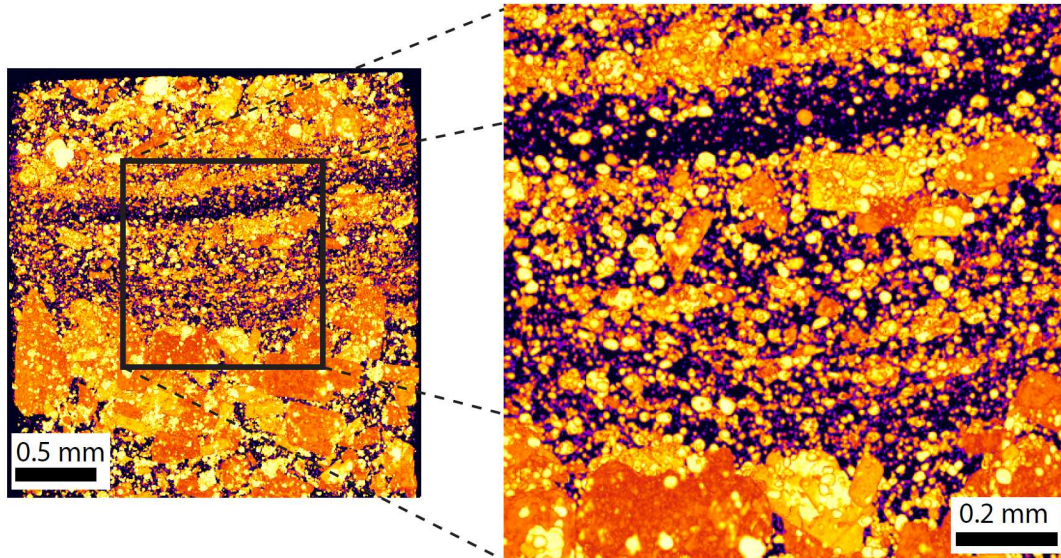
Figure 5-6. Stacked image of crystals in 3D. All crystals in the sample, at a voxel size of 30μm flattened into a slice. The figure shows heavier elements in brighter colours, and clearly illustrates the very fine grained nature of the pseudotachylyte vein (majority of crystals below detection-size).
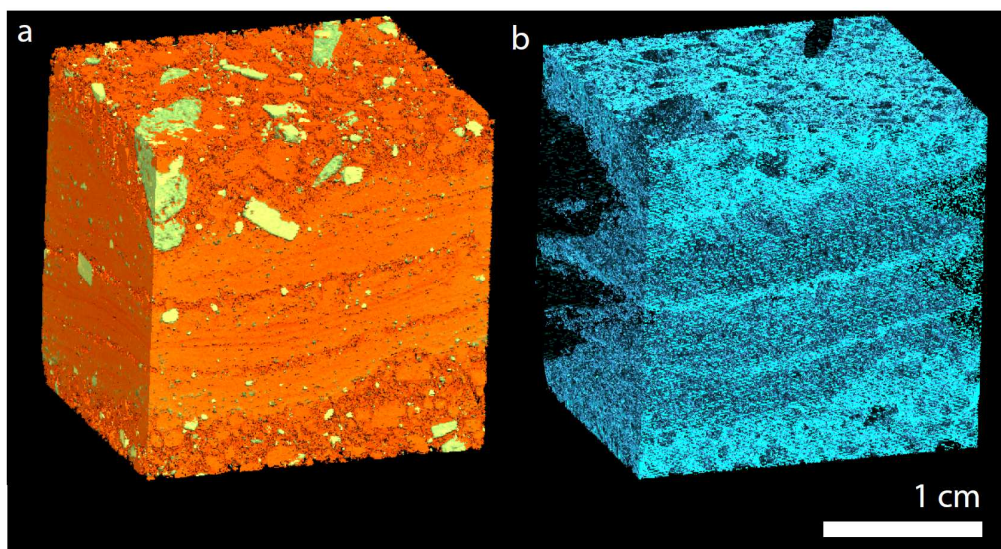
Figure 5-7. Tomography of the shear band in the host rock. (a) 3D representation of the solid fraction of the sample is shown in yellow (oxides and pyroxenes) and orange (plagioclase and groundmass) according to density. (b) 3D pore space in blue, highlighting the negligible porosity of the pseudotachylyte layers.

Crystallisation in this volcanic pseudotachylyte vein recorded a distinct magnetic signature characteristic of classic, tectonic pseudotachylyte, which confirms its status as a frictionally generated melt. The remanence of the pseudotachylyte is carried by a low coercive material with a Curie temperature (T_c) of 320 °C, whereas the host rock, which also shows low coercive behaviour, has two Curie temperatures at 400 and 540 °C. Alternating field demagnetisation of different remanent magnetisations was used to identify further differences between the two samples (Figure 5-8).
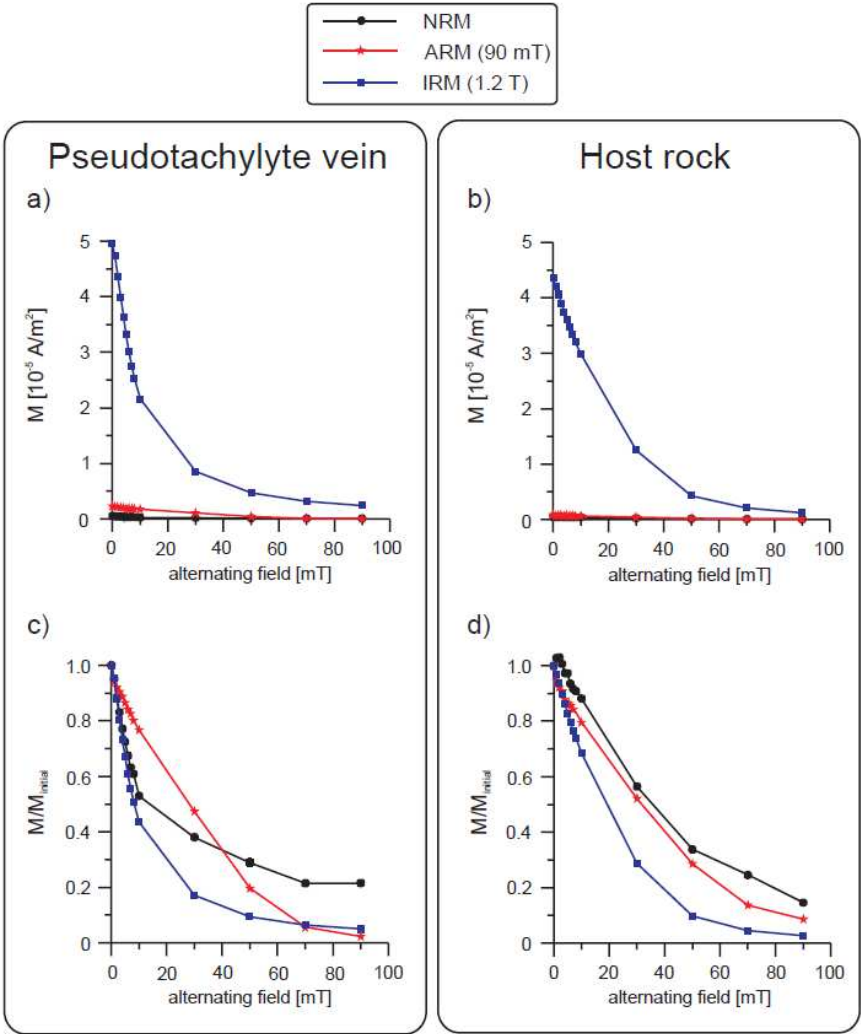
Figure 5-8. Rock magnetic measurements. Alternating field demagnetisations of NRM, ARM and IRM of pseudotachylyte and host rock. (a) and (b) First magnetisation versus alternating field for pseudotachylyte and host rock respectively, (c) and (d), normalised magnetisation (normalisation using initial magnetisation at 0 mT alternating field) versus alternating field. NRM of the pseudotachylyte is analogue to an IRM while the NRM of the host rock is analogue to an ARM.

The remanence of the pseudotachylyte is comparable to an isothermal remanent magnetisation, whereas the remanence of host rock displays similarities to an anhysteretic remanent magnetisation as expected for a thermal origin. Thus, the pseudotachylyte has seen a strong magnetic field that overwrote the previous thermoremanent magnetisation of the magma. Due to the close proximity of the two samples (within 2 cm) this IRM cannot originate from a lightning strike (known to enforce magnetisation) but instead demonstrates its frictional melt origin, as strong local electric currents occurring in a fault give rise to a strong isothermal remanent magnetisation (Ferré et al., 2005; Freund et al., 2007). Indeed, the demagnetisation experiments performed provide some of the clearest evidence to distinguish between pseudotachylyte and host rock (Ferré et al., 2005; Freund et al., 2007).

5.4. Conclusions

This study documents unequivocal evidence of frictional melting, in still-viscous, conduit-dwelling magma. Pseudotachylyte has previously been linked to seismogenic ruptures (Magloughlin and Spray, 1992), at slip velocities over 0.1 m/s (Spray, 2010). The formation of pseudotachylyte at the SHV may be linked to repetitive "drumbeat" seismicity recorded throughout the eruption (Rowe et al., 2004; Watts et al., 2002), and which has been linked to magma failure and stick-slip events along conduit margins (Iverson, 2005). Slip events on the order of 10^{-2} m/s(Costa et al., 2012) should be sufficient to create frictional melt (Lavallée et al., 2012). The formation of shear bands may have important implications for eruption dynamics (Hale and Muhlhaus, 2007; Hale and Wadge, 2008), and if pseudotachylyte is formed, these consequences may differ significantly from those anticipated from gouge-hosting (Cashman et al., 2008; Kennedy et al., 2009) shear zones because the frictional properties of melt differ greatly from gouge (Magloughlin and Spray, 1992; Spray, 2010). Additionally the development of the permeable porous network is dependent upon shear band formation (Okumura et al., 2010). Evidence here suggests that the shear zone was involved in active degassing, which has proven vital in explosive-effusive transitions (Castro et al., 2012; Edmonds and Herd, 2007) and hence further work is required to establish the consequence of frictional melting in the conduit during eruptions of highly viscous magma.

“Don't build your world around volcanoes melt you down…”

-Damien Rice

Chapter 6

Viscous brake and stick-slip in volcanic conduits

The extrusion of highly viscous magma during dome-building eruptions is frequently accompanied by "drumbeat" seismicity (Iverson et al., 2006). This is simultaneous to the formation of shear zones and movement along slip surfaces at conduit margins, which generate fault products akin to those formed in tectonic settings, including gouge, cataclasite (Kennedy et al., 2009) and pseudotachylyte . The repetitive-source nature of "drumbeat" families has been attributed to stick-slip motion at fixed loci within the conduit (Costa et al., 2012; Neuberg et al., 2006). However, the cause of said stick-slip motion remains elusive. Here, we demonstrate that the occurrence of frictional melting can explain the self-regulating, cyclic progression of stick-slip motion during viscous magma ascent via the production of a viscous melt brake. High-velocity rotary shear (HVR) experiments indicate that frictional melting may be an inevitable consequence of slip, resulting in higher shear resistance than rock-rock sliding. Variable-rate experiments, which mimic rapid velocity fluctuations in stick-slip behaviour, pertain to the velocity-weakening behaviour of melt, with a tendency for unstable slip. This establishes that the control of magma transport is passed from buoyant forces at depth to viscous slip zone properties during ascent, with the repetitive nature of "drumbeats" accounted for by the arrival of fresh magma at this mechanical transition zone. The link between frictional melting and stick-slip motion is applicable to many active volcanoes worldwide and has wide-reaching implications for models of volcanic unrest. We anticipate that this advance will reshape our description of dome-building eruptions.

6.1.Introduction

Dome-building eruptions are frequently accompanied by seismic activity, and specifically the repetitive occurrence of long period (LP) seismic events termed "drumbeats". Families of events with fixed source locations indicate a recurrent scenario, which has been modelled as either resonance of a gas-filled crack (Chouet, 1988), or more commonly accepted as magma fracture and stick-slip at the conduit margin (Costa et al., 2012; Iverson et al., 2006; Lensky et al., 2008; Neuberg et al., 2006). The high temperature fracture of magma has been shown to be seismogenic (Lavallée et al., 2008; Tuffen et al., 2008) and conditions which permit failure are relatively well studied (Lavallée et al., 2013). However, little is known about the frictional properties of magma likely at play during ascent beyond the point of failure. Exogenic dome growth has evidenced the development of cataclastic gouge zones (Cashman et al., 2008; Kennedy et al., 2009) as well as pseudotachylyte, but their mechanical contribution to eruptive behaviour remains unconstrained.

The frictional properties of rocks are generally described in terms of and rate- and state- friction (Abe et al., 2002; Dieterich and Kilgore, 1994; Ruina, 1983). Fault strength and frictional properties of rock show a complex dependence upon slip and slip-velocity (Hirose and Shimamoto, 2005; Sibson, 1977). The mechanical work involved with slip generates heat, which can lead to flash heating (Rice, 2006) and frictional melting (Del Gaudio et al., 2009; Di Toro et al., 2006; Fialko and Khazan, 2005; Hirose and Shimamoto, 2005; Magloughlin and Spray, 1992). It is generally conceived that frictional melting will ensue from a slip rate exceeding 0.1 m/s (Rice, 2006; Spray, 2010)– a rate commonly achieved by the exogenic growth of lava domes (Costa et al., 2012; Hale and Wadge, 2008). Melting may act as a lubricant or a brake (Di Toro et al., 2006) and result in unstable slip (Fialko and Khazan, 2005), which is amongst the requirements for stick-slip motion (Dieterich, 1979; Swanson, 1992). Here we present evidence that frictional melting and the formation of pseudotachylyte is a common product of high-viscosity magma ascent, and could be the cause of stick-slip motion and associated repetitive, "drumbeat" seismicity.

6.2. Method

HVR experiments (Shimamoto and Tsutsumi, 1994) were conducted under atmospheric conditions. 2 hollow cylindrical cores of 24.98mm (inner diameter of 9.2-9.5mm) were fixed into the apparatus, and one sample was rotated at up to 1500 rpm (max. 1.5 m/s for our samples) at a set axial load of up to 10 MPa. Slip distance varies from the axis of rotation, and hence an equivalent slip velocity is defined (Hirose and Shimamoto, 2005). Axial force, shortening and torque are measured at a sampling rate of 200 kHz, and shear stress calculated as a function of displacement. Experimental runs were recorded with a thermal camera to monitor thermal production associated with friction.

6.3. Stick slip motion and the viscous brake

High-velocity rotary shear experiments demonstrate the propensity for melting of the andesitic and dacitic material (from Soufrière Hills volcano (SHV) and Mount St. Helens (MSH) respectively) at upper conduit stress conditions. Starting from room temperature, frictional melting of the magmas can occur in less than 1 m slip at 1 m/s (Figure 6-1). The slip distance at which melting occurs is drastically decreased (~18 to ~1 m) by increasing the normal stress (1 to 10 MPa) or moderately decreased by increasing the slip velocity. We note that even from room temperature, enough heat is generated to induce frictional melting at as little as 0.1 m/s (Figure 6-1) – a rate commonly achieved during magma ascent (Costa et al., 2012).
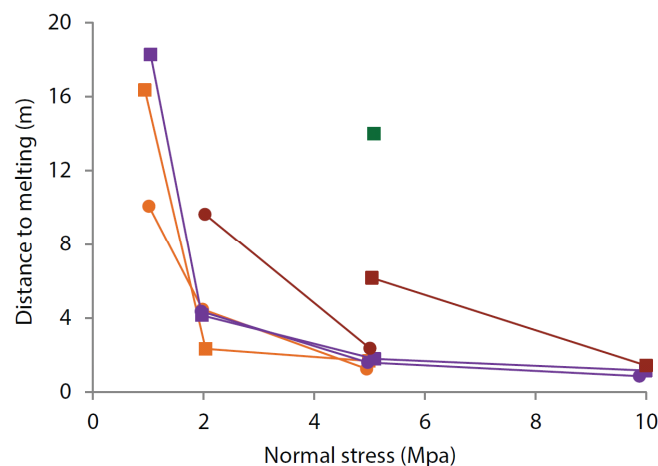
Figure 6-1. Efficiency of melting. Slip distance at which melting occurs dependent upon normal stress and slip velocity of 0.1, 0.4, 1.0 and 1.5 m/s (green, red, purple and orange respectively) for Mount St. Helens (squares) and Soufrière Hills (circles). The dataset

demonstrates that melting is favoured at higher normal stress, at higher velocity and in Soufrière Hills andesite. Sample melting occurs as early as ~0.85 m slip at 1m/s and 10 MPa.

At the onset of rock-rock friction comminution produces gouge and results in an early shear stress peak, followed by slip weakening and stabilisation (Figure 6-2a). A second peak emerges as discrete melt patches form along the contact until a peak shear stress is attained as a complete molten layer forms (see Supplementary video 1). This is followed by further slip weakening, as the melt zone thickens and attains steady state viscosity-controlled sliding (Figure 6-2a). The shear stress (τ) of rock-rock friction increases with normal stress (σ_n):

$$\tau = \mu\sigma_n \tag{Eq.11}$$

where the friction coefficient μ ranges between 0.6 and 0.85, according to Byerlee's rule(Byerlee, 1978) (Figure 6-2b). The rate-effect for rock-rock friction is negligible, tending toward velocity weakening, across the range measured (Figure 6-2b). During slip the friction coefficient decreases (Figure 6-2a) in agreement with other high-velocity friction studies on igneous rocks (Del Gaudio et al., 2009; Di Toro et al., 2006).

Upon melting, the shear resistance increases drastically (figure 6-3a) with shear-to-normal stress ratio as high as 1.8 for the peak stress regime and 1.3 for steady state regime (Figure 6-2c). At higher normal stress the ratio rapidly falls below the anticipated range. While it may be misleading to describe the relationship of shear to normal stress as a friction coefficient (Di Toro et al., 2006), a dependence is still noted. Additionally, melt is velocity weakening (Figure 6-2c) due to shear thinning.
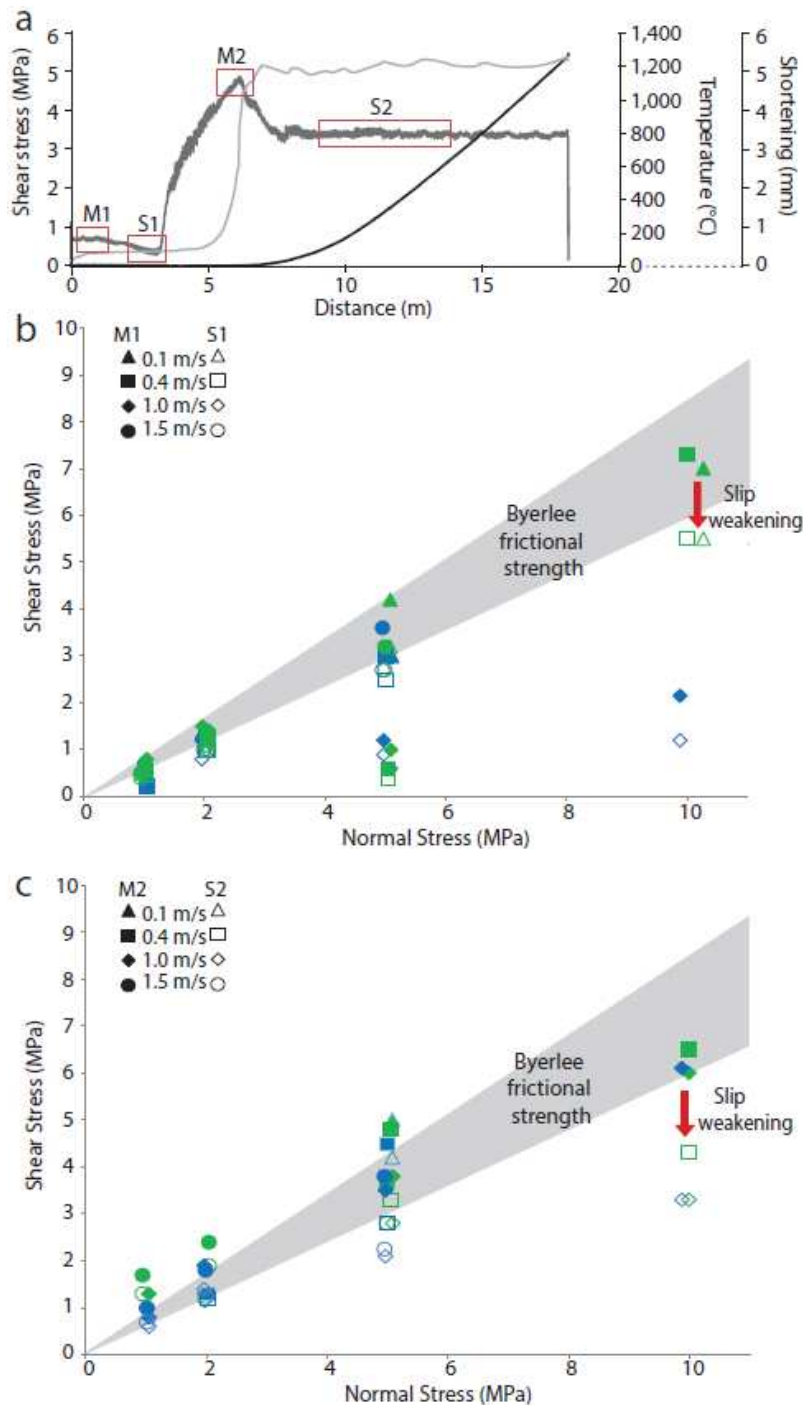
Figure 6-2. Frictional behaviour of magma. (a) Example of a HVR run with shear stress (dark grey), shortening (black) and temperature (light grey) over slip distance. Rock-rock maximum (M1) and steady state (S1) shear stress and melt maximum (M2) and steady state (M2) shear stress are highlighted for use in subsequent plots. The corresponding thermal video S1 shows the heating rate. (b) Cumulative plot of rock-rock normal versus shear stress for M1 and S1 and (c) Cumulative plot of melt normal versus shear stress for M2 and S2, both at 0.1, 0.4, 1.0 and 1.5 m/s for MSH (green) and SHV (blue) with Byerlee's rule (μ=0.6 to 0.85) in grey.
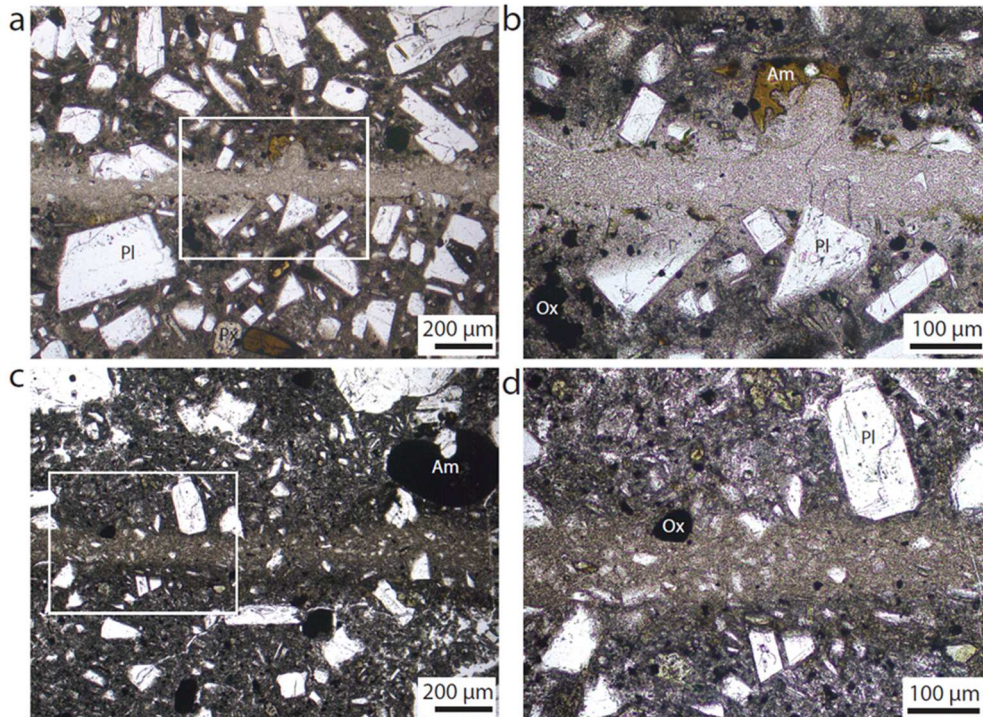
Figure 6-3. Photomicrographs of experimentally generated pseudotachylyte. From thin sections of samples deformed at 5MPa, 1 m/s for 20 m displacement (a) MSH dacite with a ~0.3 mm pseudotachylyte layer containing plagioclase crystal fragments. Melt cuts through host rock plagioclase and groundmass sharply but preferentially melts encountered amphiboles in the close-up image (b). (c) SHV andesite with a ~ 0.1 mm pseudotachylyte layer bounded by a ~ 0.1 mm zone of alteration where the host rock glass has surpassed the glass transition allowing local ductile deformation. More crystal fragments are seen in the pseudotachylyte than in (a) and preferential alignment of microphenocrysts is seen in the viscously remobilised zone in the close-up (d).

Under the same conditions, SHV showed faster melting and lower shear stress than MSH (Figures 6-1 and 6-2). This is controlled by the nature of the samples; the MSH sample is a dacite with plagioclase, amphibole, clinopyroxene, orthopyroxene and apatite phenocrysts, and FeTi oxides set in an aphantic groundmass of predominantly plagioclase and quartz and no interstitial glass whereas the SHV sample is a porphyritic andesite, with plagioclase and orthopyroxene phenocrysts, amphibole pseudomorphs and quartz, clinopyroxene, orthopyroxene and plagioclase microphenocrysts and FeTi oxides set in a rhyolitic interstitial glass (Figure 6-3). At a given temperature, the viscosity of a melt with bulk andesitic composition is lower than that of a dacitic composition (Giordano et al., 2008) and hence, as slip properties are controlled by the viscosity of the melt, frictional melt of the SHV sample preferentially favours slip over that of MSH. Additionally, the effect of interstitial glass, which

surpasses its glass transition temperature (T_g, ~ 700 °C) on the approach to melting, alter the frictional properties of the andesite (Lavallée et al., 2012). A zone visible either side of the pseudotachylyte layer in SHV (Figure 6-3c and d) indicates the area that exceeded T_g and suffered viscous deformation during slip (preferential crystal alignment) verifying the glass' influence.

Once the slip properties of the samples were established, a set of variable-rate experiments were used to mimic rapid velocity fluctuations in stick-slip behaviour (Figure 6-4). These experiments verify the tendency for velocity weakening behaviour and highlight an inclination for unstable slip. Experiment one (Figure 6-4a) demonstrates that once a steady state shear stress is achieved in melt, an instantaneous increase in shear stress results from rapidly decreasing velocity and a new stable shear stress is easily attained, additionally, the original steady shear stress is instantaneously re-instated when velocity is increased again; in agreement with shear thinning rheological behaviour of crystal-bearing melt(Lavallée et al., 2007). The shear stress will always maintain a steady state as long as the melt layer is maintained; so when velocity is decreased further, the shear stress increase overwhelms the structural relaxation of the high-viscosity melt produced by the MSH sample. Experiment two (Figure 6-4) sees MSH melting significantly later than SHV as slip rate is increased, then, as slip rate is decreased shear stress gradually increases due to shear thinning until MSH and then SHV fail when the temperature decreases and the viscosity becomes too high to structurally relax at the imposed slip rate. In experiment three the initial low-slip velocity (0.4 m/s) does not permit melting, instead steady state rock-rock friction is achieved, and the first high-velocity section (1.0 m/s) forms melt as well as a peak in shear stress. The first trough shows the velocity-weakening effect of the melt, and the following rapid fluctuations in slip velocity induce strong variations in shear stress, but frictional melt remains in the slip zone. Experiment four has a similar dynamic, the shorter high velocity portions and longer low velocity portions have little effect and a constant melt layer is maintained throughout. In cases where the base slip velocity is lowered (e.g., 0.2 m/s; experiments five and six), the frictional melt generated at high slip velocity struggles to remain liquid due to insufficient temperature generated by low slip velocity; this allows the less viscous SHV melt to persist, but brings the MSH melt to a viscous halt (failure in this case) after 3 and 7 cycles respectively, and in both cases shear stress achieves a higher and higher peak on subsequent low velocity cycles. For SHV the shortening is visibly stepped in experiments five and six as more melt is produced at the higher velocity.
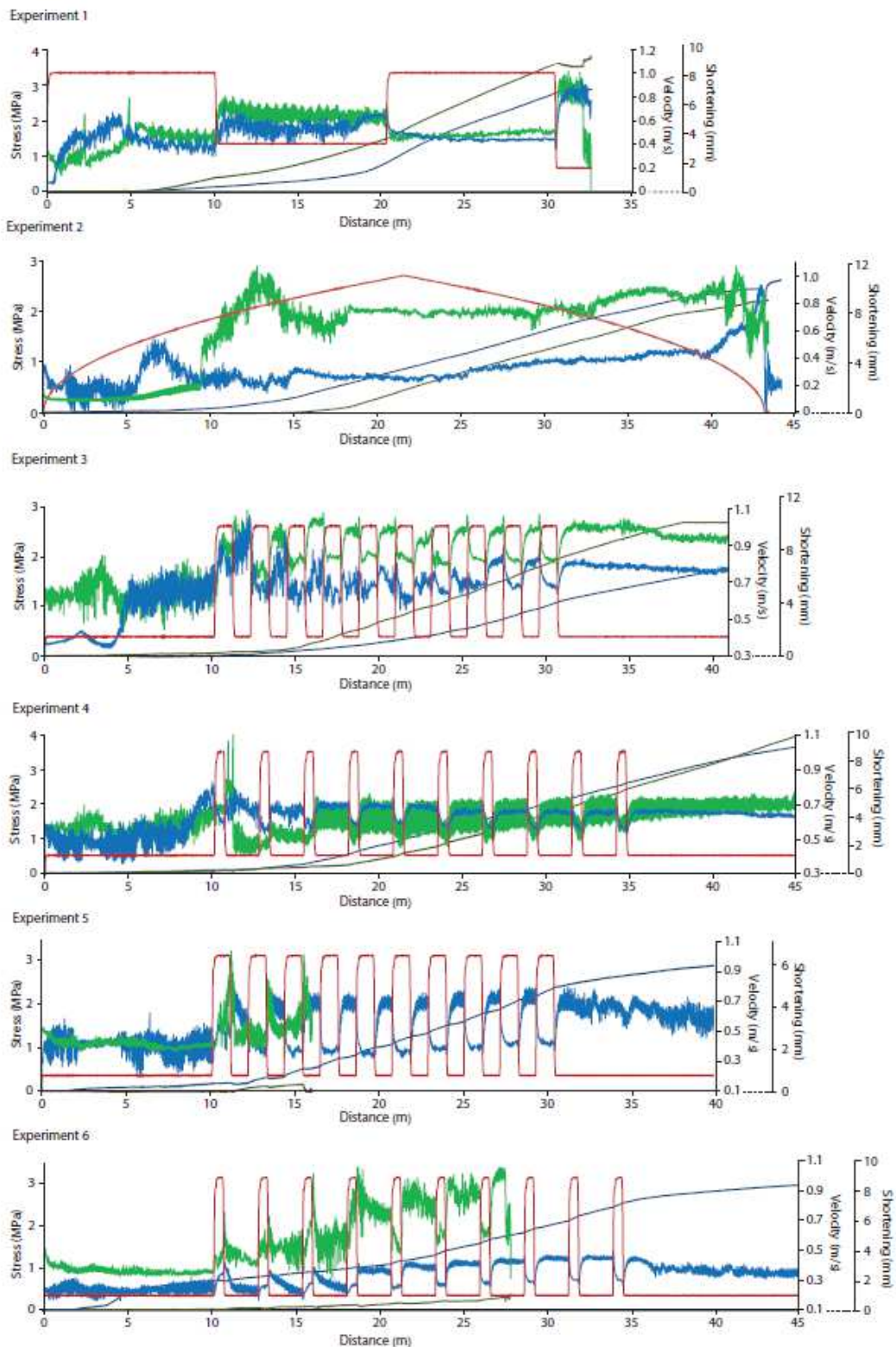
Figure 6-4. Variable rate, stick-slip HVR experiments. A set of 6 velocity profiles used to mimic extrusion rate variations and stick-slip behaviour in volcanic conduits. Slip rate (red) shows the imparted velocity, resultant shear stress (green and blue) and shortening (dark green and dark blue) for MSH and SHV respectively show the evolution of the melt layer over slip distance.

6.4. A model

The application of the viscous brake to magma ascent is as follows; when a failure and slip event forms a melt layer at the conduit margin the high velocity creates a lubricating effect and slip is maintained. As slip velocity wanes the apparent melt viscosity increases, causing an increase in shear resistance that acts as a viscous brake and halts slip (the "stick" of stick-slip motion) with a fault zone healed by the melt. Sufficient buoyancy-driven pressure from ascending magma below eventually overcomes resistance to produce another failure and rapid slip event (the "slip"). The fault zone is once again temporarily lubricated due to velocity-weakening, but new magma below experiences the same slip event more slowly as the magma decompresses (in a concertina effect), and as the velocity decreases the shear resistance increases to once again bring into effect the viscous brake. The fixed spatial locus of repetitive "drumbeats" and the occurrence of "families" of similar seismic events is accounted for by the arrival of fresh magma with constant rheological properties at a fixed source. While above, the frictional melt crystallises and continues its ascent along the conduit margin. This view is supported by field evidence in the form of pseudotachylytes identified in lava dome products at Mount St. Helens (Chapter 4) and Soufrière Hills (Chapter 5) volcanoes, both of which were characterised by repetitive, periodic, fixed-source seismicity and lava spine extrusion. The Pseudotachylyte was cross-cut by a gouge/cataclasite layer which formed later (i.e., at higher level) in the upper conduit. We conclude that stick-slip motion in volcanic conduits is a self-driven, frictional-melt-regulated force common to many dome-building volcanoes.

"There are three stages in scientific discovery.
First, people deny that it is true, then they deny that it is important;
finally they credit the wrong person."

- Bill Bryson, A Short History of Nearly Everything

Chapter 7

Conclusions and Outlook
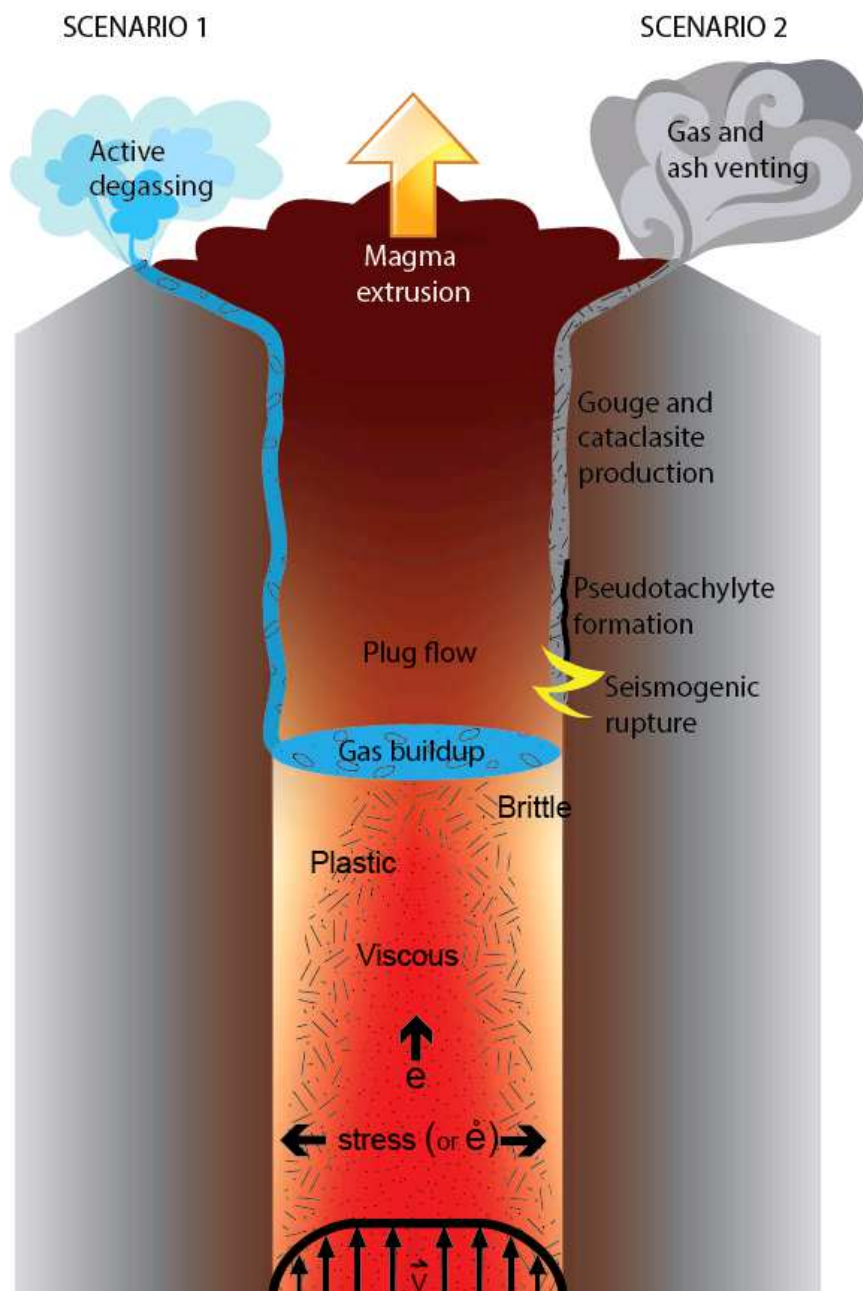
Figure 7-1. A composite image of conduit processes. The ascent of magma through the conduit is depicted, transitioning from viscous to crystal-plastic to brittle deformation with increasing strain rate ($\mathring{\varepsilon}$)) toward the conduit wall or total strain (ε) during ascent. At which point strain localisation results in plug flow, and gas pressure below the plug may be released via active degassing along fractured conduit margin (Scenario 1) or can result in repeat stick-slip events, seismogenic rupture, pseudotachylyte generation, gouge production and gas and ash venting (Scenario 2).

Understanding the behaviour of volcanoes during periods of unrest is of vital importance not only to the people who live within sight of their flanks but to the population as a whole. By examining the products of past eruptions, by actively monitoring on-going activity, and via laboratory experimentation, models of volcanic unrest may be improved. This study focuses on the premise that strain localisation in magma, during ascent, alters its intrinsic strength by exploiting pre-existing weaknesses in the multi-phase system (crystals, pores and silicate melt), dictating its fate; to "flow or blow". A combination of field, analytic and experimental studies from Volcán de Colima (Mexico), Mount St. Helens (USA) and Soufrière Hills (Montserrat) are brought together to investigate the processes involved with magma ascent during dome-building eruptions (Figure 7-1).

In terms of magma rheology the findings indicate that crystalline magmas are strain-rate dependent; viscosity is lower when deformed at faster strain rate, evidence of shear thinning behaviour. Relative viscosity decreases as a function of strain, independent of crystal fraction under the range investigated, thus the previously termed "time-dependent" deformation should more properly be called "strain-dependent" deformation. At a given temperature and stress, chemically similar lava types can display a significant range of measured strain rates as a result of crystallinity and porosity.

During high-temperature deformation of crystalline magma it is possible to impart an irreversible, crystal-plastic deformation on the phenocrysts themselves; crystal-plastic deformation of plagioclase, diopside and hypersthene is attainable under magmatic conditions. Crystal plasticity may be viewed as an important outlet for strain and a mechanism that accommodates some of the permanent, inelastic deformation imparted on magma. The amount of strain experienced by each crystal is dependent upon aspect ratio and the relative strengths of the minerals, but does tend to increase with increasing stress or total strain and therefore crystal relics in magma can act as strain markers. As deformation increases, the plastic limit of the suspended crystals may be exceeded, demonstrating the ability of plastic deformation to lead bulk ductile deformation toward brittle failure. The deformability of suspended particles necessarily influences the non-Newtonian behaviour of magma, complicating the viscous-brittle transition. Indeed crystal plasticity may be an important stage in the transition, and could occupy a time-space interval in ascending magma (Figure 7-1), the locus of which is dependent upon total strain (~ ascent), total shear stress (which increases towards the margins of the conduit) and crystallinity (itself dependent upon composition and temperature).

Additionally the viscosity of multi-phase magmas relies heavily upon the intrinsic strength of the magma. As total strain increases, crystalline magmas follow an evolution from elastic, strain hardening, constant-rate and finally strain weakening behaviour. The physical attributes of the sample dictate the point at which each stage occurs. Strain hardening comprises of a period of magmatic flow, during which pre-existing pore space is closed. The constant-rate period corresponds to crystal rearrangement and the occurrence of crystal plasticity and sporadic fractures in phenocrysts during crystal-crystal interactions. After a certain threshold (of strain, dependent upon stress) fracture coalescence and damage zone development begins. Structural deterioration of a material can result in lower apparent viscosities than anticipated, especially at high strain rates, and behaviour deviates from that of magmatic flow. In regimes where strain can be localised, specifically at conduit margins, crystal-plastic deformation is locked into the magma and may precede magma fracture, which is dependent on the strength of the magma. With integration into rheological models, crystal-plastic deformation may well become a valuable strain marker, while integration of physical magma properties can help characterise magma in the approach to failure.

The rearrangement of homogeneously distributed pore space during deformation of magma at high temperature creates anisotropy (with cracks in preferred orientations). Coalescence of cracks results in damage zones in the areas of highest strain localisation, and these pathways dictate the permeable porous network. Although physical evidence shows that the samples experience significant damage, the axially-measured dynamic elastic moduli do not change significantly, and thus do not represent the true characteristics of the samples. Hence, extreme care should be taken when using ultrasonic wave velocities as a proxy for strain (or damage). In a volcanic setting these damage zones, formed along conduit margins, can result in active degassing (Scenario 1, Figure 7-1), and can depressurise the conduit-dwelling magma. Additionally, the rearrangement of the porosity results in areas of magma densification and closure of the permeable porous network. The highly viscous, impermeable magmas can form a magma plug in the conduit, resulting in gas entrapment below which can subsequently lead to stepwise extrusion of a magma spine accompanied by "drumbeat" seismicity.

An archetypal case study for magma plug extrusion is the 2004-2008 eruption of Mount St. Helens. Throughout the eruption, a spatial and temporal differentiation of mechanical behaviour took place as extrusion slowed and the eruptive vent migrated. Well-documented gouge layers

cover the surface of all extruded spines, and thin throughout the eruption, but there also exists a previously undocumented rock unit below the gouge at spine 7 that is interpreted here as a pseudotachylyte. Field observations, porosity and density measurements, geochemical, mineralogical, and microstructural studies, crystal size and shape distribution, kinetic properties and magnetic analyses were used to help identify this existence. Formation is attributed to extreme frictional processes at a depth below 1km (Scenario 2, Figure 7-1). A link is made to 2 large LP events akin to "drumbeat" events (similar signals and source locations) that could have represented meters of slip along the conduit margin, allowing melting of the crystalline magma plug surface. Further frictional processes, after re-crystallisation, led to gouge formation at depths above 1 km. A second case study from Soufrière hills volcano (Montserrat) shows inter-banded pseudotachylyte and granular, cataclastic layers forming a <2 cm thick ribbon, laterally continuous over almost 1 m, which has been ductilely deformed post-formation. The mineralogy, thermal properties and magnetic signature of the vein confirm its status as a pseudotachylyte. In tectonic settings pseudotachylytes have been linked to seismogenic ruptures at velocities > 0.1 m/s, and at Soufrière hills, extrusion proceeded following a stick-slip motion with accompanying repetitive, "drumbeat" seismicity which could have been produced by slip events on the order of 10^{-2} m/s; which should be more than sufficient to create frictional melt.

These two case studies document unequivocal evidence of frictional melt generation in still-viscous, conduit-dwelling magma for the first time (Scenario 2, Figure 7-1). Given the high geotherm in volcanic settings, the pseudotachylyte does differ slightly from that formed in tectonic or impact settings. High ambient temperatures result in near equilibrium melting and slower recrystallisation, punctuated by a period of ductile deformation, and also prevent the development of signature "quench" characteristics. However data here suggests that magnetic measurements may be the "go-to" tool for identification of volcanic pseudotachylytes, even when mineralogy is inconclusive. Shear band formation, including the generation of pseudotachylyte, and can control the permeable porous network because the aphanitic, finely crystalline pseudotachylyte is almost pore-free and hence largely impermeable.

This study also shows that generation of frictional melt has important implications for eruption dynamics, due to its control over conduit margin slip-zone properties. High-velocity rotary shear (HVR) experiments show that, starting from room temperature, frictional melting of the magmas can occur in under 1 s (<< 1 m) at a velocity of 1.5 m/s. At lower velocities melting

occurs comparatively later due to dissipation of heat from the slip zone, although the temperature gradient in a volcanic system would be less significant. It is also evident that frictional properties of melt differ greatly from those of gouge and cataclasite, and slip properties are controlled by the viscous attributes of the melt instead of following Byerlee's law. Variable-rate HVR experiments which mimic rapid velocity fluctuations in stick-slip behaviour demonstrate the velocity-weakening character of melt, with a tendency for unstable slip. The experiments verify our postulations from field evidence; that pseudotachylyte may be linked to "drumbeat" seismicity and stick-slip motion which are so commonly observed at dome-building volcanoes. Indeed, it is believed that stick-slip motion in volcanic conduits is a self-driving, frictional-melt-regulated force and proceeds as follows: when a failure and slip event forms a melt layer at the conduit margin the high velocity creates a lubricating effect and slip is maintained. As slip velocity wanes the apparent melt viscosity increases, causing an increase in shear resistance that acts as a viscous brake and halts slip (the "stick" of stick-slip motion) with a fault zone healed by the melt. Sufficient buoyancy-driven pressure from ascending magma below eventually overcomes resistance to produce another failure and rapid slip event (the "slip"). The fault zone is once again temporarily lubricated due to velocity-weakening, but new magma below experiences the same slip event more slowly as the magma decompresses (in a concertina effect), and as the velocity decreases the shear resistance increases to once again bring into effect the viscous brake. The fixed spatial locus of repetitive "drumbeats" and the occurrence of "families" of similar seismic events is accounted for by the arrival of fresh magma at a fixed source. Post-crystallisation, pseudotachylyte at the conduit margin may suffer further frictional processes, but as stresses wane, instead of melting they can form gouge and cataclasite (as shown at Mount St. Helens, where the surficial gouge layer cross-cuts the pseudotachylyte).

Further work is required to fully understand the consequence of strain localisation and damage evolution in magma. The effect of magma fracture on apparent viscosity is of upmost importance; the multi-scale process (which in-part dictates magma rheology) must be integrated into rhelogical models in corroboration with crystal- and pore-effects. Additionally, the demonstrable deformability of crystals via crystal-plastic dislocation inevitably contributes to the non-Newtonian behaviour of magmas. It would be of great significance to quantify this crystal-plastic deformation. By imparting known conditions on crystalline magmas and comparing resultant crystal-plastic deformation to natural samples an invaluable tool, which would use crystal relics as strain markers, could be developed.

As demonstrated here, crystal plasticity can lead a crystalline sample toward bulk brittle failure, but the degree to which this is the case is not resolved. Further investigations using EBSD could resolve not only the internal deformations, but also the alignment of crystals into preferential strain-localised shear zones. The geometry of these shear zones (dependent upon stress and strain, and the physical structure of the crystalline suspension) can be of vital importance to the investigation of frictional magma properties. Advances in the field of volcanology will be attained by investigation of the slip properties of magma; of great importance during dome-building eruptions, sector collapse and caldera subsidence for example. Here, we demonstrate that slip zone properties at conduit margins may supersede the effect of buoyant magma during ascent. But additionally, quantified frictional behaviour with slip during comminution and gouge formation could be retrospectively compared with extrusion dynamics (for example at Mount St. Helens where the 2004-2008 spines were covered by a carapace of gouge) to understand their effect during volcanic eruptions.

It is anticipated that high-viscosity magma ascent is regularly accompanied by marginal frictional melting, which may then act as a viscous melt brake and heal a fault plane. High velocity rotary shear (HVR) experiments could help resolve the shear stress required for fracture and sliding including during repeat rupture-healing cycles as envisaged in conduit settings. This could be attained by developing a high-temperature furnace for the HVR to better mimic volcanological P-T conditions. Additionally, acoustic emission (AE) monitoring of laboratory experiments has been shown to scale to seismic unrest at volcanoes (Lavallée et al., 2008; Smith, 2006; Smith et al., 2009). The addition of an AE system to HVR experiments to monitor the signals of repeat fracturing events on a slip plane could help understand sub-surface volcanic signals, acceleration rates (in accordance with the failure forecast method (Kilburn, 2003; Voight, 1988)) and ultimately lead to a better understanding of magma ascent.

"Scared to death on the first day of spring
Stood a robin who wanted to sing
So we took in the scene of impossible green
Wondering how we should cause such a thing"

-TV on the radio

References

Abe, S., Dieterich, J.H., Mora, P. and Place, D., 2002. Simulation of the Influence of Rate- and State-dependent Friction on the Macroscopic Behavior of Complex Fault Zones with the Lattice Solid Model. Pure and Applied Geophysics, 159(9): 1967-1983.

Abramoff, M.D., Magalhaes, P.J. and Ram, S.J., 2004. Image processing with ImageJ. Biophotonics International, 11: 36-42.

Alidibirov, M. and Dingwell, D.B., 1996. An experimental facility for the investigation of magma fragmentation by rapid decompression. Bulletin of Volcanology, 58(5): 411-416.

Alidibirov, M., Dingwell, D.B., Stevenson, R.J., Hess, K.U., Webb, S.L. and Zinke, J., 1997. Physical properties of the 1980 Mount St. Helens cryptodome magma. Bulletin of Volcanology, 59(2): 103-111.

Allen, G.B. (Editor), 1961. Selected Letters Of Pliny. Oxford University Press, London.

Altenberger, U., Prosser, G. and Grande, A., 2010. Microstructure and petrology of a garnet-bearing pseudotachylyte of Calabria- a link to lower crustal hypocenters, Workshop: Physico-chemical processes in seismic faults, Padova, Italy.

Arámbula-Mendoza, R., Lesage, P., Valdés-González, C., Varley, N.R., Reyes-Dávila, G. and Navarro, C., 2011. Seismic activity that accompanied the effusive and explosive eruptions during the 2004-2005 period at Volcán de Colima, Mexico. Journal of Volcanology and Geothermal Research, 205(1-2): 30-46.

Atlas, Z.D., Dixon, J.E., Sen, G., Finny, M. and Martin-Del Pozzo, A.L., 2006. Melt inclusions from Volcán Popocatépetl and Volcán de Colima, Mexico: Melt evolution due to vapor-saturated crystallization during ascent. Journal of Volcanology and Geothermal Research, 153(3-4): 221-240.

Barmin, A., Melnik, O. and Sparks, R.S.J., 2002. Periodic behavior in lava dome eruptions. Earth and Planetary Science Letters, 199(1-2): 173-184.

Baxter, P.J., Bonadonna, C., Dupree, R., Hards, V.L., Kohn, S.C., Murphy, M.D., Nichols, A., Nicholson, R.A., Norton, G., Searl, A., Sparks, R.S.J. and Vickers, B.P., 1999. Cristobalite in Volcanic Ash of the Soufriere Hills Volcano, Montserrat, British West Indies. Science, 283(5405): 1142-1145.

Bell, T.H. and Etheridge, M.A., 1973. Microstructure of mylonites and their descriptive terminology. Lithos, 6(4): 337-348.

Bell, T.H. and Etheridge, M.A., 1976. The deformation and recrystallization of quartz in a mylonite zone, Central Australia. Tectonophysics, 32(3-4): 235-267.

Ben-Zion, Y. and Sammis, C.G., 2003. Characterization of Fault Zones. Pure and Applied Geophysics, 160(3): 677-715.

Benson, P.M., Vinciguerra, S., Meredith, P.G. and Young, R.P., 2008. Laboratory simulation of volcano seismicity. Science, 322: 249-252.

Benson, P.M., Vinciguerra, S., Meredith, P.G. and Young, R.P., 2010. Spatio-temporal evolution of volcano seismicity: A laboratory study. Earth and Planetary Science Letters, 297(1-2): 315-323.

Biasi, G.P. and Weldon, R.J., II, 2006. Estimating Surface Rupture Length and Magnitude of Paleoearthquakes from Point Measurements of Rupture Displacement. Bulletin of the Seimological Society of America, 96(5): 1612-1623.

Bizzarri, A., 2011. Dynamic seismic ruptures on melting fault zones. J. Geophys. Res., 116(B2): B02310.

Bloemendal, J., King, J.W., Hall, F.R. and Doh, S.J., 1992. Rock Magnetism of Late Neogene and Pleistocene Deep-Sea Sediments: Relationship to Sediment Source, Diagenetic Processes, and Sediment Lithology. J. Geophys. Res., 97(B4): 4361-4375.

Brantut, N., Schubnel, A., Rouzaud, J.N., Brunet, F. and Shimamoto, T., 2008. High-velocity frictional properties of a clay-bearing fault gouge and implications for earthquake mechanics. Journal of Geophysical Research: Solid Earth, 113(B10): n/a-n/a.

Breton, M., Ramirez Ruiz, J.J. and Navarro, C., 2002. Summary of the historical eruptive activity of Volcan de Colima, Mexico: 1519-2000. Journal of Volcanology and Geothermal Research, 117: 21-46.

Byerlee, J.D., 1978. Friction of rocks. Pure Applied Geophysics, 116: 615-626.

Cardwell, R.K., Chinn, D.S., Moore, G.F. and Turcotte, D.L., 1978. Frictional heating on a fault zone with finite thickness. Geophysical Journal of the Royal Astronomical Society, 52(3): 525-530.

Caricchi, L., Burlini, L., Ulmer, P., Gerya, T., Vassalli, M. and Papale, P., 2007. Non-Newtonian rheology of crystal-bearing magmas and implications for magma ascent dynamics. Earth and Planetary Science Letters, 264: 402-419.

Carn, S.A., Watts, R.B., Thompson, G. and Norton, G.E., 2004. Anatomy of a lava dome collapse: the 20 March 2000 event at Soufrière Hills Volcano, Montserrat. Journal of Volcanology and Geothermal Research, 131(3–4): 241-264.

Carreau, P.J., Lavoie, P.A. and Yziquel, F., 1999. Rheological properties of concentrated suspensions. In: D.D.K. D.A. Siginer and R.P. Chhabra (Editors), Rheology Series. Elsevier, pp. 1299-1345.

Cashman, K.V., Thornber, C.R. and Pallister, J.S., 2008. From Dome to Dust: Shallow Crystallization and Fragmentation of Conduit Magma During the 2004-2006 Dome Extrusion of Mount St. Helens, Washington. In: D.R. Sherrod, W.E. Scott and P.H. Stauffer (Editors), A Volcano Rekindled: The Renewed Eruption of Mount St. Helens, 2004-2006. Professionnal Paper 1750. U.S. Geological Survey, pp. 387-413.

Castro, J.M., Cordonnier, B., Tuffen, H., Tobin, M.J., Puskar, L., Martin, M.C. and Bechtel, H.A., 2012. The role of melt-fracture degassing in defusing explosive rhyolite eruptions at volcán Chaitén. Earth and Planetary Science Letters, 333–334(0): 63-69.

Chadwick, W.W., Swanson, D.A., Iwatsubo, E.Y., Heliker, C.C. and Leighley, T.A., 1983. Deformation Monitoring at Mount St. Helens in 1981 and 1982. Science, 221(4618): 1378-1380.

Chen, D.-s., Song, B., Wang, L.-n., Qi, T., Wang, Y. and Wang, W.-j., 2011. Solid state reduction of Panzhihua titanomagnetite concentrates with pulverized coal. Minerals Engineering, 24(8): 864-869.

Chester, F.M., 1994. Effects of temperature on friction: Constitutive equations and experiments with quartz gouge. J. Geophys. Res., 99(B4): 7247-7261.

Chester, F.M. and Chester, J.S., 1998. Ultracataclasite structure and friction processes of the Punchbowl fault, San Andreas system, California. Tectonophysics, 295(1-2): 199-221.

Chouet, B., 1988. Resonance of a fluid-driven crack: Radiation properties and implications for the source of long-period events and harmonic tremor. Journal of Geophysical Research: Solid Earth, 93(B5): 4375-4400.

Cimarelli, C., Costa, A., Mueller, S. and Mader, H.M., 2011. Rheology of magmas with bimodal crystal size and shape distributions: Insights from analog experiments. Geochem. Geophys. Geosyst., 12(7): Q07024.

Cordonnier, B., Caricchi, L., Pistone, M., Castro, J., Hess, K.-U., Gottschaller, S., Manga, M., Dingwell, D.B. and Burlini, L., 2012. The viscous-brittle transition of crystal-bearing silicic melt: Direct observation of magma rupture and healing. Geology, 40(7): 611-614.

Cordonnier, B., Hess, K.-U., Lavallée, Y. and Dingwell, D.B., 2009. Rheological properties of dome lavas: Case study of Unzen volcano. Earth and Planetary Science Letters, 279(3-4): 263-272.

Costa, A., 2005. Viscosity of high crystal content melts: Dependence on solid fraction. Geophysical Research Letters, 32(22): n/a-n/a.

Costa, A., Sparks, R.S.J., Macedonio, G. and Melnik, O., 2009. Effects of wall-rock elasticity on magma flow in dykes during explosive eruptions. Earth and Planetary Science Letters, 288(3-4): 455-462.

Costa, A., Wadge, G. and Melnik, O., 2012. Cyclic extrusion of a lava dome based on a stick-slip mechanism. Earth and Planetary Science Letters, 337–338(0): 39-46.

Cowie, P.A. and Scholz, C.H., 1992. Displacement-length scaling relationship for faults: data synthesis and discussion. Journal of Structural Geology, 14 (10): 1149-1156.

Curewitz, D. and Karson, J.A., 1999. Ultracataclasis, sintering, and frictional melting in pseudotachylytes from East Greenland. Journal of Structural Geology, 21(12): 1693-1713.

D'Oriano, C., Poggianti, E., Bertagnini, A., Cioni, R., Landi, P., Polacci, M. and Rosi, M., 2005. Changes in eruptive style during the A.D. 1538 Monte Nuovo eruption (Phlegrean Fields, Italy): the role of syn-eruptive crystallization. Bulletin of Volcanology, 67(7): 601-621.

Day, R., Fuller, M. and Schmidt, V.A., 1977. Hysteresis properties of titanomagnetites: Grain-size and compositional dependence. Physics of The Earth and Planetary Interiors, 13(4): 260-267.

Del Gaudio, P., Di Toro, G., Han, R., Hirose, T., Nielsen, S., Shimamoto, T. and Cavallo, A., 2009. Frictional melting of peridotite and seismic slip. Journal of Geophysical Research: Solid Earth, 114(B6): n/a-n/a.

Deubelbeiss, Y., Kaus, B.J.P., Connolly, J.A.D. and Caricchi, L., 2011. Potential causes for the non-Newtonian rheology of crystal-bearing magmas. Geochem. Geophys. Geosyst., 12(5): Q05007.

Di Toro, G., Hirose, T., Nielsen, S., Pennacchioni, G. and Shimamoto, T., 2006. Natural and experimental evidence of melt lubrication of faults during earthquakes. Science, 311(5761): 647-649.

Di Toro, G., Pennacchioni, G. and Nielsen, S., 2009. Chapter 5 Pseudotachylytes and Earthquake Source Mechanics. In: F. Eiichi (Editor), International Geophysics. Academic Press, pp. 87-133.

Dieterich, J.H., 1979. Modeling of rock friction: 1. Experimental results and constitutive equations. Journal of Geophysical Research: Solid Earth, 84(B5): 2161-2168.

Dieterich, J.H. and Kilgore, B.D., 1994. Direct observation of frictional contacts: New insights for state-dependent properties. Pure and Applied Geophysics, 143(1): 283-302.

Dingwell, D. and Webb, S.L., 1989. Structural relaxation in silicate melts and Non-Newtonian melt rheology in geologic processes. Physics and Chemistry of Minerals, 16: 508-516.

Dingwell, D.B., 1996. Volcanic dilemma: Flow or blow? Science, 273(5278): 1054-1055.

Dingwell, D.B., 1997. The Brittle–Ductile Transition in High-Level Granitic Magmas: Material Constraints. Journal of Petrology, 38(12): 1635-1644.

Divoux, T., Vidal, V., Ripepe, M. and Géminard, J.-C., 2011. Influence of non-Newtonian rheology on magma degassing. Geophys. Res. Lett., 38(12): L12301.

Dominguez, T., Zobin, V.M. and Reyes-Davila, G.A., 2001. The fracturing in volcanic edifice before an eruption: the June-July 1998 high-frequency earthquake swarm at Volcan de Colima, Mexico. Journal of Volcanology and Geothermal Research, 105(1-2): 65-75.

Dunlop, D.J., 2002. Theory and application of the Day plot (Mrs/Ms versus Hcr/Hc) 1. Theoretical curves and tests using titanomagnetite data. J. Geophys. Res., 107(B3): 2056.

Edmonds, M. and Herd, R.A., 2007. A volcanic degassing event at the explosive-effusive transition. Geophys. Res. Lett., 34(21): L21310.

Einstein, A., 1906. Eine neue Bestimmung der Moleküldimensionen Annalen der Physik, 19: 289-306.

Faulkner, D.R., Mitchell, T.M., Jensen, E. and Cembrano, J., 2011. Scaling of fault damage zones with displacement and the implications for fault growth processes. J. Geophys. Res., 116(B5): B05403.

Ferré, E.C., Zechmeister, M.S., Geissman, J.W., MathanaSekaran, N. and Kocak, K., 2005. The origin of high magnetic remanence in fault pseudotachylites: Theoretical considerations and implication for coseismic electrical currents. Tectonophysics, 402(1–4): 125-139.

Fialko, Y. and Khazan, Y., 2005. Fusion by earthquake fault friction: Stick or slip? J. Geophys. Res.-Solid Earth, 110.

Fletcher, J., Ceuleneer, G. and Cannat, M., 1997. Microfabrics and patterns of dynamic recrystallization in gabbroic rocks from the MARK area, Mid-Atlantic Ridge. , College Station,TX (Ocean Drilling Program), 143-153 pp.

Foss, D.R. and Brady, J.F., 2000. Structure, diffusion and rheology of Brownian suspensions by Stokesian Dynamics simulation. Journal of Fluid Mechanics, 407: 167-200.

Freund, F., Salgueiro da Silva, M.A., Lau, B.W.S., Takeuchi, A. and Jones, H.H., 2007. Electric currents along earthquake faults and the magnetization of pseudotachylite veins. Tectonophysics, 431(1–4): 131-141.

Garcia, M. and Jacobson, S., 1979. Crystal clots, amphibole fractionation and the evolution of calc-alkaline magmas. Contributions to Mineralogy and Petrology, 69(4): 319-327.

Gavilanes-Ruiz, J.C., Cuevas-Muñiz, A., Varley, N., Gwynne, G., Stevenson, J., Saucedo-Girón, R., Pérez-Pérez, A., Aboukhalil, M. and Cortés-Cortés, A., 2009. Exploring the factors that influence the perception of risk: The case of Volcán de Colima, Mexico. Journal of Volcanology and Geothermal Research, 186(3-4): 238-252.

Gent, A.N., 1960. Theory of the parallel plate viscometer. British Journal of Applied Physics, 11(2): 85.

Giordano, D., Nichols, A.R.L. and Dingwell, D.B., 2005. Glass transition temperatures of natural hydrous melts: a relationship with shear viscosity and implications for the welding process. Journal of Volcanology and Geothermal Research, 142(1-2): 105-118.

Giordano, D., Russell, J.K. and Dingwell, D.B., 2008. Viscosity of magmatic liquids: A model. Earth and Planetary Science Letters, 271(1-4): 123-134.

Gonnermann, H.M. and Manga, M., 2003. Explosive volcanism may not be an inevitable consequence of magma fragmentation. Nature, 426: 432-435.

Gonnermann, H.M. and Manga, M., 2005. Flow banding in obsidian: A record of evolving textural heterogeneity during magma deformation. Earth and Planetary Science Letters, 236: 135-147.

González, M.B., Ramírez, J.J. and Navarro, C., 2002. Summary of the historical eruptive activity of Volcán De Colima, Mexico 1519-2000. Journal of Volcanology and Geothermal Research, 117(1-2): 21-46.

Gottsmann, J., Giordano, D. and Dingwell, D.B., 2002. Predicting shear viscosity during volcanic processes at the glass transition: a calorimetric calibration. Earth and Planetary Science Letters, 198(3-4): 417-427.

Gottsmann, J., Lavallée, Y., Martí, J. and Aguirre-Díaz, G., 2009. Magma–tectonic interaction and the eruption of silicic batholiths. Earth and Planetary Science Letters, 284(3–4): 426-434.

Gudmundsson, A., 2006. How local stresses control magma-chamber ruptures, dyke injections, and eruptions in composite volcanoes. Earth Science Reviews.

Gudmundsson, A. and Brenner, L.S., 2009. Local stresses, dyke arrest and surface deformation in volcanic edificesand rift zones.

Gudmundsson, A. and Philipp, S.L., 2006. How local stress fields prevent volcanic eruptions. Journal of Volcanology and Geothermal Research, In Press, Corrected Proof.

Hale, A.J. and Muhlhaus, H.B., 2007. Modelling shear bands in a volcanic conduit: Implications for over-pressures and extrusion-rates. Earth and Planetary Science Letters, 263(1-2): 74-87.

Hale, A.J. and Wadge, G., 2008. The transition from endogenous to exogenous growth of lava domes with the development of shear bands. Journal of Volcanology and Geothermal Research, 171(3-4): 237-257.

Handy, M.R., Wissing, S.B. and Streit, L.E., 1999. Frictional-viscous flow in mylonite with varied bimineralic composition and its effect on lithospheric strength. Tectonophysics, 303(1-4): 175-191.

Hanks, T. and Kanamori, H., 1979. A moment magnitude scale. J. Geophys. Res., 84(B5): 2348-2350.

Hawkins, A.B., 1998. Aspects of rock strength. Bulletin of Engineering Geology and the Environment, 57: 17-30.

Hayman, N.W., Housen, B.A., Cladouhos, T.T. and Livi, K., 2004. Magnetic and clast fabrics as measurements of grain-scale processes within the Death Valley shallow crustal detachment faults. American Geophysical Union, Washington DC.

Heap, M.J., Baud, P., Meredith, P.G., Vinciguerra, S., Bell, A.F. and Main, I.G., 2011. Brittle creep in basalt and its application to time-dependent volcano deformation. Earth and Planetary Science Letters, 307(1–2): 71-82.

Heap, M.J., Faulkner, D.R., Meredith, P.G. and Vinciguerra, S., 2010. Elastic moduli evolution and accompanying stress changes with increasing crack damage: implications for stress changes around fault zones and volcanoes during deformation. Geophysical Journal International, 183(1): 225-236.

Heap, M.J., Vinciguerra, S. and Meredith, P.G., 2009. The evolution of elastic moduli with increasing crack damage during cyclic stressing of a basalt from Mt. Etna volcano. Tectonophysics, 471: 153-160.

Herd, R.A., Edmonds, M. and Bass, V.A., 2005. Catastrophic lava dome failure at Soufrière Hills Volcano, Montserrat, 12–13 July 2003. Journal of Volcanology and Geothermal Research, 148(3–4): 234-252.

Herriott, T.M., Sherrod, D.R., Pallister, J.S. and Vallance, J.W., 2008. Photogeologic Maps of the 2004-2005 Mount St. Helens Eruption. In: D.R. Sherrod, W.E. Scott and P.H.

Stauffer (Editors), A Volcano Rekindled: The Renewed Eruption of Mount St. Helens, 2004-2006. Professionnal Paper 1750. U.S. Geological Survey, pp. 209-224.

Herwegh, M. and Handy, M.R., 1998. The origin of shape preferred orientations in mylonite: inferences from in-situ experiments on polycrystalline norcamphor. Journal of Structural Geology, 20(6): 681-694.

Hess, K.U., Cordonnier, B., Lavallée, Y. and Dingwell, D.B., 2007. High-load, high-temperature deformation apparatus for synthetic and natural silicate melts. Rev Sci Instrum, 78(7): 075102.

Hippert, J.F. and Hongn, F.D., 1998. Deformation mechanisms in the mylonite/ultramylonite transition. Journal of Structural Geology, 20(11): 1435-1448.

Hirose, T. and Shimamoto, T., 2005. Slip-Weakening Distance of Faults during Frictional Melting as Inferred from Experimental and Natural Pseudotachylytes. Bulletin of the Seismological Society of America, 95(5): 1666-1673.

Holness, M.B., 2002. Spherulitic textures formed during crystallization of partially melted arkose, Rum, Scotland. Geological Magazine, 139(6): 651-663.

Horwell, C., Blond, J., Michnowicz, S.K. and Cressey, G., 2010. Cristobalite in a rhyolitic lava dome: evolution of ash hazard. Bulletin of Volcanology, 72(2): 249-253.

Hürlimann, M., Garcia Piera, J.O., Ledesma, A, 2000. Causes and mobility of large volcanic landslides : application to Tenerife, Canary Islands. Elsevier, Oxford, ROYAUME-UNI, 474 pp.

Ida, Y., 1972. Cohesive Force across the Tip of a Longitudinal-Shear Crack and Griffith's Specific Surface Energy. J. Geophys. Res., 77(20): 3796-3805.

Ikeda, R., K. Omura, Hickman, H.H. and Matsuda, T., 2003. Unzen volcano scientific drilling : structure and stress state inferred from downhole measurements in the flank drilling. Geophysical Exploration, 56: 391-399.

Iverson, R.M., 2005. A Dynamical Model of Seismogenic Dome Extrusion, Mount St. Helens, 2004-2005. EOS Trans AGU: V52B-04.

Iverson, R.M., Dzurisin, D., Gardner, C.A., Gerlach, T.M., LaHusen, R.G., Lisowski, M., Major, J.J., Malone, S.D., Messerich, J.A., Moran, S.C., Pallister, J.S., Qamar, A.I., Schilling, S.P. and Vallance, J.W., 2006. Dynamics of seismogenic volcanic extrusion at Mount St Helens in 2004-05. Nature, 444: 439-443.

Kennedy, B., Spieler, O., Scheu, B., Kueppers, U., Taddeucci, J. and Dingwell, D.B., 2005. Conduit implosion during Vulcanian eruptions. Geology, 33(7): 581-584.

Kennedy, L.A. and Russell, J.K., 2011. Cataclastic production of volcanic ash at Mount Saint Helens. Physics and Chemistry of the Earth, Parts A/B/C, In Press, Corrected Proof.

Kennedy, L.A., Russell, J.K. and Nelles, E., 2009. Origins of Mount St. Helens cataclasites: Experimental insights. American Mineralogist, 94(7): 995-1004.

Kilburn, C.R.J., 2003. Multiscale fracturing as a key to forecasting volcanic eruptions. Journal of Volcanology and Geothermal Research, 125: 271-289.

Kim, J.W., Ree, J.H., Han, R. and Shimamoto, T., 2010. Experimental evidence for the simultaneous formation of pseudotachylyte and mylonite in the brittle regime. Geology, 38(12): 1143-1146.

Kittler, J., Illingworth, J. and Foglein, J., 1985. Threshold selection based on a simple image statistic Computer Vision Graphics and Image Processing, 30(2): 125-147.

Kolzenburg, S., Heap, M.J., Lavallée, Y., Russell, J.K., Meredith, P.G. and Dingwell, D.B., 2012. Strength and permeability recovery of tuffisite-bearing andesite. Solid Earth, 3: 191-198.

Kueppers, U., Scheu, B., Spieler, O. and Dingwell, D.B., 2006. Fragmentation efficiency of explosive volcanic eruptions: A study of experimentally generated pyroclasts. Journal of Volcanology and Geothermal Research, 153(1-2): 125-135.

Lavallée, Y., Benson, P., Hess, K.-U., Flaws, A., Schillinger, B., Meredith, P.G. and Dingwell, D.B., 2013. Reconstructing magma failure and the permeable degassing network. Geology, In Press.

Lavallée, Y., Hess, K.U., Cordonnier, B. and Dingwell, D.B., 2007. Non-Newtonian rheological law for highly crystalline dome lavas. Geology, 35(9): 843-846.

Lavallée, Y., Meredith, P.G., Dingwell, D.B., Hess, K.U., Wassermann, J., Cordonnier, B., Gerik, A. and Kruhl, J.H., 2008. Seismogenic lavas and explosive eruption forecasting. Nature, 453(7194): 507-510.

Lavallée, Y., Mitchell, T.M., Heap, M.J., Vasseur, J., Hess, K.-U., Hirose, T. and Dingwell, D.B., 2012. Experimental generation of volcanic pseudotachylytes: Constraining rheology. Journal of Structural Geology, 38(0): 222-233.

Lavallée, Y., Varley, N., Alatorre-Ibargüengoitia, M., Hess, K.U., Kueppers, U., Mueller, S., Richard, D., Scheu, B., Spieler, O. and Dingwell, D., 2011. Magmatic architecture of dome-building eruptions at Volcán de Colima, Mexico. Bulletin of Volcanology: 1-12.

Lejeune, A.M., Bottinga, Y., Trull, T.W. and Richet, P., 1999. Rheology of bubble-bearing magmas. Earth and Planetary Science Letters, 166(1): 71-84.

Lejeune, A.M. and Richet, P., 1995. Rheology of Crystal-Bearing Silicate Melts - An Experimental study at High Viscosities. Journal of Geophysical Research, 100(B3): 4215-4229.

Lensky, N.G., Sparks, R.S.J., Navon, O. and Lyakhovsky, V., 2008. Cyclic activity at Soufrière Hills Volcano, Montserrat: degassing-induced pressurization and stick-slip extrusion. Geological Society, London, Special Publications, 307(1): 169-188.

Lin, A., 2007. Fossil earthquakes: The formation and preservation of pseudotachylytes, Lecture Notes in Earth Sciences. Springer.

Lin, A. and Shimamoto, T., 1998. Selective melting processes as inferred from experimentally generated pseudotachylytes. Journal of Asian Earth Sciences, 16(5-6): 533-545.

Lin, A.M., 1996. Injection veins of crushing-originated pseudotachylyte and fault gouge formed during seismic faulting. Engineering Geology, 43(2-3): 213-224.

Lin, A.M., 1999. Roundness of clasts in pseudotachylytes and cataclastic rocks as an indicator of frictional melting. Journal of Structural Geology, 21(5): 473-478.

Linker, M.F. and Dieterich, J.H., 1992. Effects of variable normal stress on rock friction: observations and constitutive equations. Journal of Geophysical Research, 97(B4): 4923-4940.

Lipman, P.W., and D. R. Mullineaux (Editor), 1981. The 1980 eruptions of Mount St. Helens, Washington.

Llewellin, E.W., Mader, H.M. and Wilson, S.D.R., 2002. The constitutive equation and flow dynamics of bubbly magmas. Geophys. Res. Lett., 29(24): 2170.

Loubser, M. and Verryn, S., 2008. Combining XRF and XRD analyses and sample preparation to solve mineralogical problems. S. Afr. J. Geol., 111(2-3): 229-238.

Luhr, J.F., 2002. Petrology and geochemistry of the 1991 and 1998-1999 lava flows from Volcán de Colima, México: implications for the end of the current eruptive cycle. Journal of Volcanology and Geothermal Research, 117(1-2): 169-194.

Luhr, J.F. and Carmichael, I.S.E., 1980. The Colima Volcanic Complex, Mexico: I. Post-Caldera Andesites From Volcan Colima. Contributions to mineralogy & petrology, 71: 343-372.

Luhr, J.F. and Carmichael, I.S.E., 1990. Petrological monitoring of cyclical eruptive activity at Volcán Colima, Mexico. Journal of Volcanology and Geothermal Research, 42(3): 235-260.

Lyakhovsky, V. and Ben-Zion, Y., 2008. Scaling relations of earthquakes and aseismic deformation in a damage rheology model. Geophysical Journal International, 172(2): 651-662.

Magloughlin, J.F. and Spray, J.G., 1992. Frictional Melting Processes and Products in Geological Materials. Science Direct, 141 pp.

Manga, M., Castro, J., Cashman, K.V. and Loewenberg, M., 1998. Rheology of bubble-bearing magmas. Journal of Volcanology and Geothermal Research, 87(1): 15-28.

Marone, C. and Richardson, E., 2010. Learning to read fault-slip behavior from fault-zone structure. Geology, 38(8): 767-768.

Marsh, B.D., 1981. On the crystallinity, probability of occurrence, and rheology of lava and magma. Contributions to Mineralogy and Petrology, 78(1): 85-98.

Marti, J. and Ernst, G.G.J., 2005. Volcano hazards

Volcanoes and the Environment. Cambridge University Press.

Masch, L. and Preuss, E., 1977. Das Vorkommen des Hyalomylonits von Langtang, Himalaya (Nepal). . N. Jahrbuch für Mineralogie,, 129(3): 292-311.

Matoza, R.S. and Chouet, B.A., 2010. Subevents of long-period seismicity: Implications for hydrothermal dynamics during the 2004-2008 eruption of Mount St. Helens. J. Geophys. Res.-Solid Earth, 115: 26.

McBirney, A.R. and Murase, T., 1984. Rheological Properties of Magmas. Annual Review of Earth and Planetary Sciences, 12(1): 337-357.

Melnik, O.E., 2001. An unsteady model for volcanic-eruption dynamics involving crystallization and through-magma gas filtration. Doklady Physics, 46(4): 271-275.

Melnik, O.E. and Sparks, R.S.J., 1999. Nonlinear dynamics of lava dome extrusion. Nature, 402: 37-41.

Melnik, O.E. and Sparks, R.S.J., 2005. Controls on conduit magma flow dynamics during lava dome building eruptions. J. Geophys. Res., 110(B2): B02209.

Mikumo, T., Olsen, K.B., Fukuyama, E. and Yagi, Y., 2003. Stress-Breakdown Time and Slip-Weakening Distance Inferred from Slip-Velocity Functions on Earthquake Faults. Bulletin of the Seimological Society of America, 93(1): 264-282.

Mizoguchi, K., Hirose, T., Shimamoto, T. and Fukuyama, E., 2006. Moisture-related weakening and strengthening of a fault activated at seismic slip rates. Geophysical Research Letters, 33(16): 4.

Moecher, D.P. and Steltenpohl, M.G., 2009. Direct calculation of rupture depth for an exhumed paleoseismogenic fault from mylonitic pseudotachylyte. Geology, 37(11): 999-1002.

Monzawa, N. and Otsuki, K., 2003. Comminution and fluidization of granular fault materials: implications for fault slip behavior. Tectonophysics, 367(1-2): 127-143.

Moore, P.L., Iverson, N.R. and Iverson, R.M., 2008. Frictional properties of the Mount St. Helens gouge. In: D.R. Sherrod, W.E. Scott and P.H. Stauffer (Editors), A Volcano Rekindled: The Renewed Eruption of Mount St. Helens, 2004-2006. Professionnal Paper 1750. U.S. Geological Survey, pp. 415-424.

Mora, J.C., Macías, J.L., Saucedo, R., Orlando, A., Manetti, P. and Vaselli, O., 2002. Petrology of the 1998-2000 products of Volcán de Colima, México. Journal of Volcanology and Geothermal Research, 117(1-2): 195-212.

Moran, S.C., Malone, S.D., Qamar, A.I., Thelen, W., Wright, A.K. and Caplan-Auerbach, J., 2008. Seismicity Associated with Renewed Dome-Building at Mount St. Helens, 2004-2005. In: D.R. Sherrod, W.E. Scott and P.H. Stauffer (Editors), A Volcano Rekindled: The Renewed Eruption of Mount St. Helens, 2004-2006. Professionnal Paper 1750. U.S. Geological Survey, pp. 27-60.

Mueller, S., Llewellin, E.W. and Mader, H.M., 2011. The effect of particle shape on suspension viscosity and implications for magmatic flows. Geophys. Res. Lett., 38(13): L13316.

Mueller, S., Melnik, O., Spieler, O., Scheu, B. and Dingwell, D., 2004. Permeability and degassing of dome lavas undergoing rapid decompression: An experimental determination. Bulletin of Volcanology, 67: 526-538.

Murphy, M.D., Sparks, R.S.J., Barclay, J., Carroll, M.R. and Brewer, T.S., 2000. Remobilization of Andesite Magma by Intrusion of Mafic Magma at the Soufriere Hills Volcano, Montserrat, West Indies. Journal of Petrology, 41(1): 21-42.

Nakada, S., Shimizu, H. and Ohta, K., 1999. Overview of the 1990-1995 eruption at Unzen Volcano. Journal of Volcanology and Geothermal Research, 89: 1-22.

Nakamura, N., Hirose, T. and Borradaile, G.J., 2002. Laboratory verification of submicron magnetite production in pseudotachylytes: relevance for paleointensity studies. . Earth and Planetary Science Letters, 201(1): 13-18.

Namiki, A. and Manga, M., 2008. Transition between fragmentation and permeable outgassing of low viscosity magmas. Journal of Volcanology and Geothermal Research, 169: 48-60.

Navarro-Ochoa, C., Gavilanes-Ruíz, J.C. and Cortés-Cortés, A., 2002. Movement and emplacement of lava flows at Volcán de Colima, México: November 1998-February 1999. Journal of Volcanology and Geothermal Research, 117(1-2): 155-167.

Neuberg, J., Tuffen, H., Collier, L., Green, D., Powell, T. and Dingwell, D., 2006. The trigger mechanism of low-frequency earthquakes on Montserrat. J.Volcanol.and Geotherm.Res., 153(1-2): 37-50.

Nielsen, S., B., Carlson, J. and Olsen, K., B. , 2007. Sensitivity of 3D rupture dynamics to fault geometry and friction parameters.

Nielsen, S., Mosca, P., Giberti, G., Di Toro, G., Hirose, T. and Shimamoto, T., 2010. On the transient behavior of frictional melt during seismic slip. J. Geophys. Res.-Solid Earth, 115: 17.

O'Hara, K.D., 2001. A pseudotachylyte geothermometer. Journal of Structural Geology, 23(9): 1345-1357.

Ojovan, M., 2008. Configurons: Thermodynamic Parameters and Symmetry Changes at Glass Transition. Entropy, 10(3): 334-364.

Okumura, S., Nakamura, M., Nakano, T., Uesugi, K. and Tsuchiyama, A., 2010. Shear deformation experiments on vesicular rhyolite: Implications for brittle fracturing, degassing, and compaction of magmas in volcanic conduits. Journal of Geophysical Research: Solid Earth, 115(B6): n/a-n/a.

Okumura, S., Nakamura, M., Takeuchi, S., Tsuchiyama, A., Nakano, T. and Uesugi, K., 2009. Magma deformation may induce non-explosive volcanism via degassing through bubble networks. Earth and Planetary Science Letters, 281(3-4): 267-274.

Otsuki, K., Monzawa, N. and Nagase, T., 2003. Fluidization and melting of fault gouge during seismic slip: Identification in the Nojima fault zone and implications for focal earthquake mechanisms. J. Geophys. Res.-Solid Earth, 108(B4): 18.

Palladino, D.M., Simei, S. and Kyriakopoulos, K., 2008. On magma fragmentation by conduit shear stress: Evidence from the Kos Plateau Tuff, Aegean Volcanic Arc. Journal of Volcanology and Geothermal Research, 178(4): 807-817.

Pallister, J.S., Hoblitt, R.P., Crandell, D.R. and Mullineaux, D.R., 1992. Mount St. Helens a decade after the 1980 eruptions: magmatic models, chemical cycles, and a revised hazards assessment. Bulletin of Volcanology, 54(2): 126-146.

Pallister, J.S., Thornber, C.R., Cashman, K.V., Clynne, M.A., Lowers, H.A., Mandeville, C.W., Brownfield, I.K. and Meeker, G.P., 2008. Petrology of the 2004-2006 Mount St Helens lava dome - implications for magmatic plumbing and eruption triggering. In: D.R. Sherrod, W.E. Scott and P.H. Stauffer (Editors), A Volcano Rekindled: The Renewed Eruption of Mount St. Helens, 2004-2006. Professionnal Paper 1750. Professional Paper. U.S. Geological Survey, pp. 647-703.

Palmer, A.C. and Rice, J.R., 1973. The Growth of Slip Surfaces in the Progressive Failure of Over-Consolidated Clay. Proceedings of the Royal Society of London. A. Mathematical and Physical Sciences, 332(1591): 527-548.

Papale, P., 1999. Strain-induced magma fragmentation in explosive eruptions. Nature, 397: 425-428.

Passchier, C.W., 1982. Pseudotachylyte and the development of ultramylonite bands in the Saint-Barthélemy Massif, French Pyrenees. Journal of Structural Geology, 4(1): 69-79.

Passchier, C.W. and Trouw, R.E.J., 2005. Microtectonics. Springer, Berlin.

Paterson, M.S. and Wong, T.F., 2005. Experimental Rock Deformation - The Brittle Field. Springer, Berlin Heidelberg, 347 pp.

Petford, N., 2003. Rheology of Granitic Magmas During Ascnet and Emplacement. Annual Review of Earth and Planetary Sciences, 31(1): 399-427.

Petford, N., 2009. Which effective viscosity? Mineralogical Magazine, 73: 167-191.

Picard, D., Arbaret, L., Pichavant, M., Champallier, R. and Launeau, P., 2011. Rheology and microstructure of experimentally deformed plagioclase suspensions. Geology, 39(8): 747-750.

Poirier, J.-P. (Editor), 1985. Creep of Crystals: High-temperature Deformation Processes in Metals. University Press, Cambridge, 263 pp.

Poirier, J.P., 1995. Plastic rheology of crystals, Mineral Physics & Crystallography: A Handbook of Physical Constants. AGU Ref. Shelf. AGU, Washington, DC, pp. 237-247.

Purcaru, G. and Berckhemer, H., 1978. A magnitude scale for very large earthquakes. Tectonophysics, 49(3-4): 189-198.

Reches, Z. and Lockner, D.A., 2010. Fault weakening and earthquake instability by powder lubrication. Nature, 467(7314): 452-U102.

Reed, S.B.J., 1996. Electronic Microprobe Analysis and Scanning Electronic Microscopy in Geology. Cambridge University Press.

Rempel, A.W., 2006. The effects of flash-weakening and damage on the evolution of fault strength and temperature. In: R. Abercrombie, A. McGarr, G. DiToro and H. Kanamori (Editors), Earthquakes: Radiated Energy and the Physics of Faulting. Geophysical Monograph Series. Amer Geophysical Union, Washington, pp. 263-270.

Rice, J.R., 2006. Heating and weakening of faults during earthquake slip. J. Geophys. Res., 111(B5): B05311.

Roscoe, R., 1952. The viscosity of suspensions of rigid spheres. British Journal of Applied Physics, 3(8): 267.

Rowe, C.A., Thurber, C.H. and White, R.A., 2004. Dome growth behavior at Soufriere Hills Volcano, Montserrat, revealed by relocation of volcanic event swarms, 1995–1996. Journal of Volcanology and Geothermal Research, 134(3): 199-221.

Ruina, A., 1983. Slip Instability and State Variable Friction Laws. Journal of Geophysical Research, 88(B12).

Rutherford, M.J., 2008. Magma Ascent Rates. Reviews in Mineralogy and Geochemistry, 69(1): 241-271.

Samuelson, J., Marone, C., Voight, B. and Elsworth, D., 2008. Laboratory investigation of the frictional behavior of granular volcanic material. Journal of Volcanology and Geothermal Research, 173(3-4): 265-279.

Savov, I.P., Luhr, J.F. and Navarro-Ochoa, C., 2008. Petrology and geochemistry of lava and ash erupted from Volca[combining acute accent]n Colima, Mexico, during 1998-2005. Journal of Volcanology and Geothermal Research, 174(4): 241-256.

Scheu, B., Ichihara, M., Spieler, O. and Dingwell, D.B., 2008. A closer look at magmatic fragmentation. Geophysical Research Abstracts, 10(EGU2008): A-04786.

Schilling, S.P., Thompson, R.A., Messerich, J.A. and Iwatsubo, E.Y., 2008. Use of digital aerophotogrammetry to determine rates of lava dome growth, Mount St. Helens, 2004-2005. In: D.R. Sherrod, W.E. Scott and P.H. Stauffer (Editors), A Volcano Rekindled: The Renewed Eruption of Mount St. Helens, 2004-2006. Professionnal Paper 1750. U.S. Geological Survey, pp. 145-167.

Schlische, R.W., Young, S.S., Ackermann, R.V. and Gupta, A., 1996. Geometry and scaling relations of a population of very small rift-related normal faults. Geology, 24(8): 683-686.

Scholz, C.H., 1998. Earthquakes and friction laws. Nature, 391(6662): 37-42.

Scholz, C.H., 2002. Mechanics of earthquakes, The Mechanics of Earthquakes and Faulting. Columbia University, New York.

Scholz, C.H., Dawers, N.H., Yu, J.Z. and Anders, M.H., 1993. Fault Growth and Fault Scaling Laws - Preliminary-Results. J. Geophys. Res.-Solid Earth, 98(B12): 21951-21961.

Schultz, R.A. and Fossen, H., 2008. Terminology for structural discontinuities. AAPG Bull., 92(7): 853-867.

Scott, W.E., Sherrod, D.R. and Gardner, C.A., 2008. Overview of 2004 to 2005, and Continuing, Eruption of Mount St. Helens, Washington. In: D.R. Sherrod, W.E. Scott

and P.H. Stauffer (Editors), A Volcano Rekindled: The Renewed Eruption of Mount St. Helens, 2004-2006. Professionnal Paper 1750. U.S. Geological Survey, pp. 3-22.

Shimamoto, T. and Tsutsumi, A., 1994. A new rotary-shear high-velocity frictional testing machine: Its basic design and scope of research (in Japanese with English abstract). Structural Geology, 39: 65-78.

Sibson, R.H., 1977. Fault rocks and fault mechanisms. Journal of the Geological Society, 133.

Siddoway, C.S., Baldwin, S.L., Fitzgerald, P.G., Fanning, C.M. and Luyendyk, B.P., 2004. Ross Sea mylonites and the timing of intracontinental extension within the West Antarctic rift system. Geology, 32(1): 57-60.

Siebert, L., 2004. Landslides resulting from structural failure of volcanoes. In: S.G. Evans, and DeGraff, J.V. (Editor), Catastrophic Landslides: Effects, Occurrence and mechanisms. Reviews in Engineering Geology, Geological Society of America, Boulder, Colorado USA.

Smith, J.V., Miyake, Y. and Oikawa, T., 2001. Interpretation of porosity in dacite lava domes as ductile-brittle failure textures. Journal of Volcanology and Geothermal Research, 112(1-4): 25-35.

Smith, R., 2006. Rates of rock fracturing as a tool for forecasting eruptions at andesitic-dacitic stratovolcanoes, University of London, 369 pp.

Smith, R. and Kilburn, C.R.J., 2010. Forecasting eruptions after long repose intervals from accelerating rates of rock fracture: The June 1991 eruption of Mount Pinatubo, Philippines. Journal of Volcanology and Geothermal Research, 191(1-2): 129-136.

Smith, R., Kilburn, C.R.J. and Sammonds, P.R., 2007. Rock Fracture as a Precursor to Lava Dome Eruptions at Mount St Helens from June 1980 to October 1986. Bulletin of Volcanology, 69(6): 681-693.

Smith, R., Sammonds, P.R. and Kilburn, C.R.J., 2005. Experimental Studies of Lava Dome Fracture. Geophysical Research Letters.

Smith, R., Sammonds, P.R. and Kilburn, C.R.J., 2009. Fracturing of volcanic systems: experimental insights into pre-eruptive conditions. Earth and Planetary Science Letters, 280(1-4): 211-219.

Smith, R., Sammonds, P.R., Tuffen, H. and Meredith, P.G., 2011. Evolution of the mechanics of the 2004-2008 Mt. St. Helens lava dome with time and temperature. Earth and Planetary Science Letters, 307(1-2): 191-200.

Snieder, R., Prejean, S. and Johnson, J.B., 2006. Spatial variation in Mount St. Helens clones from coda wave analysis. Center for Wave Phenomena Consortium Preject: CPW-543.

Sosman, R.B., 1965. The phases of silica. RutgersU niversityP ress, New Brunswick, N.J., 389 pp.

Sparks, R.S.J. and Young, S.R., 2002. The eruption of Soufriere Hills Volcano, Montserrat (1995-1999): overview of scientific results. In: T.H. Druitt and B.P. Kokelaar (Editors), The Eruption of Soufriere Hills Volcano, Montserrat, from 1995 to 1999. Memoirs. Geological Society, London, pp. 45 -69.

Spieler, O., Kennedy, B., Kueppers, U., Dingwell, D.B., Scheu, B. and Taddeucci, J., 2004. The fragmentation threshold of pyroclastic rocks. Earth and Planetary Science Letters, 226(1-2): 139-148.

Spray, J.G., 1992. A physical basis for the frictional melting of some rock-forming minerals. Tectonophysics, 204(3-4): 205-221.

Spray, J.G., 2010. Frictional Melting Processes in Planetary Materials: From Hypervelocity Impact to Earthquakes. Annual Review of Earth and Planetary Sciences, 38(1): 221-254.

Stevenson, R.J., Dingwell, D.B., Webb, S.L. and Sharp, T.G., 1996. Viscosity of microlite-bearing rhyolitic obsidians: An experimental study. Bulletin of Volcanology, 58(4): 298-309.

Swanson, M.T., 1992. Fault structure, wear mechanisms and rupture processes in pseudotachylyte generation. Tectonophysics, 204(3-4): 223-242.

Taira, T., Silver, P.G., Niu, F.L. and Nadeau, R.M., 2008. Detecting seismogenic stress evolution and constraining fault zone rheology in the San Andreas Fault following the 2004 Parkfield earthquake. J. Geophys. Res.-Solid Earth, 113(B3): 16.

Thelen, W.A., Crosson, R.S. and Creager, K.C., 2008. Absolute and Relative Locations of Earthquakes at Mount St. Helens, Washington Using Continuous Data: Implications for Magmatic Processes. In: D.R. Sherrod, W.E. Scott and P.H. Stauffer (Editors), A Volcano Rekindled: The Renewed Eruption of Mount St. Helens, 2004-2006. Professionnal Paper 1750. U.S. Geological Survey, pp. 71-95.

Thornber, C.R., Pallister, J.S., Rowe, M.C., McConnell, S., Herriott, T.M., Eckberg, A., Stokes, W.C., Johnson Cornelius, D., Conrey, R.M., Hannah, T., Taggart, J.E., Adams, M., Lamothe, P.J., Budahn, J.R. and Knaack, C.M., 2008. Catalogue of Mount St. Helens 2004-2007 Dome Samples with Major- and Trace-element Chemistry.

Tilling, R.I., 1996. The role of monitoring in forecasting volcanic events . . In: W. McGuire, C.R.J. Kilburn and J.B. Murray (Editors), Monitoring active volcanoes: strategies, procedures and techniques. UCL Press, London, pp. 369-396.

Trigila, R., Battaglia, M. and Manga, M., 2008. An experimental facility for investigation hydromagmatic eruptions at high-pressure and high-temperature with application to the importance of magma porosity for magma-water interaction. Bulletin of Volcanology, 69(4): 365-372.

Tuffen, H. and Dingwell, D., 2005. Fault textures in volcanic conduits: evidence for seismic trigger mechanisms during silicic eruptions. Bulletin of Volcanology, 67(4): 370-387.

Tuffen, H., Dingwell, D.B. and Pinkerton, H., 2003. Repeated fracture and healing of silicic magma generate flow banding and earthquakes? Geology, 31(12): 1089-1092.

Tuffen, H., Smith, R. and Sammonds, P.R., 2008. Evidence for seismogenic fracture of silicic magma. Nature, 453(7194): 511-514.

Valdez-Moreno, G., Schaaf, P., Luis Macías, J. and Kusakabe, M., 2006. New Sr-Nd-Pb-O isotope data for Colima volcano and evidence for the nature of the local basement. Geological Society of America Special Papers, 402: 45-63.

Vallance, J.W., Gardner, C.A., Scott, W.E., Iverson, R.M. and Pierson, T.C., 2010. Mount St. Helens: A 30-Year Legacy of Volcanism. EOS, Transactions, American Geophysical Union, 191(19): 169-170.

Vallance, J.W., Schneider, D.J. and Schilling, S.P., 2008. Growth of the 2004-2006 lava-dome complex at Mount St. Helens. In: D.R. Sherrod, W.E. Scott and P.H. Stauffer (Editors), A Volcano Rekindled: The Renewed Eruption of Mount St. Helens, 2004-2006. Professionnal Paper 1750. U.S. Geological Survey, pp. 169-208.

Varley, N., Arámbula-Mendoza, R., Reyes-Dávila, G., Sanderson, R. and Stevenson, J., 2010. Generation of Vulcanian activity and long-period seismicity at Volcán de Colima, Mexico. Journal of Volcanology and Geothermal Research, 198(1-2): 45-56.

Vidal, N. and Merle, O., 2000. Reactivation of basement faults beneath volcanoes: a new model of flank collapse. Journal of Volcanology and Geothermal Research, 99(1–4): 9-26.

Voight, B., 1988. A Method for prediction of volcanic eruptions. Nature, 332: 125-130.

Voight, B. and Elsworth, D., 2000. Instability and collapse of hazardous gas-pressurized lava domes. Geophysical Research Letters, 27(1): 1-4.

Voight, B., Sparks, R.S., Miller, A.D., Stewart, R.C., Hoblitt, R.P., Clarke, A., Ewart, J., Aspinall, W.P., Baptie, B., Calder, E.S., Cole, P., Druitt, T.H., Hartford, C., Herd, R.A., Jackson, P., Lejeune, A.M., Lockhart, A.B., Loughlin, S.C., Luckett, R., Lynch, L., Norton, G.E., Robertson, R., Watson, I.M., Watts, R. and Young, S.R., 1999. Magma Flow Instability and Cyclic Activity at Soufriere Hills Volcano, Montserrat, British West Indies. Science, 283(5405): 1138-1142.

Wack, M.R. and Gilder, S.A., 2012. The SushiBar: An automated system for paleomagnetic investigations. Geochemistry, Geophysics, Geosystems, 13(3): n/a-n/a.

Waite, G.P., Chouet, B.A. and Dawson, P.B., 2008. Eruption dynamics at Mount St. Helens imaged from broadband seismic waveforms: Interaction of the shallow magmatic and hydrothermal systems. J. Geophys. Res.-Solid Earth, 113(B2): B02305.

Watts, R.B., Herd, R.A., Sparks, R.S. and Young, S.R., 2002. Growth patterns and emplacement of the andesitic lava dome at Soufriere Hills volcano. In: T.H. Druitt and B.P. Kokelaar (Editors), The eruption of Soufriere Hills volcano, Montserrat, from 1995 to 1999. Geological Society of London Memoirs, pp. 115-152.

Webb, S.L. and Dingwell, D.B., 1990. Non-Newtonian rheology of igneous melts at high stresses and strain rates: experimental results for rhyolite, andesite, basalt and nephelinite. Journal of Geophysical Research, 95: 15695-15701.

Wells, D.L. and Coppersmith, K.J., 1994. New empirical relationships among magnitude, rupture length, rupture width, rupture area, and surface displacement. Buletin of the Seismological Society of America, 84(4): 974-1002.

Wenk, H.R., 1978. Are pseudotachylites products of fracture or fusion? Geology, 6(8): 507-511.

Wohlfarth, E.P., 1958. Relations between different modes of acquisition of the remanent magnetization of ferromagnetic particles. Journal of Applied Physics, 29: 595-596.

Yamamoto, H., Takayama, K. and Kedrinskii, V., 2008. An analog experiment of magma fragmentation: behavior of rapidly decompressed starch sirup. Shock Waves, 17(6): 371-385.

Yong, C. and Wang, C.Y., 1980. Thermally induced acoustic emission in rocks - influences of water and temperature disturbances. Geophysical Research Letters, 7: 1089-1092.

Zellmer, G.F., Hawkesworth, C.J., Sparks, R.S.J., Thomas, L.E., Harford, C.L., Brewer, T.S. and Loughlin, S.C., 2003. Geochemical Evolution of the Soufrière Hills Volcano, Montserrat, Lesser Antilles Volcanic Arc. Journal of Petrology, 44(8): 1349-1374.

Zobin, V.M., Amezcua, M.G., Davila, G.A.R., Dominguez, T., Chacon, J.C.C. and Alvarez, J.M.C., 2002. Comparative characteristics of the 1997-1998 seismic swarms preceding the November 1998 eruption of Volcan de Colima, Mexico. Journal of Volcanology and Geothermal Research, 117(1-2): 47-60.

Zobin, V.M., Varley, N.R., González, M., Orozco, J., Reyes, G.A., Navarro, C. and Bretón, M., 2008. Monitoring the 2004 andesitic block-lava extrusion at Volcán de Colima, México

from seismic activity and SO2 emission. Journal of Volcanology and Geothermal Research, 177(2): 367-377.

"The world is my playground too, and I'll do what I like"

- Archive

CURRICULUM VITAE

<u>Personal Information</u>

Jackie Evan Kendrick; Born 15 December 1986 in Cardiff, United Kingdom.

<u>Qualifications</u>

2010 – 2013	**PhD Experimental volcanology, Ludwig-Maximilians-University, Munich**
2005 – 2009	**MSci Geology, University College London**
2003 – 2005	**A-Levels, Hereford Sixth Form College**
1998 – 2003	**GCSE's, Fairfield High School**

<u>Work Experience</u>

2010 – 2013 **Ludwig-Maximilians-University, Munich, Germany**
- Study of frictional properties of magmas using a high-velocity rotary shear apparatus.
- Rheological studies using a high temperature, 300 KN, constant-load or constant strain-rate uniaxial press.
- Electron back-scatter diffraction (EBSD) on volcanic rocks.
- Viscosity measurements by Micropenetration.
- Differential scanning calorimetry.
- Permeability studies using the "fragmentation bomb".
- Chemical analyses including WDA, XRF and XRD.
- Structural mapping and sample collection at: Volcán de Colima, Ceborucco and La Primavera, Mexico; Soufrière Hills volcano, Montserrat; Tarawera and Ngongataha volcanoes, New Zealand; Mount St. Helens and Newberry Caldera, USA.

2011 **Teaching Assistant (DAAD), Ludwig-Maximilians-University, Munich, Germany**
- For the class Petrophysics at Masters level.

2009 **Volunteer, USGS Cascade Volcano Observatory, Washington, USA**
- Fieldwork at Mount St. Helens with the PIRE (Partnership in Volcanological Research and Education) group.
- Assistance with the deployment of "spiders" (portable telemetered stations) at Mount St. Helens for the OASIS (Optimised Autonomous Space In-situ Sensorweb) project for hazard monitoring.
- Plotting and analysis of RSAM, helicorder and spectogram data for the 2007/2008 eruptions of Soputan volcano, Indonesia.
- Setting up GPS and seismic base stations at Crater Lake volcano, Oregon.
- Investigations into mass movement dynamics at the experimental debris-flow flume at H.J. Andrews Experimental Forest, Oregon.

2005 – 2009 **University College London, London, United Kingdom**
- Strength tests using a room-temperature, uniaxial press at UCL with Rosanna Smith and Peter Sammonds.
- Structural mapping and sample collection in the crater of Mount St Helens.
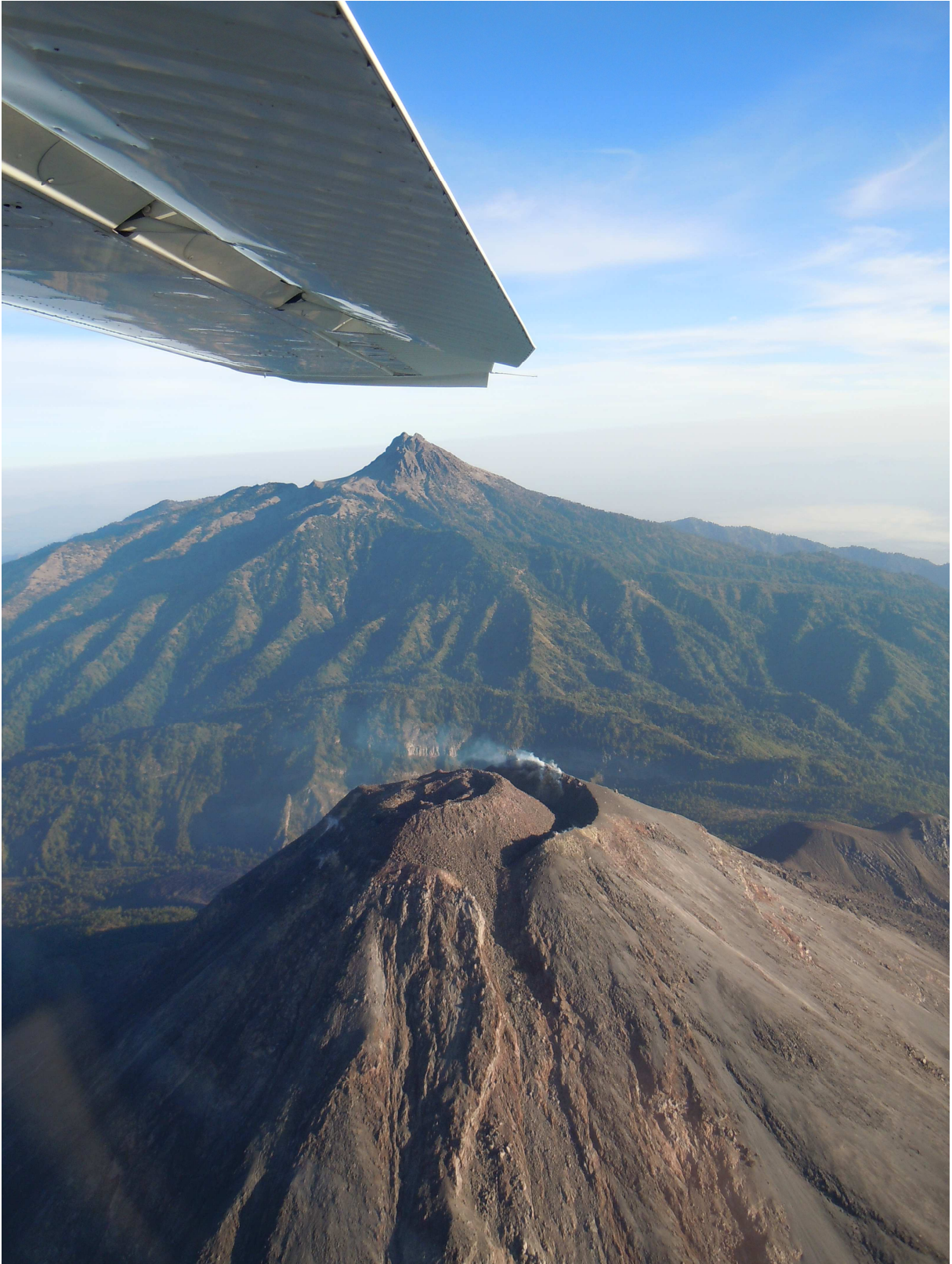
"From the end spring new beginnings."

-Pliny the Elder